COMPLEX RARE-EARTH ANTIMONIDE SUBOXIDES

COMPLEX RARE-EARTH ANTIMONIDE SUBOXIDES FOR THERMOELECTRIC APPLICATIONS

By

PENG LI WANG, B.Sc. [Hons.]

A Thesis Submitted to the School of Graduate Studies in Partial Fulfillment of the Requirements for the Degree

Doctor of Philosophy

McMaster University

Doctor of Philosophy (2013) McMaster University

(Chemistry) Hamilton Ontario

TITLE: Complex Rare-earth Antimonide Suboxides for Thermoelectric Applications

AUTHOR: Peng Li Wang

SUPERVISOR: Dr. Yurij Mozharivskyj

NUMBER OF PAGES: xxii, 182

Abstract

In the search for potential high-performance thermoelectric materials, a number of rare-earth (*RE*) antimonide suboxide phases have been investigated. These compounds were prepared from traditional solid state synthetic routes or high-temperature sintering methods. X-ray single crystal and powder diffraction techniques were employed for structural determinations and bulk sample phase analyses. Energy-dispersive X-ray spectroscopy (EDS) and electron micro-probe analysis (EMPA) were used to confirm the chemical compositions of the single crystals and bulk samples. Selected bulk samples (purity > 90 at. %) were subjected to physical property measurements in order to study their electrical and thermal transport properties. The relationships between the crystal structures and electrical properties were analyzed using electronic structure calculations.

Based on their structures, the rare-earth antimonide suboxides under investigation can be classified as: the $RE_3Sb_3O_3$ and $RE_8Sb_{3-\delta}O_8$ phases (*C*2/*m* space group) based on the *RE*–O frameworks, the *RE*–Sb–O–C natural superlattices (*P*4/*n, P*4/*nmm* and *P*4*bm* space groups), and the *anti*-$ThCr_2Si_2$ type RE_2SbO_2 compounds (*I*4/*mmm* space group). Regardless of their diverse structures, the rare-earth (*RE*) antimonide suboxides share some interesting common features including the basic RE_4O tetrahedral building blocks and the anionic antimony sites.

In terms of chemistry, the RE_2SbO_2 compounds appeared to be the most thermally stable and robust toward elemental substitutions. As a result, a series of RE_2SbO_2 phases with different rare-earth elements were produced in bulk quantities for systematic

thermoelectric property measurements. The elemental substitution on the Sb site was also achieved based on the Ho_2SbO_2 phase. As an extension of the RE_2SbO_2 series, the iso-structural $Ho_2Sb_{1-x}Bi_xO_2$ phases were synthesized to further explore the structure-property relationships in this system. The less thermally robust RE_3SbO_3 and $RE_8Sb_{3-\delta}O_8$ phases were selectively produced by kinetic and thermodynamic controls, respectively. Due to synthetic challenges, the physical property studies were conducted for a few rare-earth analogs (Sm and Ho). The most chemically complex rare-earth antimonide suboxides belong to the *RE*–Sb–O–C natural superlattice family, where the layered structures are stabilized by carbon impurities. The detailed preparative studies revealed a number of related superlattice structures formed as a result of different impurity levels in the starting materials.

The physical property measurements on the high-purity bulk samples revealed unexpected semiconducting properties in the non-charge-balanced systems, i.e. $RE_8Sb_{3-\delta}O_8$ and RE_2SbO_2. Since the electronic structure calculations suggested that the anionic Sb state dominates the band at the vicinity of the Fermi level, the local structures of the Sb atomic site were believed to be the source of the observed physical properties. Such behaviors were explained under the framework of Anderson/Mott-type localizations. Ultimately, systematic investigation through the RE_2SbO_2 and $Ho_2Sb_{1-x}Bi_xO_2$ series elucidated the large variability of electrical properties in these systems caused by local structural perturbations.

Preface

The opening chapter of this dissertation starts with an introduction to the thermoelectric phenomenon, applications and thermoelectric materials. Subsequently, the challenges and progresses in the field of thermoelectric material research are highlighted. By analyzing some of the most successful materials, the philosophies behind the individual projects were elucidated. In Chapter 2, the experimental methods and techniques used in the research are described in details to better illustrate the nature of the author's work.

In Chapter 3, investigations evolved around the novel rare-earth antimonide suboxides, RE_3SbO_3 and $RE_8Sb_{3-\delta}O_8$, were discussed. These phases were originally discovered during the exploration of the *RE*-Sb-O-C natural superlattices. Although the studies on the *RE*-Sb-O-C natural superlattices started chronologically earlier, the work on the RE_3SbO_3 and $RE_8Sb_{3-\delta}O_8$ compounds is presented as the foremost project in this dissertation. Compared to the structural studies on the *RE*-Sb-O-C natural superlattice (depicted in Chapter 4), Chapter 3 gives more comprehensive illustrations of the research work conducted in our group.

From the chemical perspective, RE_3SbO_3 and $RE_8Sb_{3-\delta}O_8$ can be considered as the result of the direct combination of rare-earth oxides and rare-earth mono-antimonides, thus, they were the better representatives of the rare-earth antimonide suboxide family than the impurity-stabilized *RE*-Sb-O-C natural superlattices. Furthermore, the anionic pnictogen (Sb^{3-}), a key feature shared by all the phases discussed within the scope of this

document, was more clearly emphasized in the RE_3SbO_3 and $RE_8Sb_{3-\delta}O_8$ systems. Some of these compounds were obtained in bulk quantities and high purities, so that we were able to conduct more in-depth physical property measurements. Ultimately, the structure-property relationships demonstrated in the RE_3SbO_3 and $RE_8Sb_{3-\delta}O_8$ systems formed the foundation for understanding the transport phenomena in the RE_2SbO_2 systems.

Although the RE_3SbO_3 and $RE_8Sb_{3-\delta}O_8$ compounds described in Chapter 3 were produced by fusing the rare-earth antimonides with the corresponding rare-earth oxides, their crystal structures were not intended to preserve the structural features of either chemical component. Unlike RE_3SbO_3 and $RE_8Sb_{3-\delta}O_8$, the *RE*-Sb-O-C natural superlattices described in Chapter 4 were structurally designed to retain the building blocks of the rare-earth antimonides and rare-earth oxides, so that the favorable physical properties of the two constituents can be combined to yield high thermoelectric performances. The structural engineering behind these superlattice structures are discussed in detail in this chapter, as well as the careful chemical studies conducted to explore their true compositions. Although the chemical compositions of the *RE*-Sb-O-C natural superlattices were proven to deviate from the pure suboxide, the later works on the RE_2SbO_2 phases (Chapter 5) built upon the natural superlattice approach illustrated in Chapter 4.

Unlike the explorative studies discussed in the previous chapters, the investigation described in Chapter 5 was based on the classic *anti*-$ThCr_2Si_2$ type RE_2SbO_2 compounds. Although the RE_2SbO_2 system had been studied by other groups, from our perspective, the average RE_2SbO_2 structure can be understood as a natural superlattice of stacked

RE_2O_2 slabs and Sb layers. Less obviously, the RE_2SbO_2 and $RE_8Sb_3O_8$ systems shared similar local atomic displacements on Sb sites, which ultimately resulted in their unexpected semiconducting properties.

The research on the RE_2SbO_2 phases was elucidated in Chapter 5 of the dissertation because the previous chapters may assist a reader to gain better insights into the RE_2SbO_2 systems. The experience accumulated from the *RE*-Sb-O-C phases had lead us to the layered RE_2SbO_2 structure, in which atomic arrangements in one sublattice can be controlled by chemical perturbations applied to the neighboring sublattices. The studies on the RE_3SbO_3 and $RE_8Sb_{3-\delta}O_8$ phases have established the interrelations between physical properties and disordered atomic sites. Without a clear comparison between the classic semiconducting RE_3SbO_3 and the disorder-based semiconductor, $RE_8Sb_{3-\delta}O_8$, the relevance of Anderson/Mott localization in the RE_2SbO_2 systems may not have been noticed.

The orthorhombic Ho_2SbO_2 phase (*Fmmm* space group) in Chapter 6 was discovered in an attempt to produce the bulk RE_2SbO_2 compounds through classic solid state sintering methods at a relatively low temperature. At 1273 K, only the holmium compound was obtained while the other rare-earth elements did not yield the desired phases. The investigations focused on the structurally modified Ho_2SbO_2 compound can be considered as an extension to the work on the tetragonal RE_2SbO_2 phases, as it further illustrated the impact of minor structural alterations on the physical properties of the RE_2SbO_2 compounds. The research efforts discussed in Chapter 6 have not been

published yet, since more detailed structural studies have to be conducted to confirm some of the hypotheses.

Similar to Chapter 6, the project discussed in Chapter 7 is tightly related to the RE_2SbO_2 system described in Chapter 5. The electrical properties of the RE_2SbO_2 compounds were found (in Chapter 5) to be variable within a large range depending on the atomic displacements of the Sb atoms, which were in turn controlled by the size of the unit cell. However, the decreasing unit cell dimensions were limited by the sizes of the rare-earth atoms. After erbium, the choice for the rare-earth elements became exhausted with the increasing rarity of Tm, Yb and Lu. Intuitively, an alternative approach was to fit the large Bi atoms into the Sb atomic sites.

In Chapter 7, the studies on the $Ho_2Sb_{1-x}Bi_xO_2$ compounds aim to further explore the effect of reduced lattice disorder, rather than simply closing the compositional gap between the Sb and Bi containing phases. The use of bismuth can be viewed as an extension to the local structural modification instead of chemical perturbations. Therefore, the topic of this dissertation remains focused on the rare-earth antimonide suboxides. From the pure structural perspective, the physical properties observed in the $Ho_2Sb_{1-x}Bi_xO_2$ compounds could be realized without Bi, given that the size of the rare-earth elements can be further reduced.

Finally, in the last part of this document, a number of conclusions are drawn for the rare-earth antimonide suboxides as an interrelated chemical system in term of their compositions, structures and physical properties. In addition, guidelines for further investigations are also highlighted.

Acknowledgement

I would like to express my gratitude towards a great number of people who were vital in the completion of this work. First and foremost, I would like to thank my supervisor, Dr. Yurij Mozharivskyj for giving me the opportunity to work in his group and for all the guidance he has given me through the years. I am also grateful for the guidance and wisdom I have received from my supervisory committee members, Dr. John Greedan and Dr. Jacques Barbier.

I thank the past and current members of the Mozharivskyj's group, especially Mr. Scott Forbes and Dr. Jinlei Yao, for their support and assistance in both research works and in daily life. To our collaborators, especially Dr. Taras Kolodiazhnyi, thank you all for your patience and insights, that made the completion of this work possible. I greatly appreciate the supportive and cheerful environment created by Dr. Hanna Dabkowska, Dr. Antoni Dabkoski and the members of Greedan group. And I am very grateful for the staff and faculty members in the department, particularly Dr. William Leigh, for providing me a wonderful experience as a graduate student.

Without a supportive and understanding family, I could not have succeeded in my studies. My fiancé, Svetlana Kostina, has always been a wonderful life companion through my time at McMaster. To my parents, who selflessly supported me all my life, I owe the deepest gratitude. I also truly appreciate everyone in mine and Lana's family for they make my life joyful and exciting.

Table of Contents

List of Figures

List of Tables

Chapter 1. Introduction

Thermoelectric materials are able to convert heat directly into electricity and vice versa. This special property makes thermoelectric materials valuable for a variety of applications involving power generation and refrigeration. [1-4]

1.1 History and Background Theory

The first thermoelectric phenomenon was discovered in 1822 by German scientist, Thomas Johans Seebeck (1770–1831).[2] He observed that applying heat at the joint of two dissimilar metals in a closed circuit caused a nearby compass needle to turn (Figure 1.1). Seebeck characterized this observation as a magnetic phenomenon and attempted to explain the existence of earth's magnetic field as a result of the temperature difference between the poles and the equator. [5] During the same period of time, many scientists including Ampère, Biot, Savart and Laplace, were investigating the interactions between electrical currents and magnetic fields. Among them, Hans Christian Oersted (1777–1851), first deduced the electrical nature of the phenomenon and introduced the concept of "thermoelectric effect" rather than "thermomagnetism". [6] Despite the fact that Seebeck had denied the electrical nature of his experiment, the importance of his work lies with the extensive thermoelectric data he had collected, some of which are still of interest today.[6, 7]

The modern notation of the Seebeck coefficient (thermopower), α, is used to define the ratio between the change of chemical potential (voltage) and the temperature difference[8].

$$\alpha = \left(\frac{\Delta V}{\Delta T}\right) [\mu V/K] \quad (1\text{-}1)$$

When a temperature gradient, ΔT, is applied to a thermoelectric material, the charge carriers in the hot end, with a higher kinetic energy, diffuse through the material more easily than those from the cold end. As an equilibrium is reached, the accumulation of charge carriers at the cold side occurs which gives rise to a voltage difference, ΔV.[9]

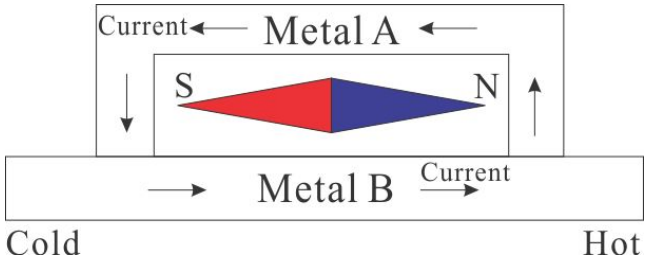

Figure 1.1. Schematics of the experimental setup used in the observation of the Seebeck effect.

Since the Seebeck coefficient relates the temperature to the electrical potential (Equation 1-1), thermocouples were developed by calibrating the Seebeck coefficient of a given bi-metallic couple.[6] Shown in Figure 1.2, a thermocouple can be considered as a circuit formed from two dissimilar conductors (*A* and *B*). If the junctions are maintained at different temperatures, *T1* and *T2*, an open circuit electromotive force (e. m. f.), *V* is developed. The potential, *V*, can be measured by a potentiometer and then the temperature difference between *T1* and *T2* can be calculated.

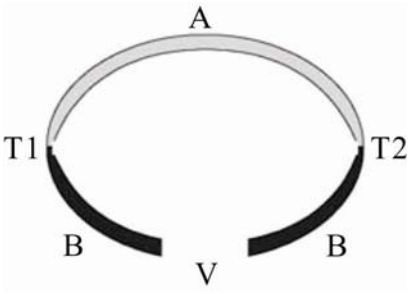

Figure 1.2. Schematics of a simple thermocouple.[7]

While thermocouples were the major application of thermoelectricity until the 1930s,[6] the foundations of other applications such as cooling and power generations was established twelve years after Seebeck's original experiment. French physicist Jean Peltier (1785–1845) observed the temperature difference at the junction of two dissimilar conductors, as an electric current was passed through.[10] While Peltier's observation was not recognized as the counter phenomenon of the Seebeck effect, in 1838, Emil Lenz (1804–1865) was able to demonstrate that either heating or cooling occurs at the metal junction depending on the direction of current flow. The Peltier coefficient Π, defines the ratio between the rate of the heat flow Q and the applied current I.[11]

$$\Pi = \frac{Q}{I} \text{ [W/A]} \tag{1-2}$$

The interdependency between the Seebeck effect and the Peltier effect was identified by William Thomson (later Lord Kelvin, 1824–1907). In 1851, he postulated the third thermoelectric effect, known as the Thomson effect, corresponding to the reversible change of heat content in any non-isothermal segment of a single homogeneous conductor material, when a current is passed through under a temperature gradient.[12] The

Thomson coefficient, μ, denotes the rate of heat production per unit volume of a certain material, and thus the Seebeck effect (α) and the Peltier effect (Π) can be interrelated:

$$\frac{d\Pi}{dT} - \alpha - \mu = 0 \tag{1-3}$$

$$\frac{d\Pi}{dT} - \frac{\Pi}{T} - \mu = 0 \tag{1-4}$$

And the equations above imply the Thomson relations: [12, 13]

$$\mu = T\frac{d\alpha}{dT} \tag{1- 4a}$$

$$\Pi = \alpha T \tag{1-4b}$$

Although the basic theories of thermoelectricity were well established by 1850s, there was no guideline for thermoelectric material research until Edmund Altenkirch derived the maximum efficiency of a power generator (1909)[14] or a cooler (1911)[15] based on thermoelectric effect. Ioffe[6] later developed the 'figure of merit', *ZT*, to denote the thermoelectric efficiency, which is defined by three important parameters: the Seebeck coefficient α, the electrical conductivity, σ, and the thermal conductivity, κ.

$$ZT = \frac{\alpha^2\sigma}{\kappa}T \tag{1-5}$$

1.2 Thermoelectric Applications

Following the development of the modern theory of thermoelectricity, during the 1950s, the major focus of thermoelectric research moved from metals to semiconductor compounds for their higher thermoelectric power.[16] Owning to the developments in the

semiconductor transistors and driven by the interests in military applications, new semiconducting materials with substantially improved thermoelectric properties were investigated.[10] However, by 1970 the research efforts had declined due to the limited improvements in the maximum ZT value. Despite the low efficiencies, thermoelectric devices offer exceptional reliability. Therefore many of them were designed for missions in outer space or in remote parts of the planet, where the device's efficiency is outweighed by the demand for reliability. The radioisotope thermoelectric generators (RTG), originally developed in the late 1950s, have been implemented in a number of spacecrafts. Figure 1.3 illustrates the design of the radioisotope thermoelectric generator used in the Cassini probe. The radioactive decay of ^{238}Pu provides a steady temperature of 1000°C acting as the hot end of the thermoelectric device, and with the outer space acting as the heat sink, the module generated 300 Watts of electrical power at the start of mission and has kept functioning maintenance free since 1997.[17]

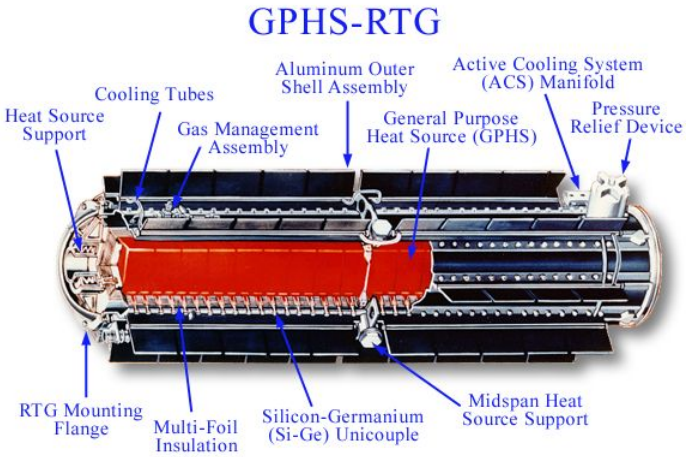

Figure 1.3. The General-Purpose Heat Source (GPHS) Radioisotope Thermoelectric Generator (RTG) on the Cassini spacecraft.[17]

The increase in crude oil prices in the mid 70s[10] and the public concern for environmental problems caused by compressor liquids (CFCs)[2] generated renewed interests in thermoelectric power generation and cooling applications. During the last two decades, along with the progresses in the fields of semiconductor technologies, material science, solid-state chemistry and device engineering, many thermoelectric devices have become commercially available. Some of them such as the automobile/camper fridges compete against the traditional compressor fridges with their high mobility and low cost. Others like air-conditioners and water chillers are sold for their simplicity in terms of installation and maintenance, quietness during operation (no moving parts) and versatility (heating or cooling depends on the current direction).[18]

Today, a large part of the world's overall energy resources is consumed as thermal energy. However the efficiencies for thermal energy utilization are around 30 to 35% with the major portions rejected as waste heat. With the growing global demand for energy management and conservation, high-temperature thermoelectric generation has attracted a lot of basic research efforts.[10] Thermoelectric modules have been developed to harvest wasted energy from heat sources such as manufacturing plants and automobiles. Figure 1.4 shows the general energy distribution of a gasoline-fueled internal-combustion engine vehicle, where only 25% of the fuel energy is used for transportation along with a whopping 40% waste. Thermoelectric materials can be utilized to convert a portion of the wasted heat into electrical power to support the ever growing electronic contents in the same vehicle.[19, 20]

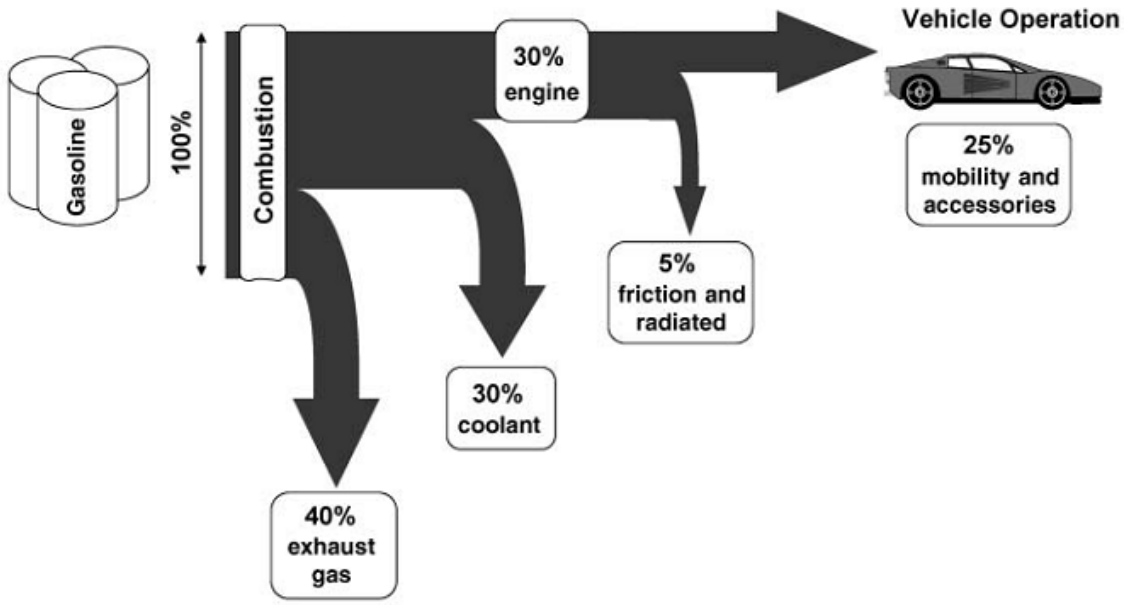

Figure 1.4. Energy distribution in a gasoline-fueled internal-combustion engine vehicle.[20]

Another emerging field of thermoelectric application is the small-scale, localized cooling on electronic devices including low noise IR detectors, optoelectronics and computer CPUs, where the traditional compressor-based cooling devices can no longer compete with the thermoelectric devices as their efficiencies decrease dramatically as they are scaled down in size. As shown in Figure 1.5, the current thermoelectric modules deliver reasonable efficiency at the milli-watt and even micro-watt power level.[21] The significance of the localized thermoelectric cooling rests with the potential performance gain in the electronics, especially in the computer processors. If the so-called "cold computing" can be achieved, some computer processors based on the complementary metal oxide semiconductor (CMOS) technology can perform 30-200% faster.[3]

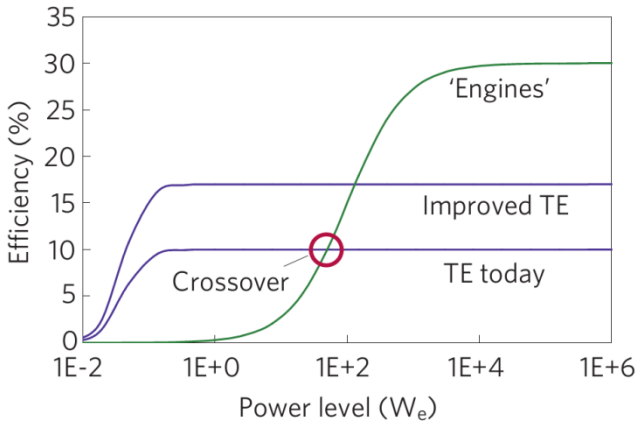

Figure 1.5. Efficiency of thermoelectric devices compared to that of the traditional technologies at different power levels. [21]

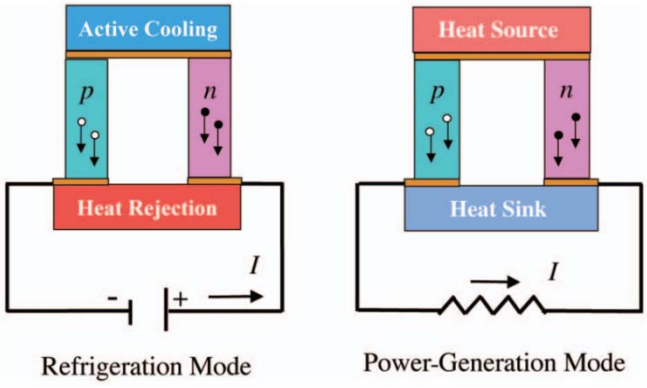

Figure 1.6. Schematics of a thermoelectric couple from an *n*-type and a *p*-type semiconductor. Depends on a current or a temperature gradient is applied, the device can perform Peltier cooling or Seebeck powder generation, respectively. [2, 3]

Despite the large variety of their applications, most thermoelectric devices require both *n*-type and *p*-type thermoelectric materials, which are joined at one end and connected to an electrical circuit through the other ends. Shown in Figure 1.6 (left), when a current (*I*) is passed though the closed circuit, the electrons in the *n*-type material flow from the junction toward the base, while the holes in the *p*-type material also flow from the junction to the base, as the carriers also transport heat, a temperature gradient is

produced by the Peltier effect. Conversely, if a temperature gradient is applied between the junction and the base, a Seebeck voltage is developed at the two base electrodes (Figure 1.6 right).[2, 3]

1.3 Thermoelectric Efficiency

Although much engineering and designing efforts have been incorporated into thermoelectric devices, the thermoelectric material at the heart of each module governs its efficiency. Equation (1-5) provides important clues in searching for high performance thermoelectric materials. Materials with a high figure-of-merit, *ZT*, have to possess large Seebeck coefficients, good electric conductivities and minimal thermal conductivities. [1-4, 22]

$$\eta = \frac{T_H - T_C}{T_H} \times \frac{\sqrt{1+ZT}-1}{\sqrt{1+ZT}+\frac{T_C}{T_H}} \quad (1\text{-}6)$$

When the figure-of-merit, *ZT*, is expressed in Carnot efficiency,[3] as in equation 1-6, the overall efficiency of a given thermoelectric material also depends on the temperature gradient (difference between T_H and T_C). As a result, under the normal operating conditions (T < 1000°C) thermoelectric devices do not offer much advantage over the competing technologies unless the figure-of-merit, *ZT*, can be dramatically improved (Figure 1.7). To guide our search of the high *ZT* materials, the interrelations between the Seebeck coefficient, the electrical conductivity and the thermal conductivity has to be analyzed in detail.

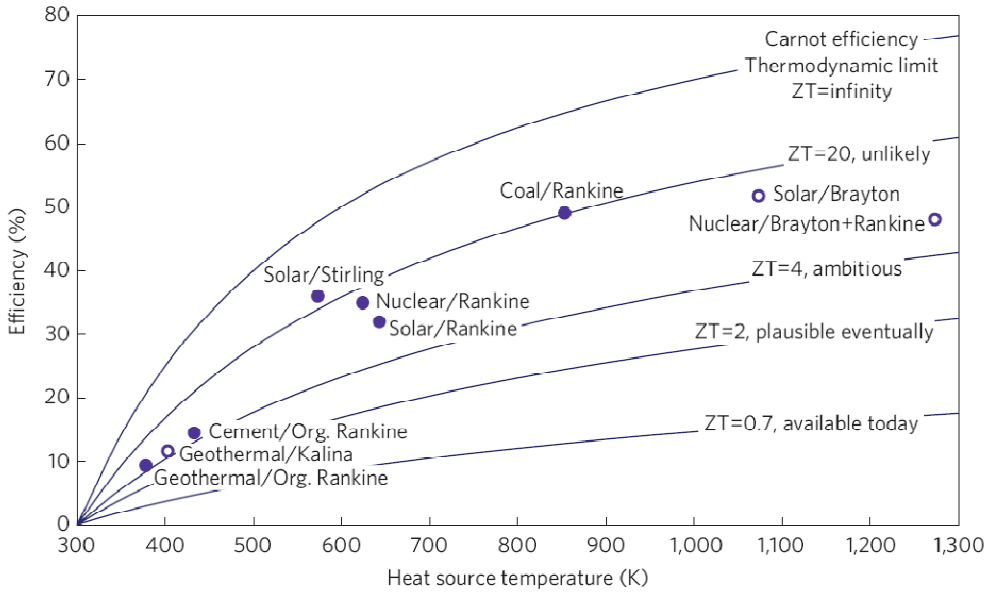

Figure 1.7. Efficiency of the mechanical heat engines (technology/company) compared with a thermoelectric estimate.[21]

1.3.1 Thermoelectric Power Factor

The term "power factor" is defined as $\alpha^2\sigma$. As shown in Equation 1-5, the efficiency of a given thermoelectric material is proportional to the value of the power factor. The importance of the Seebeck coefficient is obvious, as it defines the potential difference developed under a given temperature gradient, whereas a high electrical conductivity allows the charge carriers to transport thermal energy in the material without creating extra heat. Joule heating is an irreversible process of heat generation due to the internal electrical resistance, and the amount of heat evolved is directly proportional to the resistivity of the material, therefore inversely related to its electrical conductivity. The temperature gradient generated from (or applied to) a less electrically conductive material is compromised by the Joule heating since the heat evolves uniformly through the material regardless of the direction of current.[23]

Optimization of the power factor represents one of the major challenges in the field of thermoelectric research, since the two electrical parameters, α and σ, form a compromising relationship. In a conductive material, the electrical conductivity depends on the charge carrier concentration, n, the charge of the carrier, e, and the carrier mobility, μ.

$$\sigma = ne\mu \text{ [S·m]} \tag{1-7}$$

The electrical conductivity of a metal is high since there is a large concentration of free conduction electrons present independently of the temperature. These conduction electrons occupy a large number of electronic states up to a very high energy level even without thermal excitation. Consequently, a typical metal remains electrically conductive at 0 K since its conduction electrons still reside in the high energy states. However, under an applied temperature gradient, only a small fraction of the conduction electrons in the highest energy states (at the Fermi Level) can be thermally excited, while the rest of them are not able to move up in energy as the neighboring electronic states are completely filled.[6, 23] Since the electronic states of metals are so closely distributed in energy, the gain in electric potential per temperature difference, $\Delta V/\Delta T$ (Seebeck coefficient) is small.

In a semiconductor, the charge carriers (electrons or holes) have to be thermally excited across a forbidden energy range (band gap) in order to move freely. Thus, the total number of free charge carriers, n, in a semiconductor depends on temperature and the size of the band gap, ΔE, as in the Boltzmann relationship:

$$n \propto exp\left(-\frac{\Delta E}{kT}\right) \tag{1-8}$$

While the electrical conductivity of a semiconductor is much lower than that of a metal due to the limited number of conducting charge carriers, for each charge carrier excited across the band gap, the potential energy change caused by the thermal excitation is more significant (Seebeck voltage). Goldsmid and Sharp have shown that the maximum Seebeck coefficient of a semiconductor is directly proportional to the energy gap, ΔE.[24] As a result, the thermopower of a semiconductor can reach >200 μV/K, whereas that of a metal is usually in the range of ~10 μV/K.[23] Mathematically, the Seebeck coefficient is correlated to the charge carrier concentration, n, by equation 1-9[25] (where k_B is Boltzmann constant and m^* is the effective mass of the charge carrier).

$$\alpha = \left(\frac{8\pi^2 {k_B}^2}{3eh^2}\right) m^* T \left(\frac{\pi}{3n}\right)^{2/3} \tag{1-9}$$

Equation 1-7 and 1-9 represent the first paradox of thermoelectric research: as the band gap increases, the Seebeck coefficient of a material increases at the expense of its electrical conductivity due to the diminishing number of free charge carriers at a given temperature.

In addition to the trade-off between α and σ with respect to the charge carrier concentration, the charge carrier mobility, μ, and the effective mass, m^*, are also inversely related. While large effective masses produce high thermopowers (equation 1-9), the heavy carriers are slower, therefore exhibit small mobilities, which result in low electrical conductivities (equation 1-7). The exact relationship between effective mass and mobility is not well understood and the optimum effective mass is not obvious.

However, good thermoelectric materials have been found to exhibit a wide range of effective masses and mobilities.[25]

1.3.2 Electrical and Thermal Conductivity

Another road block preventing the optimization of the thermoelectric effect arises from the relationship between electrical and thermal conductivities. The significance of a low thermal conductivity in a thermoelectric material lies with its ability to maintain the applied (or created) temperature gradient by preventing heat transfer from the hot to the cold junction. Therefore, the value of thermal conductivity, κ, is inversely related to the thermoelectric efficiency ZT (equation 1-5).[6]

The thermal conductivity of a solid (κ) consists of two parts: the electronic thermal conductivity (κ_{el}) and the lattice thermal conductivity (κ_l). Improving the electrical conductivity, σ, of a given material usually increases the electronic contribution to its thermal conductivity according to the Wiedeman-Franz law (L is Lorenz number and T is temperature):[4, 26]

$$\kappa_{el} = L\sigma T \tag{1-10}$$

Fortunately, the lattice thermal conductivity, κ_l, is not electronically related and it depends on the specific heat capacity C_v, mean free path of the phonon, l, and the velocity of sound in the material, v_s:[27]

$$\kappa_l = {}^1\!/_3\, C_v l v_s \tag{1-11}$$

At high temperatures, the specific heat, C_v, approaches a constant value while the mean free path, l, of the phonon decreases due to the increasing phonon-phonon scattering.[27, 28]

For a given material, there is a maximum lattice thermal conductivity, which can be reduced by enhancing the phonon scattering mechanism. Therefore, to a certain extent, it is possible to offset the negative effect of the high electrical conductivity on the electrical thermal conductivity by limiting the lattice contribution. [4, 22]

1.4 Thermoelectric Materials

As discussed in Section 1.3, the challenges in the search of high performance thermoelectric materials arise from the intricate interrelations between the physical parameters α, σ and κ, which constitute the thermoelectric efficiency, ZT. By understanding the physics behind these quantities, some guidelines for material selection and strategies for property optimization can be summarized.

1.4.1 General Criteria

It was shown previously that metals, despite their high electric conductivity, are not desirable for thermoelectric applications due to their low thermopower. Insulators, on the contrary, usually exhibit good thermopowers but poor electrical conductivities. In order to satisfy the compromise between the Seebeck coefficient and the electrical conductivity, there is a range of charge carrier concentration that allows the optimization of thermoelectric power factor, $\alpha^2\sigma$. As shown in Figure 1.8, the value of power factor peaks at a charge carrier concentration around 10^{19} carriers per cm^3. [3, 6, 7, 25]

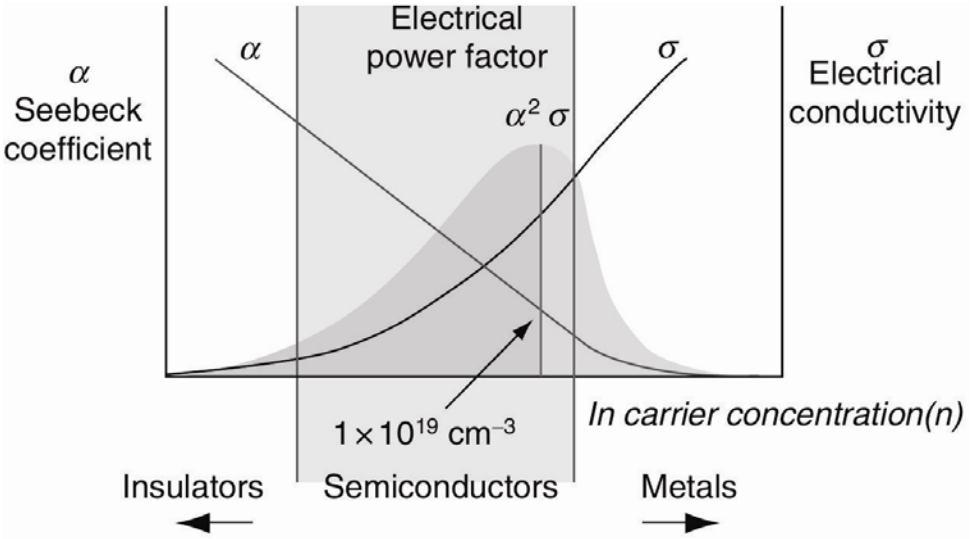

Figure 1.8. Dependence of the electrical conductivity, σ, the Seebeck coefficient, α, and the power factor, $\alpha^2\sigma$, on charge carrier concentration.[7]

While the favored charge carrier concentration leads our search for high *ZT* materials towards the heavily doped semiconductors and semimetals, Mahan *et al.*[29] suggested an energy gap about $10k_BT$ (0.26 *eV* at room temperature) would be ideal for a thermoelectric material. Any smaller band gap allows excitation of compensating charge carriers, which lowers the Seebeck coefficient, whereas the larger band gaps limits the number of free charge carriers at a given temperature.

In addition to the electrical properties outlined above, the lattice thermal conductivity should approach the minimum possible value in good thermoelectric materials. A semiconductor composed of heavy elements tends to possess a lower thermal conductivity, according to equation 1-12, the lattice contribution to a solid's thermal conductivity is inversely related to the average atomic weight of the constituents, *A*.[28]

$$\kappa_l = \frac{R^{3/2}}{3\gamma^2\varepsilon^3 N^{1/3}} \frac{{T_m}^{3/2}\rho^{2/3}}{A^{7/6}} \quad (1\text{-}12)$$

In the above equation, R is the ideal gas constant, γ is the Gruneisen constant, N is Avogadro's number, T_m is the melting point, ε is the amplitude of inter-atomic vibration, and ρ is the density. Empirically, other features in a solid state compound such as a large unit cell or a complex crystal structure may also facilitate lower thermal conductivities since the heat carrying phonons have to propagate through a more difficult pathway.[2]

In summary, good thermoelectric materials are likely found among heavily doped semiconductors or semimetals which consist of heavy elements and adopt complex crystal structures. In addition to the basic criteria, there are more specific strategies aiming to improve one or more physical properties contributing to the thermoelectric performance through electronic band structure engineering and crystal structure design. These optimizing strategies have lead to significantly improved *ZT* in certain classes of materials. Currently, the state-of-the-art thermoelectric materials possess maximum *ZT* values exceeding 1.5 (Figure 1.9). In the following sections, some of these materials will be described in terms of their crystal structures, electronic structures and physical properties, in an effort to highlight the different research approaches used to select, design, modify and optimize these materials.

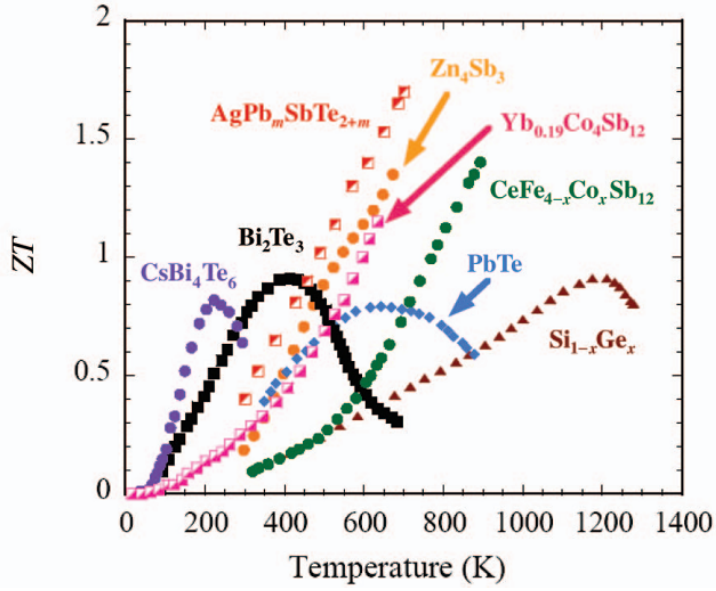

Figure 1.9. Figure of merit ZT of several state-of-the-art thermoelectric materials.[3]

1.4.2 Clathrates

As a specific guideline to decouple the electrical conductivity and the thermal conductivity, Slack has established the concept of "phonon glass and electron crystal" (PGEC).[22] In a PGEC material, the rigid cage/framework-type structure maintains a high electrical conductivity, while the heavy guest atoms loosely enclosed in the crystalline cage/framework act as phonon scattering centers and give rise to a glass-like thermal conductivity.[22]

This approach has lead to the studies of the clathrate compounds for thermoelectric performances. The clathrates feature large metal atoms enclosed in a framework of tetrahedrally coordinated main group elements, such as Al, Ga, Si, Ge or Sn. There is a number of structure types associated with the clathrates. Figure 1.10 illustrates the structures of the Type-I and Type-II clathrates with the general formula of A_8E_{46} and $A_{24}E_{136}$ (A = guest metal atoms, E = framework atoms), respectively.[30] Regardless of their

structures, the Zintl concept dictates that the electropositive *A* atoms transfer their valence electrons to the *E* atoms so they can form a three-dimensional anionic framework.[31] As a result, in a clathrate the framework dominates the electronic band structure so that the guest atoms have minimal impact on its electrical conductivity as long as the charge balance is maintained.[32]

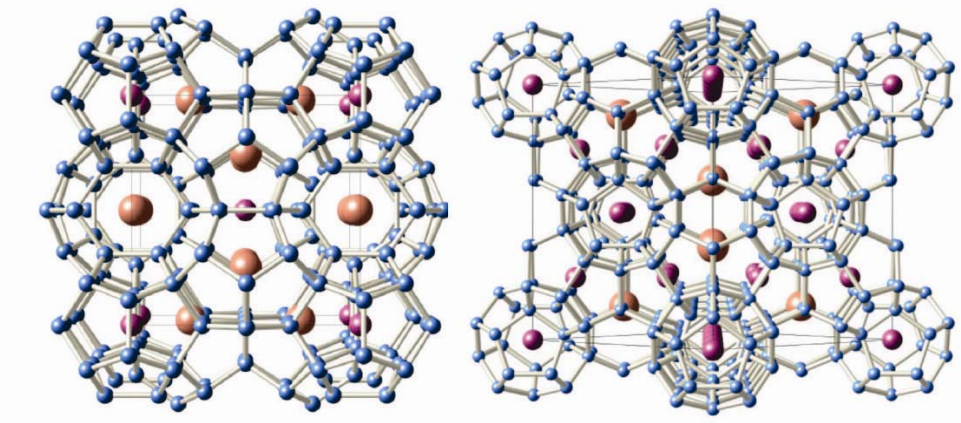

Figure 1.10 Crystal structures of the type I (left) and type II (right) clathrates.[30]

The guest atoms, however, do interact with phonons in the crystal lattice. The weak guest-framework bonding interactions allow the massive guest atoms to "rattle" in their cages. Since the localized atomic vibrations can efficiently scatter the heat-carrying acoustic phonons, the lattice thermal conductivities of the clathrate compounds are significantly reduced.

The electrical conduction through the framework and the phonon scattering by the guest atoms allow the clathrate compounds to exhibit the "phonon glass and electron crystal" behaviors. Nevertheless, the PGEC concept can be generalized to other systems where the crystalline electrical conductivity coexists with glass-like thermal conductivity which arises from defects, disorder and atomic displacement.

1.4.3 β-Zn_4Sb_3

β-Zn_4Sb_3, with a thermal conductivity as low as 0.9 W/mK at room temperature, can be considered a "phonon glass" without a "rattling" guest atom. The foundation of the low thermal conductivity in β-Zn_4Sb_3 is its disordered structure. The basic Zn_4Sb_3 structure contains one Zn and two Sb positions and adopts the *R*-3*c* space group. Study by Snyder *et al.*[33] suggested the structure in fact includes three extra interstitial sites randomly occupied by Zn atoms at 4-6%, while the Zn site in the basic structure displays a 10% vacancy. In addition to the large degree of randomness in the β-Zn_4Sb_3 lattice, the atomic misplacements also create local structural disorder around the interstitial Zn sites.[34] As a result of the combined effect, β-Zn_4Sb_3 exhibits a glass-like thermal conductivity which in turn contributes to its high thermoelectric performances. The effects of atomic displacement and disorder were exploited in the context of this thesis in order to achieve glass-like thermal conductivities in crystalline semiconductor materials. The interesting thermal transport behaviors in the RE_2SbO_2 and RE_3SbO_3 (*RE* is rare-earth elements) systems will be discussed in details with respect to their structural features.

1.4.4 Bi_2Te_3

Other thermoelectric phases without glass-like thermal conductivities can still achieve high *ZT* through optimized electrical properties. Solid solutions based on the Bi_2Te_3 system are most well studied thermoelectric materials. Some of these compounds have been successfully developed and implemented in commercial products. The pristine Bi_2Te_3 adopts a layered structure with the *R*-3*m* space group (Figure 1.11). The Bi and Te

layers form a stack with the Te–Bi–Te–Bi–Te sequence and the neighboring stacks are held together by van der Waals interactions.[4] The covalent Bi–Te bond gives rise to the high charge carrier mobility in Bi_2Te_3, while the van der Waals type Te−Te interaction causes the low thermal conductivity along the *c*-axis.[3] The Bi_2Te_3 system is remarkably robust towards doping, so that both *p* and *n*-type thermoelectric elements can be prepared from Bi_2Te_3. While the electrical properties of Bi_2Te_3 are optimized through doping, partial atomic substitutions by Sb and Se further reduce the lattice thermal conductivity through phonons scattering. The optimum compositions for bulk applications are $Bi_2Te_{2.7}Se_{0.3}$ (*n*-type) and $Bi_{0.5}Sb_{1.5}Te_3$ (*p*-type) with *ZT* above 1 near room temperature.[3]

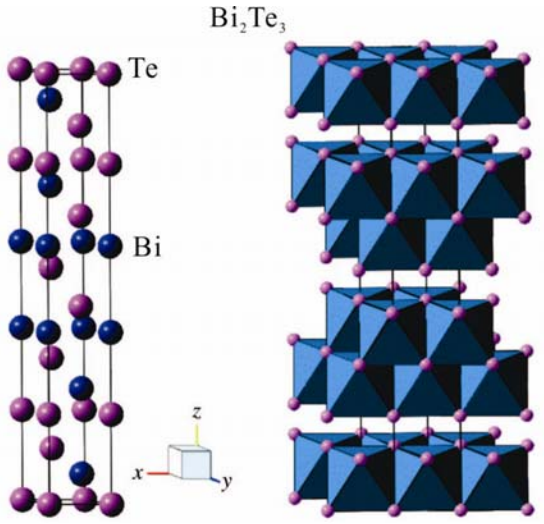

Figure 1.11 Crystal structure of Bi_2Te_3.

An important feature of Bi_2Te_3 is the low electronegativity difference between its two chemical constituents. Slack[22] has demonstrated that as charge carriers propagate through a solid, there is a charge transfer between the atoms with different electronegativity values and the amount of charge transfer increases with the electronegativity difference. At a finite temperature, the phonons in the system produce

modulations in the local electrostatic field and thus cause an increased charge carrier scattering. As a result, the charge carrier mobility decreases in a compound composed of elements with large electronegativity differences. This conclusion has lead us to study superlattice structures in which electrical conduction takes place in a sublattice with dominant covalent interactions.

1.4.5 Natural Superlattices

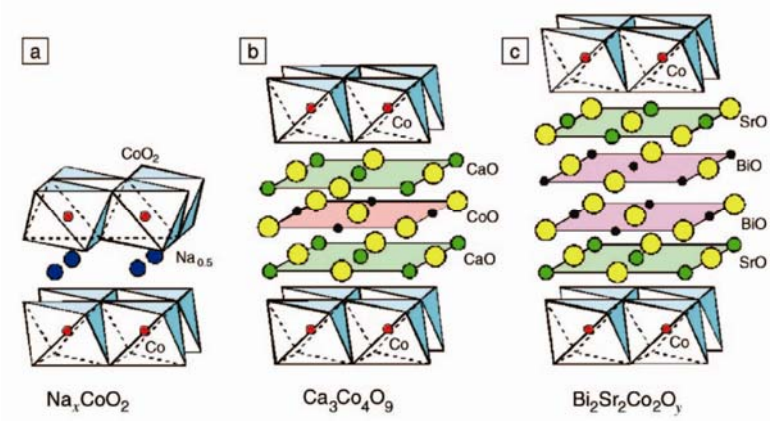

Figure 1.12 Crystal structures of Na_xCoO_2 (a), $Ca_3Co_4O_9$ (b) and $Bi_2Sr_2Co_2O_y$ (c).

The idea of constructing a superlattice to achieve high thermoelectric efficiency was first successfully demonstrated in a number of metal oxides including Na_xCoO_2, $Ca_3Co_4O_9$ and $Bi_2Sr_2Co_2O_y$ (Figure 1.12).[35] Since each of these phases is a homogeneous bulk material whose structure consists of at least two distinctly different building blocks, they are given the name of natural superlattice to differ from the thin film superlattice. An individual build block in the natural superlattice is not a single coordination polyhedron but rather a "nanoblock" with its own composition and symmetry (Figure 1.13). When integrated into a superlattice, each block can retain its desirable physical properties, which in turn contribute to the overall thermoelectric performance of the material.

Intuitively, a good thermoelectric material can be constructed from a narrow-band-gap semiconductor offering excellent electrical properties, and a thermally insulating phase, which acts as phonon barriers.

In addition to the freedom of combining structurally different components, the natural superlattice approach also allows one to control the stacking sequence between the building blocks through the composition. The Ruddlesden–Popper phases, with a common formula of $SrO(SrTiO_3)_n$ (n is an integer), are homogonous superlattices based on the $SrTiO_3$ and the SrO nanoblocks. The composition of each phase in the series depends on the number of $SrTiO_3$ layers, n, sandwiched between two SrO layers.[35] Such a gradual structural modification can be utilized as an extra leverage to optimize the thermoelectric properties in the superlattice systems.

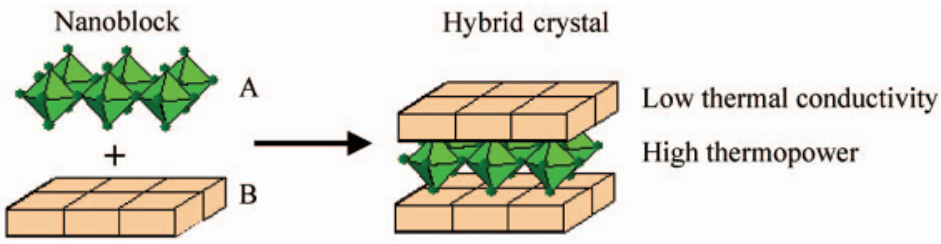

Figure 1.13 Schematics of nanoblock integration.

Fabricating superlattice phases from chemically different species also allow one to modify each building block independently. An example of such modifications can be observed in the $Ca_xYb_{1-x}Zn_2Sb_2$ system, whose structure can be regarded as a superlattice of Zintl-type $(Zn_2Sb_2)^{2-}$ layers stacked with cationic Ca^{2+}/Yb^{2+} layers in an alternating fashion (Figure 1.14). Varying the Ca:Yb ratio in the cationic layers allows a gradual change in charge carrier concentration, but brings a limited impact to the electronic band

structure and the charge carrier mobility, as these parameters are determined by the unperturbed $(Zn_2Sb_2)^{2-}$ sublattice. In addition, the Ca/Yb substitution also creates a random mass differentiation which yields a modest reduction of the thermal conductivity by interrupting phonon propagation in the lattice. The net result of the chemical modification is an increased *ZT* value, since the electrical conductivity is improved without significantly compromising the Seebeck coefficient.[25, 36]

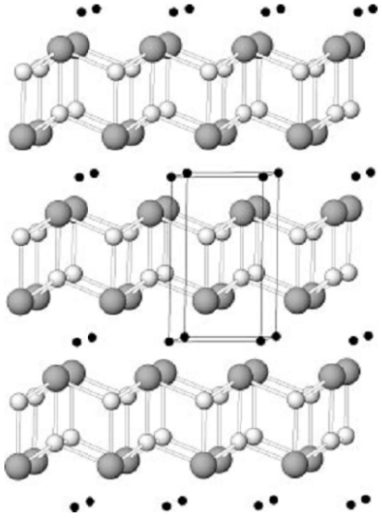

Figure 1.14. Crystal structure of $Ca_xYb_{1-x}Zn_2Sb_2$. The Ca/Yb atomic sites are shown as small black spheres, Zn and Sb are shown bonded in layers as dark and light gray spheres, respectively.[36]

Some of the research works discussed in the later sections of this dissertation were inspired by the natural superlattice approach. Other interesting features of the superlattices, such as directly and indirectly altering the sublattice structures, are also explored.

1.5 Materials in Focus

Our approaches to high efficiency thermoelectric materials are inspired by the theories and concepts described above but not restricted to these well established solid state systems. The main theme of this dissertation is the exploration, construction and modification of the complex crystal structures based on rare-earth oxides and rare-earth antimonides in an effort to produce desirable thermoelectric properties.

The advantage of incorporating rare-earth (*RE*) elements into a thermoelectric material lies with their uniform chemical properties. The ability of choosing a rare-earth element with a particular size allows the physical properties of a compound to be altered from a purely structural perspective without disturbing its chemical and electronic nature.[37] The rare-earth mono-antimonides (*RE*Sb) were selected as the starting points for thermoelectric phases because of their interesting chemical and physical properties. The pristine rare-earth mono-antimonides are semimetals[38, 39] which contain some of the heaviest elements in the periodic table. Also, these phases are well known for their high thermal stability[38] due to the strong *RE*-Sb bonds. As shown in equation 1-6 and Figure 1.7, such a high thermal stability is favorable for thermoelectric applications since a larger temperature gradient can be applied to the material. However, none of these binary compounds were found suitable for thermoelectric applications as their metallic-type electronic structures compromise their thermopower[38, 40]. In addition, the *RE*Sb binaries, adopting a simple NaCl-type crystal structure, are expected to possess a relatively high thermal conductivity due to the small number of atoms in their unit cells[41, 42]. In order to

utilize the *RE*Sb binaries for thermoelectric applications, their electronic and crystal structures have to be modified while their thermal conductivities have to be reduced.

A chemical approach to produce narrow-band-gap semiconductors from semimetallic *RE*Sb binaries is to combine them directly with electrically insulating rare-earth oxides. The oxides, RE_2O_3, are expected to increase the ionic character of the system, and thus produce novel semiconducting compounds. Although this empirical route was more of an exploration than a design, none of the phases included in this work were produced from uncontrolled oxidation of *RE* and Sb metal, since the fully oxidized rare-earth antimony oxides, such as $RE_3Sb_5O_{12}$ and RE_3SbO_7 etc[43-45] are electrical insulators. In spite of the different stoichiometries and structures, the phases depicted in the following sections are non-fully-oxidized rare-earth antimonide oxides, where the anionic characters of antimony and metallic/semiconductor properties were preserved.

1.5.1 The RE_3SbO_3 and $RE_8Sb_3O_8$ compounds

Fusing the *RE*Sb binaries and the respective RE_2O_3 oxides at high temperatures (1350°C−1600°C) led to the discovery of the novel rare-earth antimonide suboxides, RE_3SbO_3 and $RE_8Sb_3O_8$. Both of these systems adopt new crystal structures which can be considered as frameworks of RE_4O tetrahedra with Sb atomic chains enclosed in one-dimensional channels. The RE_3SbO_3 compounds are iso-electronic, but not iso-structural with the RE_3NS_3 compounds[46-48]. Some similarities have been observed between the two structures, such as the channels alone the 010 direction filled with pnictogen atoms (Figure 1.15). While the RE_3SbO_3 compounds can be considered as stable combinations of *RE*Sb and RE_2O_3 at a 1:1 ratio, the $RE_8Sb_3O_8$ phases form when some *RE* and O is lost

from the RE_3SbO_3 system. The crystal structure of $RE_8Sb_3O_8$ is similar to that of RE_3SbO_3 in terms of the building blocks and their arrangement. The one-dimensional channels along the 010 direction of $RE_8Sb_3O_8$ accommodate 3 Sb chains while only 2 Sb chains were observed in RE_3SbO_3. As discussed in Section 1.4, the overall structural complexity in these phases was expected to have a positive effect on their thermoelectric properties. However, we found that some subtle local structural details have a profound impact on the compounds' electronic structures. As a result, the $RE_8Sb_3O_8$ compounds display semiconducting properties despite of their non-charge-balanced formula. The phase formations, crystal structures, electronic structures and physical properties of the RE_3SbO_3 and $RE_8Sb_3O_8$ phases are further discussed in Chapter 3, in an effort to elucidate the relationship between the local structural features and the transport behaviors of these suboxides.

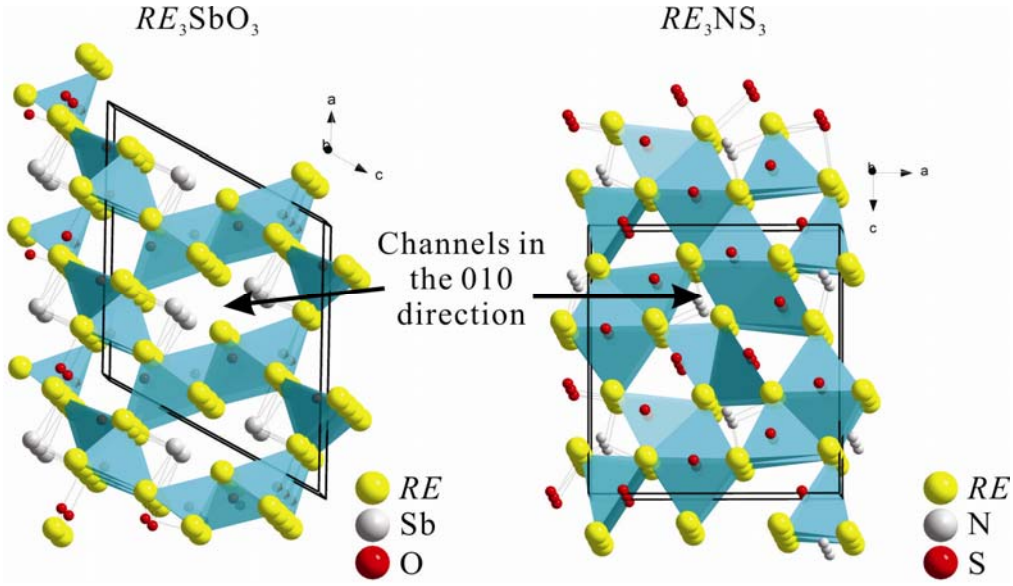

Figure 1.15. Crystal structure of RE_3SbO_3 and RE_3NS_3.

1.5.2 The *RE*Sb/*RE*-O-C Natural Superlattices

As illustrated in Section 1.4.5, a more elegant way to combine the *RE*Sb binaries and their respective oxides is to construct natural superlattices, which preserve the structural features of each component. Following this approach, a part of this work is devoted to the studies of the partially oxidized rare-earth (*RE* = Ho, Dy, Er) antimony oxycarbides, including $RE_9Sb_5O_4C$, $RE_{9-\delta}Sb_5(O,C)_5$, $La_{14}Sb_8O_7C$ and $RE_{14}Sb_{10}O_4C$.

The compounds with the common formula $RE_9Sb_5O_5$ (*RE* = La, Pr, Sm, Dy, Tb) were first studied by Nuss *et al.*,[49] and were reported to adopt a tetragonal symmetry with *P*4/*n* space group. Their structure was understood as a variant of the Sc_2Sb structure,[50] which consists of a layer Sc atoms sandwiched between the ScSb slabs. In the case of $RE_9Sb_5O_5$ phases, the interlayer between the *RE*Sb slabs has 4 *RE* atoms occupying four out five possible metal positions while the interstitial sites are stuffed with O atoms[51]. Experimental evidence suggested possible carbon substitution on the square pyramid voids within the RE_4O_5 layer. As a result, the true compositions of these phases are $RE_9Sb_5O_4C$.

Similar to the Ruddlesden–Popper phases, it is possible to obtain other structures by changing the stacking sequence of the *RE*Sb and RE_4O_4C "nanoblocks" (see Section 1.4.5). The $RE_{14}Sb_{10}O_4C$ phases can be constructed by stacking one RE_4O_4C layer with two slabs of *RE*Sb on each side, while $RE_{19}Sb_{15}O_4C$ may form with lower oxide content. The general formula of this type of phases is $(RE_5Sb_5)_n(RE_4O_4C)$, where integer, *n*, is the number of RE_5Sb_5 slabs between the neighboring RE_4O_4C layers. In addition, a number of structural variants of $RE_9Sb_5O_4C$ were discovered depending on the carbon content.

Similar to the $RE_9Sb_5O_4C$ structure, these variants consist of one *RE*-O-C layer between the neighboring RE_5Sb_5 slabs. However, the different carbon concentration in the *RE*-O-C layers forces them to adopt different symmetries.

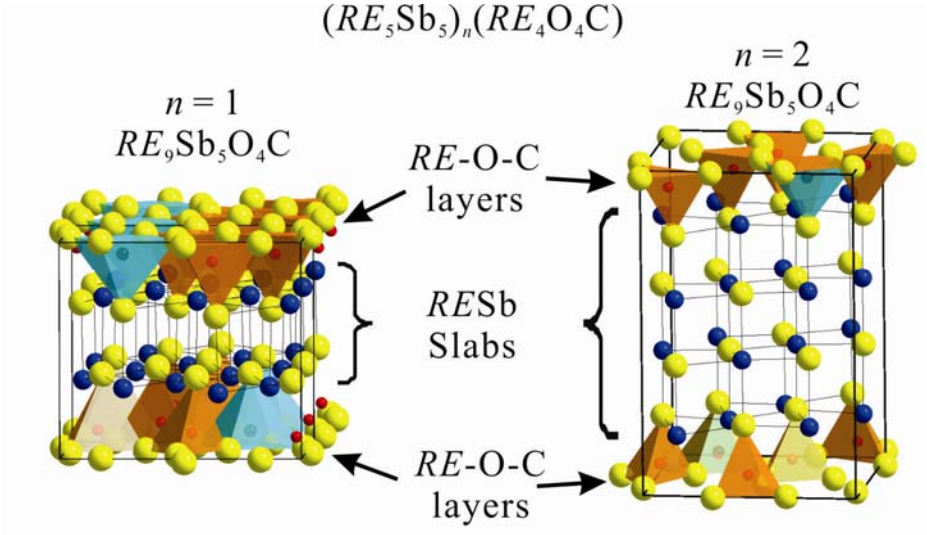

Figure 1.16. Crystal structure of $RE_9Sb_5O_4C$ (left) and $RE_{14}Sb_{10}O_4C$ (right)

As natural superlattices, these phases consist of slabs of NaCl-type *RE*Sb and layers of *RE*-O-C, as shown in Figure 1.16. These two distinctly different building blocks are expected to function differently within the structure. The *RE*Sb slabs are expected to retain the high electrical conductivity, while the *RE*-O-C layers should perform like thermal insulators to suppress overall thermal conductivity. However, in order to develop these compounds for thermoelectric applications, the relationships between the carbon concentration and the structures has to be well understood. More importantly, the O/C substitution allows the electrical properties of these compounds to be adjusted in favor of good thermoelectric performance. Chapter 4 focuses on the synthesis, compositions and structural characterization of the $RE_9Sb_5O_5$/$RE_9Sb_5O_4C$ (*RE* = La, Ho) phases.

1.5.3 The *Anti*-$ThCr_2Si_2$ Type RE_2SbO_2 Phases

Another route to a high *ZT* value involves optimizing the electrical transport properties of the thermoelectric material. However, few guidelines have been given to resolve the conflict between the electrical conductivity (σ) and the Seebeck coefficient (α) (see Section 1.3.1). Attempts to achieve a preferable electronic structure are made through the exploration of new material classes.[4] Unfortunately, it is difficult to predict the structures and compositions of the desired thermoelectric phases, and the development of new classes of materials has been rather unsystematic.[3] Therefore, much of the current research focuses on the manipulation of carrier concentration and electronic structure of an established system through doping and atomic substitution.

Our approach to the desired electrical properties involves constructing a natural superlattice, in which one sublattice (*A*) dominates the electronic structure at the vicinity of the Fermi level, while the other sublattice (*B*) displays a high tolerance for chemical manipulation. Chemically, the atomic interactions in sublattice *A* should be covalent in nature since the small electronegativity difference promises high charge carrier mobilities similar to that of the Bi_2Te_3 (see Section 1.4.4). The sublattice *B*, in addition to its chemical versatility, should exhibit ionic bonds so that its electronic states are far from the Fermi level on the energy scale. Consequently, the electrical properties of the compound can be gradually modified through the chemistry of sublattice *B* without directly perturbing the electronic structure determined by sublattice *A*. A good example of such a system is illustrated in Section 1.4.5, in the $Ca_xYb_{1-x}Zn_2Sb_2$ system, the substitution of Ca^{2+} by Yb^{2+} in the cation sublattice gradually affects the carrier

concentration, while the band gap and carrier mobility determined by the covalent $Zn_2Sb_2^{2-}$ network remain unchanged. [36]

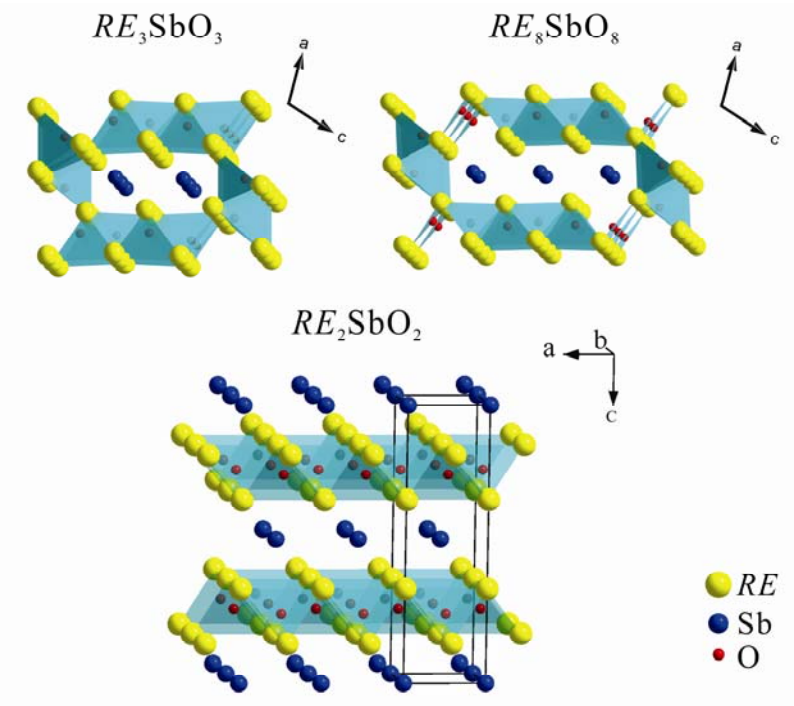

Figure 1.17. The crystal structure of RE_2SbO_2 compared to the structural units in the RE_3SbO_3 and RE_8SbO_8 phases.

Following this structural design strategy, we have centered our investigations on the RE_2SbO_2 series which can be considered as superlattices of alternating RE_2O_2 and Sb layers. The studies on the Bi analogs, RE_2BiO_2, have suggested that the electronic structure is dominated by the covalent Bi layer,[52] likewise the covalent interactions in the Sb sublattice were believed to govern the transport properties of the RE_2SbO_2 compounds. With the chemical versatility of the rare-earth series, the RE_2SbO_2 system becomes an ideal test ground for electronic band structure engineering.

In terms of structure and composition, the RE_2SbO_2 phases are closely related to the RE_3SbO_3 and RE_8SbO_8 phases. In fact, the RE_2SbO_2 structure can be derived from the

RE_3SbO_3 structure by fitting an infinite number Sb atomic chains into the RE_4O framework (see Figure 1.17). The first member of the series, Ce_2SbO_2, adopts an *anti*-$ThCr_2Si_2$ type structure with the $I4/mmm$ space group.[53] The detailed X-ray single crystal analysis conducted on Ce_2SbO_2 and Pr_2SbO_2 revealed that the Sb atoms sandwiched between the RE_2O_2 layers were shifted away from the ideal 2*a* position into an 8*i* position with the site occupancy of ¼ (Figure 1.18). Such a structural disorder was thought to enable the formation of Sb–Sb interactions in the *ab*-plane and consequently give rise to the observed semiconducting behaviors.[54] Although the large electrical resistivity of Ce_2SbO_2 and Pr_2SbO_2 renders them unfavorable for thermoelectric applications, the size differences between the rare-earth elements provide another leverage to finely adjust the electrical properties of these phases.

As we embarked on the quest to explore the physical properties of the RE_2SbO_2 compounds for potential thermoelectric applications, a variety of exotic electrical transport behaviors were discovered in the RE_2SbO_2 compounds as a function of the *RE* atomic radii. In Chapter 5, the synthesis, local structural details, electronic structures and the physical properties of the RE_2SbO_2 phases were analyzed in an attempt to elucidate the complex charge carrier transport mechanisms in the disordered Sb sublattice.

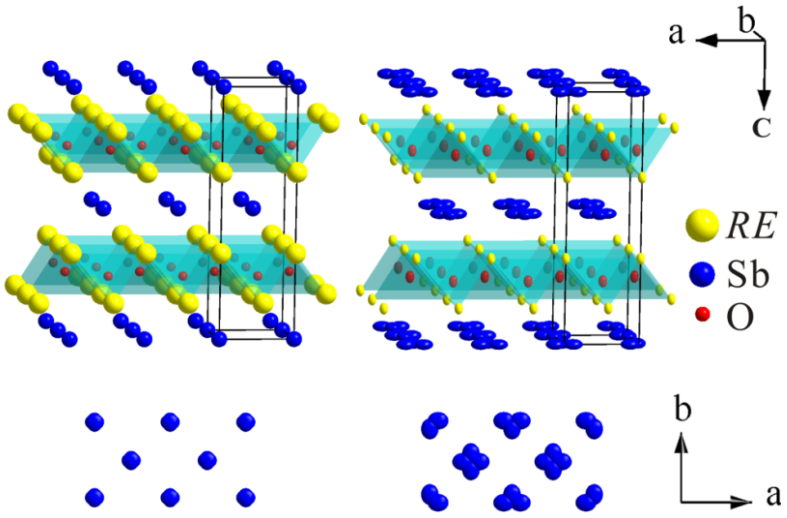

Figure 1.18. The RE_2SbO_2 structural models with the Sb atom on the 2*a* (left) and 8*i* (right) position.

Chapter 2. Methodology

2.1 Synthesis

Sample preparation is the first step in the studies of a solid state compound system.[55] Within the framework of this dissertation, different solid-state synthetic techniques and strategies were employed to prepare the targeted compounds in high purity and high crystallinity for physical property measurements and structural studies. While the synthetic details of each phase are discussed separately in the following chapters, the general considerations for synthesizing the rare-earth antimony suboxides/oxycarbides include sample oxidation, loss of volatile elements, and formation of competing products, decomposition and impurity stabilization.

Figure 2.1. The *RE*Sb binary precursors before (top) and after (bottom) sintering.

One common theme of the syntheses is the preparation of the *RE*Sb binary precursors. The *RE*Sb binaries were prepared by direct sintering of the elements. Mixtures of the filed rare-earth metals and powdered elemental antimony in the 1:1 atomic ratio were pressed into 1g pellets in an Ar-filled glove box. The samples were

sealed in evacuated silica tubes 10-15cm in length, then heated to 600 °C at a rate of 50 °C /hour (Figure 2.1, top). The sintering temperature was maintained at 600 °C to allow antimony to react with the rare-earth elements. After 12 hours, the temperature was raised to 850 °C at 50 °C /hour and held for 48 hours to drive the reaction to completion. Black pellets were obtained after cooling in air (Figure 2.1, bottom). As shown in Figure 2.2, the purity of these binaries was confirmed by powder X-ray analysis, and no significant impurity was detected.

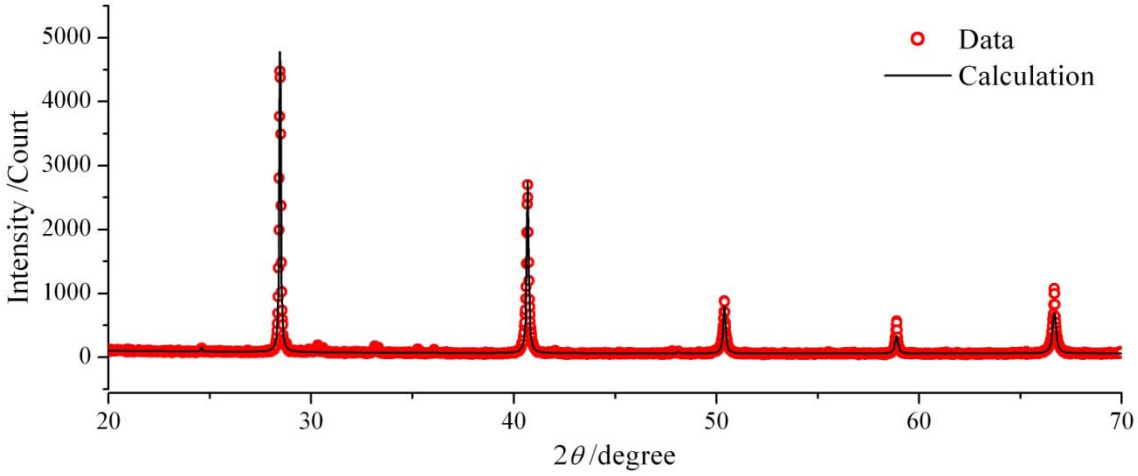

Figure 2.2. Powder X-ray diffraction and Rietveld refinement of SmSb.

The high thermal stability of the *RE*Sb binary precursors[38] is important in the preparation of the rare-earth antimonide suboxides/oxycarbides. Due to the exceptionally high thermal stabilities of the rare-earth oxides, RE_2O_3,[56] the heat treatments of the samples commonly involve sintering at temperatures over 1100 °C. By using the thermally stable *RE*Sb binaries, loss of volatile antimony, e.g. due to reaction with the sample containers, can be prevented before the desired reactions take place at the high temperature.

Since silica softens at these temperatures, more elaborated experimental setups were designed to fabricate the rare-earth antimonide suboxides/oxycarbides. Instead of silica tubes, the samples were sealed in tantalum tubes under argon by an electric arc. Then the samples were placed into a molybdenum susceptor and heated in a high-frequency induction furnace under dynamic vacuum. The reaction temperatures were monitored by an optical pyrometer. At the end of each heat treatment, the samples were left to cool to room temperature under dynamic vacuum. Such a setup (Figure 2.3) allows the high reaction temperatures to be achieved in a short period of time with no risk of oxidation.

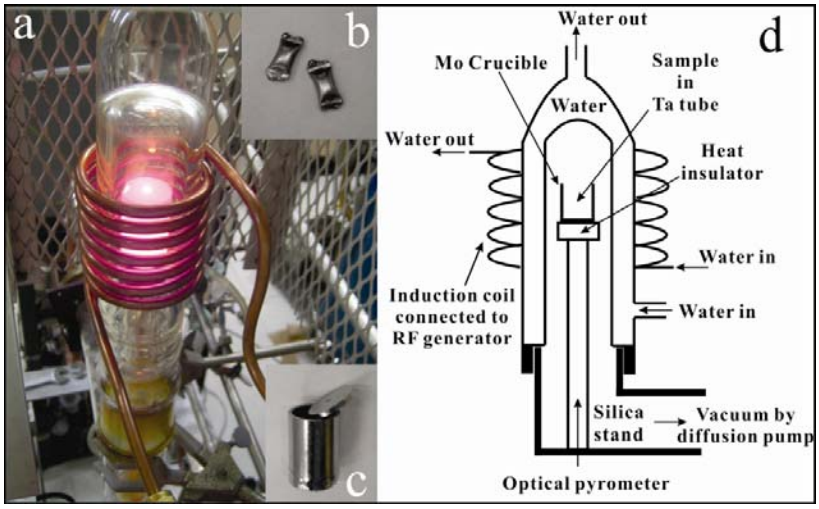

Figure 2.3. The high frequency induction furnace in operation (a). The sealed Ta ampoules (b) and the Mo receiver crucible (c) are shown. The entire setup is described in the schematics (d).

While the optimized sintering conditions for each phase are described separately in the following chapters, in some cases, the bulk and crystalline samples of the same phase were prepared differently. Using the thermally stable precursors, the high-temperature treatments produce the desired bulk products in high purities. However, such synthetic routes usually yield less crystalline samples due to the high thermal stability of the *RE*Sb

binary precursors. Occasionally, the samples with elemental *RE* and Sb were directly subjected to the high-temperature treatments. These samples tended to exhibit a better crystallinity as the molten metals act as a flux for crystal growth before they were consumed in the chemical reaction. The purity of these samples were sacrificed as the reactions between Sb and the Ta ampoule occurred at lower temperatures and Ta_3Sb[57] was produced as a side product.

2.2 X-ray diffraction techniques

One major theme of solid state chemistry research is to establish relationships between the composition, structure and the physical properties of a material. X-ray diffraction techniques are crucial in such a process since they allow the determination of 3-dimesional atomic arrangements in a crystalline solid. Moreover, the unique atomic arrangements (structures) of solid phases can be used to resolve the different chemical components in a bulk sample through X-ray diffraction.

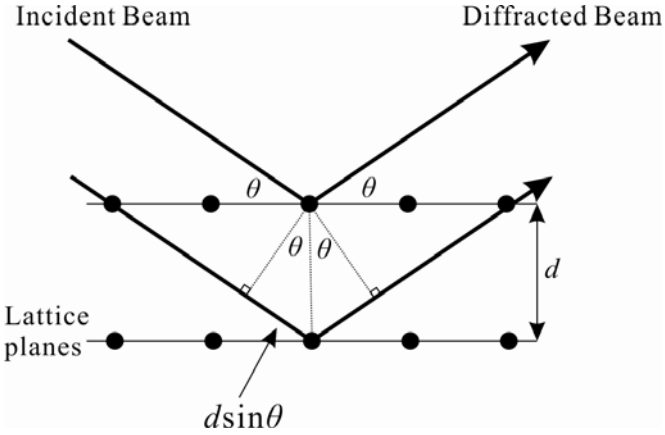

Figure 2.4. Illustration of the Bragg's law. Constructive interference occurs as the path difference between two beams ($2d\sin\theta$) equals to the wavelength λ.[58]

X-ray can be used to probe the atomic-scale structures since its wavelength is comparable to the typical periodicities in crystalline solids. As an electromagnetic wave, X-ray can be scattered by the electron clouds of atoms in an elastic fashion. However, intensity of the scattered beams is usually weak due to the destructive interference between the out-of-phase waves. The constructive interference of the scattered waves only occurs when the distance between atomic planes (d) and the X-ray wavelength (λ) satisfy the Bragg's law:

$$n\lambda = 2dsin\theta \tag{2-1}$$

Where integer n is the diffraction order and the Bragg angle θ is half of the angle between incident and diffracted beam with respect to the atomic planes (Figure 2.4).[58]

Since the angle (θ), at which the constructive interference (diffraction) occurs, is related to the distances between atomic planes (d), information of the crystal lattice can be extracted. The Miller indices h, k and l are integer numbers referring to the frequencies of a specific atomic plane intercepting the unit cell along the a, b and c directions, respectively. The reciprocal lattice (a^*, b^*, c^*) is related to its real space analog ($\vec{a}$, $\vec{b}$, $\vec{c}$) by these vectors,

$$a^* = \frac{b\times c}{V}, b^* = \frac{a\times c}{V}, c^* = \frac{b\times a}{V} \tag{2-2}$$

where V is the volume of the unit cell. In order to relate the d-spacing extracted from the diffraction angle, θ, to the indices of the lattice planes (h k l) through the reciprocal lattice (a^*, b^*, c^*), the mathematical description of Ewald's sphere has to be introduced. The Ewald's sphere is a reciprocal sphere defined by the propagation vector of the incident beam, $\boldsymbol{k}$. As shown in Figure 2.5, the absolute value of $\boldsymbol{k}$ equals to the inverse of the

incident wavelength $1/\lambda$, and in the case of elastic scattering, the scattered wave denoted by ***k'*** possesses the same absolute value. If we consider vectors ***k*** and ***k'*,** separated by 2θ**,** share the center of the Ewald's sphere, according to Bragg's law the diffraction in the ***k'*** direction must occur on the surface of the Ewald's sphere. Intuitively, the propagation vector from ***k*** to ***k'***, G_{hkl}, has an absolute value equal to the inverse of the *d*-spacing, $1/d_{hkl}$. Since G_{hkl} is vector in the reciprocal lattice, it can be expressed by the Miller indices of the planes and the reciprocal lattice parameters as

$$G_{hkl} = ha^* + kb^* + lc^* \tag{2-3}$$

Thus, vector $1/G_{hkl} = d_{hkl}$ is normal to the (h, k, l) planes in real space and $|d_{hkl}|$ equals to the distance between these atomic planes.[58, 59]

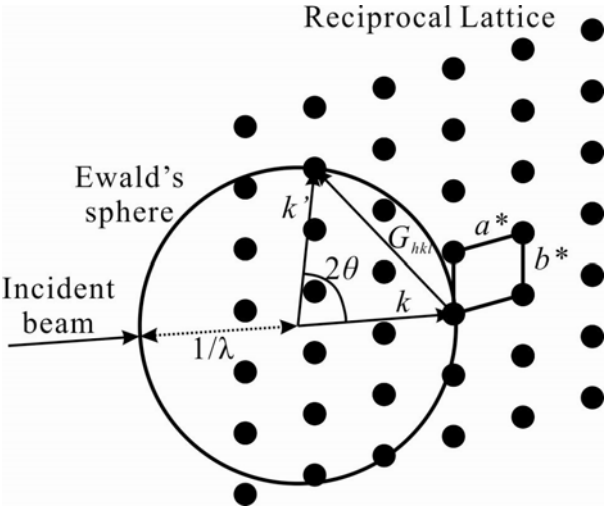

Figure 2.5. Two-dimensional Ewald's sphere and the reciprocal lattice.[58]

Since each point in the reciprocal lattice results from the X-ray beam diffracted by a set of atomic planes sharing the (h k l) indices, the intensity of a lattice point is determined by the identity of the atoms and their relative positions to the plane. The observed intensity is proportional to the square of the structure factor of the atomic plane.

The structure factor, F_{hkl}, is the sum of atomic scattering factors, $f_i(s)$, modified by an exponential function of the positions of each atom (x_i, y_i, z_i) and the corresponding Miller indices (h, k, l):

$$F_{hkl} = \sum_{i=1}^{n} f_i(s) g_i t_i(s) e^{2\pi \mathbf{i}(hx_i + ky_i + lz_i)} \quad (2\text{-}4)$$

where g_i is the occupancy factor, $t_i(s)$ is the temperature factor and (s) is the function of $sin\theta/\lambda$. The factor **i** in the above equation equals to the square root of -1, thus creating a real and imaginary part of the structure factor through the Euler expansion, $e^{ix} = cosx + isinx$. Thus, the expression of structure factor becomes:

$$F_{hkl} = \sum_{i=1}^{n} f_i(s) g_i t_i(s) \cos[2\pi(hx_i + ky_i + lz_i)] \; + \boldsymbol{i} \sum_{i=1}^{n} f_i(s) g_i t_i(s) \sin[2\pi(hx_i + ky_i + lz_i)] \quad (2\text{-}5)$$

Mathematically, the complex number F_{hkl} can be considered as a vector with projections on the real and imaginary axis. The angle between the F_{hkl} vector and the real axis, ψ, is called the phase angle. The intensity of the diffracted beam, I, can be transformed into electron density in the real space through Fourier transformation. However, since the intensity, I, is proportional to $|F_{hkl}|^2$, the phase angle, ψ, is lost. Thus, such mathematical complication prevents the determination of absolute atomic coordinates.[59]

The two most popular approaches to solve the phase angle problem are the direct and Patterson methods. The direct method statistically assigns the initial phase angle and expands it using three non-symmetrically related reflections. Among the three reflections, the phase angle of one reflection can be derived from the other two reflections. A number of phase angles can be assigned until a reasonable solution is found. The Patterson

method directly determines the positions of heavy atoms from the distribution of inter-atomic vectors in the unit cell. [59]

The initial structural solution obtained from either method has to be compared to the observed intensities so that modifications and improvements can be made on the structural model. The process of structural refinement is crucial for the analyses of both X-ray single crystal and powder diffraction data. In each refinement cycle, the least-squares method is used to determine the difference between the observed intensity and that calculated from the structural model. The structure model is then modified manually or automatically to minimize such differences in the next refinement cycle. Agreement factors, R, can be obtained based on the amplitude of the structure factor $|F_{hkl}|$. [58]

Although the basic theory of diffraction is the same for the single crystal and powder techniques, the sample preparations, instruments, data processes and analyses are different in order to fulfill a diversity of experimental objectives.

2.2.1 X-ray single crystal diffraction

Within the scope of this dissertation, X-ray single crystal diffraction experiments were performed on crystals extracted from the crushed samples. These particles were generally 10-50 μm in size and they were mounted on glass capillaries under optical microscopes. The glass capillaries with selected crystals were mounted on the goniometer head which rotates along two angles (φ and ω). Such setups (Figure 2.6) allow the diffraction data to be collected within the whole reciprocal sphere.

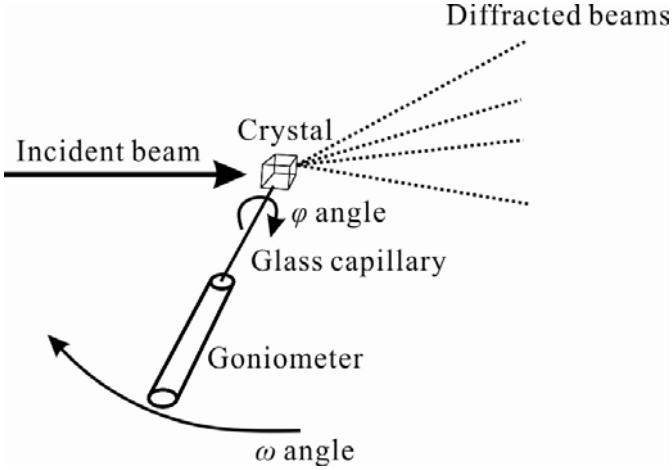

Figure 2.6. Schematics of the X-ray single diffraction setup.

The primary instrument for the room temperature diffraction experiments was a STOE IPDSII diffractometer with MoK_α radiation. A numerical absorption correction was based on the crystal shape that was originally derived from the optical face indexing but was later optimized against equivalent reflections using STOE X-Shape software[60]. The low temperature (100K) data were collected on a Bruker SMART Apex II CCD diffractometer (MoK_α radiation). Intensities were extracted and then corrected for Lorentz and polarization effects through the SAINT program[61]. Numerical absorption correction was based on the crystal shape obtained from optical face indexing. The typical data frames collected from the image plate detector (STOE IPDSII diffractometer) and the CCD detector (Bruker SMART Apex II CCD diffractometer) are shown in Figure 2.7. Structural determinations and refinements for all the rare-earth antimonide suboxides/oxycarbides phases were performed using the SHELXL program.[62]

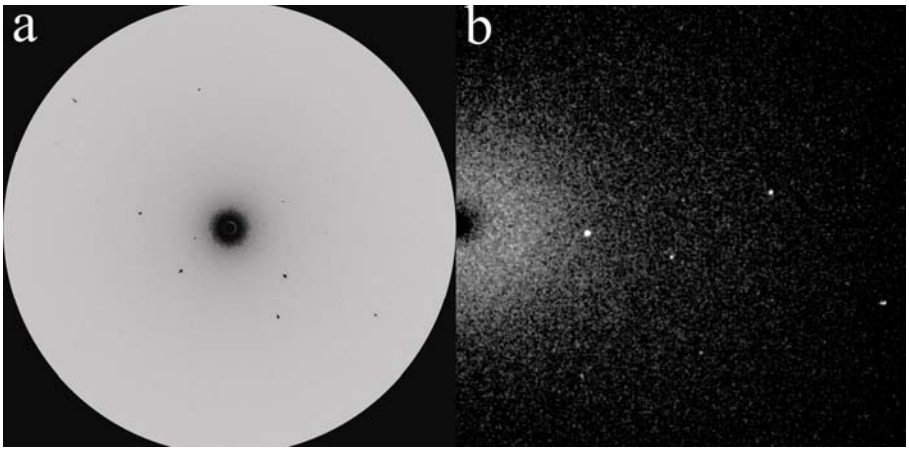

Figure 2.7. Typical data frames collected from the image plate detector (a) and the CCD detector (b).

2.2.2 X-ray powder diffraction

While the X-ray single crystal diffraction allows structure determination based on individual single crystals, the chemical compositions of the bulk materials have to be resolved in order to produce high purity samples for physical property measurements. Thus, powder X-ray diffraction technique was utilized for analysis of bulk samples of the rare-earth antimonide suboxides/oxycarbides phases.

The polycrystalline samples subjected to powder diffraction analysis are composed of many small crystallites with random orientations. When exposed to an incident X-ray beam, numerous diffracted beams can be detected at each diffraction angle θ that satisfies Bragg's Law. In the reciprocal space, the diffraction vectors of all the atomic planes in all crystallites form concentric cones as shown in Figure 2.8.[58] Thus, the powder diffraction data appears to be concentric rings on a 2-dimensional detector. In order to minimize the background signal, one-dimensional line detectors are usually used for the collection of powder X-ray data.

All the bulk materials described in this work were subjected to powder X-ray diffraction experiments on a PANalytical X'Pert Pro diffractometer with Cu$K_{\alpha 1}$ radiation. Between 20 to 50 mg of sample were used for each data collection. The finely ground powders were uniformly deposited on the surface of single crystal silicon or quartz wafers. The wafers were cut in a selected orientation so that no diffraction by the wafers would interfere with the data collection. The Cu$K_{\alpha 1}$ wavelength was produced by passing the Cu radiation from the source through a germanium single crystal monochromator. A divergence slit of 1° is used to suppress the background signals at low angles. The diffraction data in the 20–70° 2θ range were collected by an X'Celerator detector, which consists of multiple independent detection channels to obtain high intensities with minimal collection time. The full-profile Rietveld refinement (Rietica program[63]) was used to refine the structure models obtained from X-ray single crystal diffraction against the X-ray powder diffraction data.

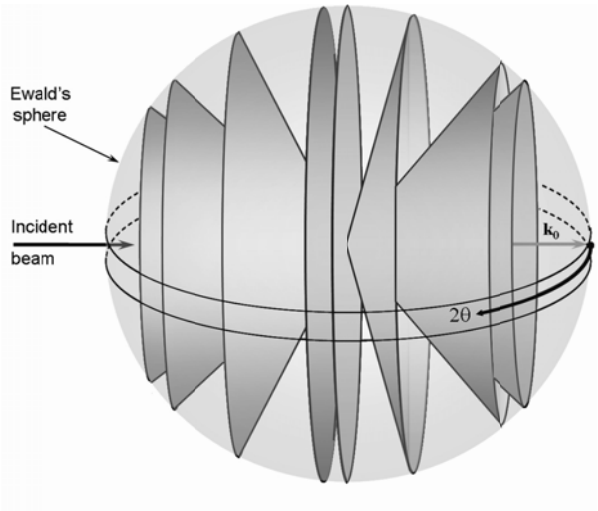

Figure 2.8. Intersection of concentric cones of diffraction vectors and the Ewald's sphere.[58]

2.3 Energy-dispersive X-ray spectroscopy and Electron Micro-Probe Analysis

Although the X-ray diffraction techniques are able to resolve the average structures of single crystals and reveal different chemical phases in bulk materials, these refinement-based methods are less effective for direct elemental analyses, especially when atomic disorder or elements with similar scattering factors are present. In order to verify the sample compositions and test for possible contaminations, bulk sample pieces and single crystals of the prepared phases were analyzed by energy-dispersive X-ray spectroscopy. Energy-dispersive X-ray spectroscopy relies on the unique atomic structure of each element to resolve the chemical composition of a sample. An electron beam is used to eject a ground state core electron in an atom thus leaving an electron hole. As an electron from an outer, higher-energy shell relaxes to fill the hole, an X-ray beam is released. The wavelength of the released X-ray corresponds to the energy difference between the two states. Since the energy differences between the electron shells are unique for different elements, the intensity and energy of the emitted X-ray can be used to determine the chemical composition of the sample.[64]

The EDS experiments were conducted on a JEOL 7000F scanning electron microscope. Copper metal was used to standardize the signals. Single crystals and powder clusters extracted from the bulk samples were mounted on the sample holder with carbon tapes. Scanning electron microscope images of single crystal and powder samples are shown in Figure 2.9 along with a typical X-ray spectrum of the EDS analysis.

Qualitative information obtained from these experiments was analyzed in conjunction with the structural solutions obtained from the diffraction techniques.

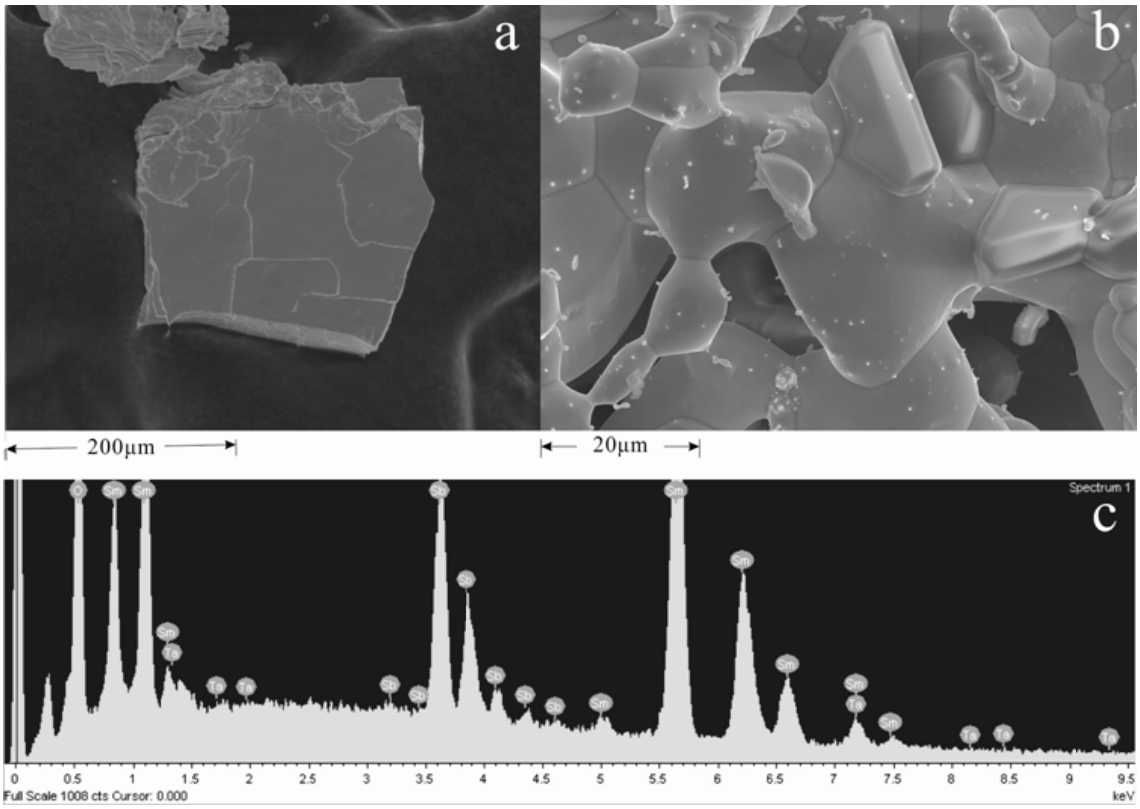

Figure 2.9. Scanning electron microscope images of a single crystal ($Ho_9Sb_5O_4C$ sample) (a) and powder grains (Sm_3SbO_3 sample) are shown, with a typical EDS spectrum (c).

The quantitative elemental analysis of selected samples was performed by electron probe microanalysis (EPMA) using wavelength dispersive (WDS) X-ray spectroscopy (Model JXA-8500F, JEOL, Tokyo, Japan). Samples were mounted in an epoxy resin 1 inch in diameter and 10 mm in thickness (Figure 2.10). The surface of the samples were exposed and polished by ~10 μm diamond dust. Antimony metal, $Sm_3Ga_5O_{12}$ and HoP_5O_{14} were used as standard materials to determine the concentration of Sb, Ho and Sm in the RE_3SbO_3 and $RE_8Sb_3O_8$ samples.

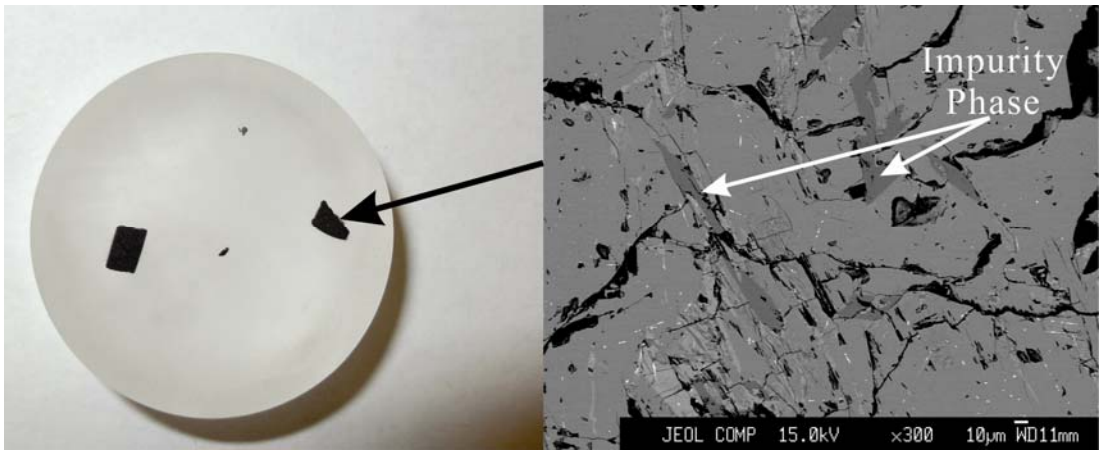

Figure 2.10. EPMA samples mounted in epoxy resin (left) and the scanning electron microscope images of the polished sample surface (right).

2.4 Physical property measurements

To study the thermoelectric properties of the rare-earth antimonide suboxides/oxycarbides phases, the electric conductivities, Seebeck coefficients and thermal conductivities of the bulk samples were measured. The cold pressed and subsequently sintered samples were cut into rectangular bars with size about 1.5cm× 0.3cm×0.3cm on a low-speed saw. Kerosene was used as lubricant and cooling agent to prevent oxidation on the exposed sample surfaces. Four-probe DC electrical resistivity was measured on a Quantum Design Physical Properties Measurement System (QD, USA) in the temperature interval of 2-400 K. Gold wires of 50 μm diameter were attached to the samples using silver ink. To confirm that the resistivity at low temperatures was not attributed to the grain boundaries but was a true bulk property of the samples, complex impedance analysis of selected samples was performed at 3-300K and AC frequency range of 10^2 -20^6 Hz using an Agilent E4980 Precision LCR Meter (Agilent, USA).

2.5 Electronic structure calculations

The objective of this study is not only to measure the physical properties of the rare-earth antimonide suboxides/oxycarbides phases, but also to link the observed physical behaviors to the structural features of these compounds. Therefore, electronic band structure calculations were employed to establish the structure-property relationships.

Tight-binding, linear-muffin-tin-orbital calculations using the atomic sphere approximation (TB-LMTO-ASA)[65] were performed for the RE_2SbO_2, RE_3SbO_3 and $RE_8Sb_3O_8$ phases with the Stuttgart program.[66] The single crystal lattice and atomic parameters were used during calculations. Exchange and correlation were treated by the local density approximation (LDA).[67] All relativistic effects except spin-orbit coupling were taken into account by using a scalar relativistic approximation.[68] In the ASA method, space is filled with overlapping Wigner-Seitz (WS) atomic spheres, the radii of which were obtained by requiring the overlapping potential to be the best possible approximation to the full potential. To satisfy the overlap criteria of the atomic spheres in the TB-LMTO-ASA method, empty spheres were included in the unit cell employing an automatic sphere generation.[69] The *f*-electrons of the rare-earth elements were treated as core electrons. Further details of the electronic structure calculations including the construction of super structures and the disagreement between the theoretical and experimental results are discussed separately for each compound series in the following chapters.

Chapter 3. Structure, Bonding and Electrical Resistivity of Novel Semiconducting Suboxides RE_3SbO_3 and $RE_8Sb_{3-\delta}O_8$

This chapter encompasses the manuscript "Structure, Bonding and Electrical Resistivity of Novel Semiconducting Suboxides RE_3SbO_3 and $RE_8Sb_{3-\delta}O_8$ with *RE* = La, Sm, Gd, Ho", published in the Journal of the American Chemical Society (*J. Am. Chem. Soc.* **2010**, 132 (25), 8795-8803). The candidate carried out the synthetic experiments with the assistance of Mr. Scott Forbes. The structure determinations, electronic structure calculations and data interpretations were also accomplished by the candidate. Dr. Taras Kolodiazhnyi measured the physical properties of the bulk samples, while Dr. Kosuke Kosuda performed electron micro-probe analyses on selected samples.

In the search of high-temperature thermoelectric materials, two families of novel narrow-band semiconducting suboxides with the RE_3SbO_3 and $RE_8Sb_{3-\delta}O_8$ compositions (*RE* = La, Sm, Gd, Ho) have been discovered. Their synthesis was motivated by attempts to open a band gap in the semimetallic *RE*Sb binaries through chemical fusion of *RE*Sb and corresponding insulating RE_2O_3. Because of the high thermal stability of *RE*Sb and RE_2O_3, temperatures of 1350°C or higher are required to prepare these phases. Both RE_3SbO_3 and $RE_8Sb_{3-\delta}O_8$ adopt new monoclinic structures with the *C*2/*m* space group and feature similar *RE*O frameworks composed of "RE_4O" tetrahedral units. In both structures, the Sb atoms occupy the empty channels within the *RE*O sublattice. High-purity bulk Sm and Ho samples were prepared and subjected to electrical resistivity measurements. Both the RE_3SbO_3 and $RE_8Sb_{3-\delta}O_8$ (*RE* = Sm, Ho) phases exhibit a semiconductor-type electric behavior. While a small band gap in RE_3SbO_3 results from the separation of the valence and conduction bands, a band gap in $RE_8Sb_{3-\delta}O_8$ appears to result from the Anderson localization of electrons. The relationship between the composition, crystal structures and electrical resistivity is analyzed using electronic structure calculations.

3.1 Introduction

Thermoelectric materials are able to perform cooling or heating when an electrical current is applied (Peltier effect) or to generate a voltage under a temperature gradient (Seebeck effect)[1]. Thermoelectric devices offer many advantages over competing technologies in terms of durability, reliability and ease of use. The limitation of current

thermoelectric materials is their efficiency. A good thermoelectric material has to have a large Seebeck coefficient α and a low thermal conductivity, κ, while retaining a high electric conductivity σ^2. Narrow-band-gap semiconductors are electronically favored for thermoelectric applications as they offer optimized thermopower α and electrical conductivity σ[7, 22].

Different strategies have been employed to reduce lattice thermal conductivity in order to achieve higher thermoelectric efficiency. Generally, commercial thermoelectric materials like Bi_2Te_3-based materials[70, 71] are composed of heavy elements which decrease lattice thermal vibrations[22]. Complex crystal structures, such as that of $Yb_{14}MnSb_{11}$[72], can also be used to minimize thermal conductivity, since the efficiency of phonon propagation is inversely related to the number of atoms in the unit cell.[22] Furthermore, atomic partial occupancy and structure defects in some systems, for instance in "*β*-Zn_4Sb_3"[73, 74], have been shown to disturb the phonon propagation. As a result, such materials exhibit low thermal conductivity similar to glasses while maintaining the electrical conductivity of a crystalline solid.[22]

Rare-earth (*RE*) monoantimonides may be of particular interest for the thermoelectric applications as they contain some of the heaviest elements in the periodic table. However, these phases, adopting a simple NaCl-type crystal structure, are expected to possess a relatively high thermal conductivity due to the small number of atoms in their unit cells[41, 42], thus some structural modifications will be required to make them competitive. The *RE*Sb binaries posses large thermal stabilities due to the strong *RE*-Sb bonds present in the NaCl-type structure; most of the *RE*Sb binaries melt above 2000°C.[38]

Thus there is a potential for using them or their derivatives for high-temperature applications. In terms of the electronic properties, rare-earth monoantimonides are semimetallic compounds[39] in which the top of the conduction band and the bottom of the valence band are situated in different parts of the momentum space (at different *k* vectors) resulting in the "negative" indirect band gap[40]. Because of this feature, the pristine binaries are unsuitable for thermoelectric applications as their metallic-type electronic structures compromise their thermopower.[38, 40] In order for the *RE*Sb phases or their derivatives to be competitive, both their electronic and thermal properties have to be optimized. One of the possible chemical approaches to produce narrow band-gap semiconductors from *RE*Sb binaries is to combine them with electrically insulating rare-earth oxides RE_2O_3. One can argue that strong interactions between the oxygen and rare-earth atoms will push up the conduction band, composed primarily of the antibonding rare-earth states, and thus will open a band gap. Thermal conductivity of the resulting phases is expected to be reduced due to an increased structural complexity. Also the new phases may be thermally stable as the strong *RE*-Sb and *RE*-O bonds will be transferred into their structures.

Chemical combinations of *RE*, Sb and O have been tried before and led to the discovery of the $RE_3Sb_5O_{12}$ and RE_3SbO_7 oxides[43-45] and $RE_9Sb_5O_5$ suboxides[49, 51, 75]. The fully oxidized $RE_3Sb_5O_{12}$ and RE_3SbO_7 phases are unsatisfactory for thermoelectric applications as they are electrical insulators (their band gaps are wide). The $RE_9Sb_5O_5$ suboxides are metallic due to the presence of conduction electrons ($RE^{+3}{}_9Sb^{-3}{}_5O^{-2}{}_5(2e^-)$) and thus they are also unsuitable for thermoelectric applications. However, the $RE_9Sb_5O_5$

structures are quite interesting as they feature the NaCl-type *RE*Sb slabs that are sandwiched between the "RE_4O_5" layers.[49, 51, 75] The discovery of the $RE_9Sb_5O_5$ phases suggests that it is possible to chemically fuse *RE*Sb and RE_2O_3 binaries to obtain novel suboxides.

Considering the high thermal stabilities of the *RE*Sb and RE_2O_3 binaries, we explored high-temperature synthetic routes for new suboxides through direct combination of *RE*Sb and RE_2O_3. During such studies, we have discovered novel phases with the RE_3SbO_3 and $RE_8Sb_3O_8$ compositions (*RE* = La, Sm, Gd, Ho). This work describes the preparation, characterization, electronic structure investigation as well as some electrical properties of these suboxides.

3.2 Experimental

3.2.1 Synthesis

The starting materials were pieces of rare-earth metals (99.99 wt. %, SmartElements) and antimony (99.999 wt. %, CERAC Inc), and RE_2O_3 powders (99.99 wt. %, Rhône-Poulenc). As the first step, *RE*Sb binaries were prepared by direct sintering of the elements. Mixtures of the filed rare-earth metals and grounded antimony in the 1:1 atomic ratio were pressed into 1g pellets in the glove box. The samples were sealed in evacuated silica tubes 10-15cm in length, then heated to 600^{o}C at a rate of 50^{o}C /hour. The sintering temperature was maintained at 600^{o}C to allow the antimony to react with the rare-earth. After 12 hours, the temperature was raised to 850^{o}C at 50^{o}C /hour and held for 48 hours to drive the reaction to completion. Black pellets were obtained after cooling

in air. The purity of these binaries was confirmed by powder X-ray analysis (See Figure 2.1).

Table 3.1. Synthesis conditions and sample descriptions for the RE_3SbO_3 and the $RE_8Sb_3O_8$ phases.

Phase	Treatment 1	Treatment 2	Sample description
La_3SbO_3	2 hours at 1350°C	--	Dark silver solidified pieces
$La_8Sb_3O_8$	6 hours at 1350°C	--	Dark silver solidified pieces
Sm_3SbO_3	2 hours at 1600°C	2 hours at 1600°C	Dark silver solidified pieces
$Sm_8Sb_3O_8$	6 hours at 1500°C	6 hours at 1350°C	Dark gray pellets
Gd_3SbO_3	0.5 hour at 1600°C	0.5 hour at 1600°C	Dark gray pellets
$Gd_8Sb_3O_8$	6 hours at 1500°C	6 hours at 1500°C	Dark gray pellets
Ho_3SbO_3	1 hour at 1600°C	1 hour at 1600°C	Dark gray pellets
$Ho_8Sb_3O_8$	6 hours at 1600°C	6 hours at 1500°C	Dark gray pellets

The ground rare-earth antimonides were mixed with RE_2O_3 (Cerac Inc, 99.999%) in the 1:1 molar ratio to prepare the RE_3SbO_3 samples, and with RE_2O_3 and Sb in the 8:8:1 ratio for $RE_8Sb_3O_8$ samples. The powders were thoroughly mixed and pressed into 0.5g pellets in a glove box. The pellets were sealed in tantalum tubes under an argon atmosphere. The Ta tubes were placed into a molybdenum susceptor and heated in a high frequency induction furnace under a dynamic vacuum below 10^{-5} torr. The reaction temperature was monitored by an optical pyrometer. The RE_3SbO_3 and the $RE_8Sb_3O_8$ samples were heated between 1300°C and 1600°C. To ensure homogeneity, after the first annealing each sample was grinded and pressed in a glove box, sealed in a fresh tantalum tube and heat-treated again. At the end of each heat treat, the samples were left to cool to room temperature under dynamic vacuum. The samples were either molten after the heating or sintered into solid pellets. Varieties of temperatures and annealing times have been tested and the optimal synthetic conditions for each phase are listed in Table 3.1.

3.2.2 X-ray single-crystal diffraction and structure refinement

X-ray single crystal diffraction studies were performed on crystals extracted from the crushed RE_3SbO_3 and $RE_8Sb_3O_8$ samples (*RE* = La, Sm, Gd, Ho). Room temperature diffraction data were collected on a STOE IPDSII diffractometer with the MoK_α radiation in the whole reciprocal sphere. A numerical absorption correction was based on the crystal shape that was originally derived from the optical face indexing but was later optimized against equivalent reflections using STOE X-Shape software[60]. The data for the $Ho_8Sb_3O_8$ single crystal were also collected on a Bruker SMART Apex II CCD diffractometer (MoK_α radiation) at 100(2) K in a reciprocal hemisphere. Intensities were extracted and then corrected for Lorentz and polarization effects through the SAINT program[61]. Numerical absorption correction was based on the crystal shape obtained from optical face indexing. Due to the poor crystal quality, the $La_8Sb_3O_8$ structure could not be refined from the corresponding X-ray data, only the unit cell parameters were obtained from indexing of the Braggs peaks. Structural determinations and refinements were performed using the SHELXL program.[62] Both the RE_3SbO_3 and $RE_8Sb_3O_8$ structures adopt the *C*2/*m* space group. The room temperature (393K) crystallographic and refinement results for all phases are given in Tables 3.2 and 3.3.

Table 3.2. Crystallographic data and refinement results for the La_3SbO_3, Sm_3SbO_3, $Sm_8Sb_3O_8$, Gd_3SbO_3, $Gd_8Sb_3O_8$ Ho_3SbO_3 and $Ho_8Sb_3O_8$ single crystals, MoKα radiation (293K).

Refined composition	La_3SbO_3	Sm_3SbO_3	$Sm_8Sb_{2.976(8)}O_8$	Gd_3SbO_3	$Gd_8Sb_{2.98(1)}O_8$	Ho_3SbO_3	$Ho_8Sb_3O_8$
Space group				*C*2/*m*			
Unit cell dimensions /Å	a = 13.856(3) b = 4.1050(8) c = 12.343(3) β = 118.55(3)°	a = 13.332(2) b = 3.9501(4) c = 11.919(2) β = 118.31(1)°	a = 13.462(3) b = 3.8629(8) c = 15.230(3) β = 106.77(3)°	a = 13.272(3) b = 3.8971(8) c = 11.878(2) β = 118.40(3)°	a = 13.394(3) b = 3.8191(8) c = 15.104(3) β = 107.05(3)°	*a* = 13.014 (3) *b* = 3.8218(7) *c* = 11.680(2) *β* = 118.21(1)°	*a* = 13.137(1) *b* = 3.7609(2) *c* = 14.870(1) *β* = 106.958(7)°
Volume /Å^3	616.7(2)	552.60(1)	758.3(3)	540.4(2)	738.7(3)	511.90(2)	702.73(9)
Z	4	4	2	4	2	4	2
D_{calcd} /g cm^{-3}	6.317	7.462	7.428	7.884	7.874	8.623	8.567
Abs. coefficient /mm^{-1}	24.594	36.133	35.690	41.165	40.755	50.963	50.125
2θ range / degrees	3.35 to 32.48	3.79 to 34.45	3.07 to 34.44	4.74 to 34.39	3.58 to 37.22	3.87 to 36.85°	3.65 to 37.20°
Reflections collected	7366	3106	5656	3515	4768	3248	10299
Independent reflections	1250 (R_{int} = 0.1636)	1221 (R_{int} = 0.0547)	1667 (R_{int} = 0.0845)	1174 (R_{int} = 0.1366)	2079 (R_{int} = 0.0700)	1386 (R_{int} = 0.0731)	2022 (R_{int} = 0.0900)
Completeness to max. 2θ	99.8 %	93.6 %	93.2 %	92.7 %	97.5 %	95.8 %	99.4 %
Data / restraints / param.	1250 / 0 / 44	1221 / 0 / 43	1667 / 0 / 62	1174 / 0 / 44	2079 / 0 / 62	1386 / 0 / 44	2022 / 0 / 62
Goodness-of-fit on F^2	0.629	0.823	0.801	1.018	0.921	0.914	1.015
Final R indices [I>2σ(I)]	R_1 = 0.0486, wR_2 = 0.0589	R_1 = 0.0319 wR_2 = 0.0448	R_1 = 0.0389 wR_2 = 0.0465	R_1 = 0.0664 wR_2 = 0.1347	R_1 = 0.0462 wR_2 = 0.0874	R_1=0.0518, wR_2=0.0788	R_1=0.0410, wR_2=0.0660
R indices (all data)	R_1 = 0.1104 wR_2 = 0.0737	R_1 = 0.0654 wR_2 = 0.0500	R_1 = 0.0909 wR_2 = 0.0540	R_1 = 0.1090 wR_2 = 0.1475	R_1 = 0.0875 wR_2 = 0.0962	R_1=0.1185, wR_2=0.0943	R_1=0.0737, wR_2=0.0720
Extinction coefficient	0.00143(7)	0.00048(4)	0.00056(2)	0.0007(2)	0.00066(6)	0.00033(5)	0.00185(6)
Diffr. peak/hole / e Å^{-3}	2.615/-3.513	2.786/-4.158	3.679/-2.474	6.947/-6.426	4.415/-4.651	7.004/-7.547	4.309/-4.141

Table 3.3. Atomic and equivalent isotropic temperature (*U*) parameters for the La_3SbO_3, Sm_3SbO_3, $Sm_8Sb_3O_8$, Gd_3SbO_3, $Gd_8Sb_3O_8$ Ho_3SbO_3 and $Ho_8Sb_3O_8$ single crystals at 293(2) K.

Atom	Site	Occupancy	*x/a*	*y/b*	*z/c*	*U* (Å^2)
			La_3SbO_3			
La(1)	*4i*	1	0.6189(1)	0	0.4449(1)	0.0051(2)
La(2)	*4i*	1	0.6274(1)	0	0.8985(1)	0.0055(2)
La(3)	*4i*	1	0.1541(1)	0	0.2061(1)	0.0060(2)
Sb(1)	*4i*	1	0.1220(1)	0	0.6822(1)	0.0082(2)
O(1)	*4i*	1	0.1891(8)	0	0.4110(11)	0.008(2)
O(2)	*4i*	1	0.4367(9)	0	0.7983(12)	0.012(3)
O(3)	*4i*	1	0.1614(9)	0	0.10123(13	0.014(3)
			Sm_3SbO_3			
Sm(1)	*4i*	1	0.1190(1)	0	0.4439(1)	0.0059(1)
Sm(2)	*4i*	1	0.3435(1)	0	0.7930(1)	0.0061(1)
Sm(3)	*4i*	1	0.8725(1)	0	0.9970(1)	0.0066(1)
Sb(1)	*4i*	1	0.3809(1)	0	0.3188(1)	0.0076(1)
O(1)	*4i*	1	0.3110(6)	0	0.5906(7)	0.007(1)
O(2)	*4i*	1	0.3367(7)	0	0.9855(7)	0.010 (2)
O(3)	*4i*	1	0.9357(7)	0	0.8035(8)	0.014(2)
			$Sm_8Sb_{2.976(8)}O_8$			
Sm(1)	*4i*	1	0.7182(1)	0	0.0890(1)	0.0063(2)
Sm(2)	*4i*	1	0.4567(1)	0	0.1686(1)	0.0102(2)
Sm(3)	*4i*	1	0.8765(1)	0	0.3465(1)	0.0065(1)
Sm(4)	*4i*	1	0.6421(1)	0	0.4312(1)	0.0095(2)
Sb(1)	*4i*	1	0.1711(1)	0	0.2676(1)	0.014 (1)
Sb(2)	*4g*	0.488(4)	0	0.048(2)	0	0.014(2)
O(1)	*4i*	1	0.4683(7)	0	0.3665(11)	0.028(3)
			Gd_3SbO_3			
Gd(1)	*4i*	1	0.1198(1)	0	0.4436(1)	0.0075(2)
Gd(2)	*4i*	1	0.3435(1)	0	0.7933(1)	0.0073(2)
Gd(3)	*4i*	1	0.8722(1)	0	0.992(1)	0.0090(2)
Sb(1)	*4i*	1	0.3813(1)	0	0.3191(2)	0.0090(2)
O(1)	*4i*	1	0.310(1)	0	0.5892(13)	0.010(3)

O(2)	*4i*	1	0.338(1)	0	0.9866(13)	0.010(3)
O(3)	*4i*	1	0.936(1)	0	0.8043(16)	0.023(4)
			$Gd_8Sb_{2.98(1)}O_8$			
Gd(1)	*4i*	1	0.7189(1)	0	0.890(1)	0.0081(1)
Gd(2)	*4i*	1	0.4565(1)	0	0.1688(1)	0.0123(1)
Gd(3)	*4i*	1	0.8769(1)	0	0.3469(1)	0.0086(1)
Gd(4)	*4i*	1	0.6430(1)	0	0.4304(1)	0.0107(1)
Sb(1)	*4i*	1	0.1715(1)	0	0.2671(1)	0.0158(2)
Sb(2)	*4g*	0.488(5)	0	0.053(1)	0	0.015(1)
O(1)	*4i*	1	0.4703(9)	0	0.368(1)	0.023(3)
O(2)	*4i*	1	0.8824(8)	0	0.2016(6)	0.009(2)
O(3)	*4i*	1	0.2983(8)	0	0.677(6)	0.009(2)
O(4)	*4i*	1	0.1656(8)	0	0.5139(6)	0.008(2)
			Ho_3SbO_3			
Ho(1)	*4i*	1	0.11994(8)	0	0.4433(1)	0.0079(2)
Ho(2)	*4i*	1	0.34264(8)	0	0.79342(9)	0.0077(2)
Ho(3)	*4i*	1	0.87230(8)	0	0.09852(9)	0.0092(2)
Sb(1)	*4i*	1	0.3820(1)	0	0.3190(2)	0.0094(2)
O(1)	*4i*	1	0.313(1)	0	0.592(1)	0.007(2)
O(2)	*4i*	1	0.334(1)	0	0.983(1)	0.014(3)
O(3)	*4i*	1	0.935(1)	0	0.807(1)	0.014(3)
			$Ho_8Sb_3O_8$			
Ho(1)	*4i*	1	0.71926(4)	0	0.08908(4)	0.0072(1)
Ho(2)	*4i*	1	0.45628(4)	0	0.16929(4)	0.0111(1)
Ho(3)	*4i*	1	0.87741(4)	0	0.34761(4)	0.0074(1)
Ho(4)	*4i*	1	0.64347(4)	0	0.43042(4)	0.0086(1)
Sb(1)	*4i*	1	0.17137(6)	0	0.26664(6)	0.0130(2)
Sb(2)	*4g*	0.475(4)	0	0.050(1)	0	0.012(1)
O(1)	*4i*	1	0.4691(6)	0	0.3688(9)	0.023(2)
O(2)	*4i*	1	0.8826(7)	0	0.2018(5)	0.010(2)
O(3)	*4i*	1	0.2960(6)	0	0.0663(6)	0.008(1)
O(4)	*4i*	1	0.1649(6)	0	0.5144(6)	0.009(1)

Within the initial structural solution for the $RE_8Sb_3O_8$ crystals, Sb2 atoms were placed on the *2a* site (0, 0, 0) with 2/*m* symmetry. However, unusually large vibrations along the *b* direction suggested that the Sb2 atoms have to be moved out of the mirror plane into the 4*g* site (0, *y*, 0) with the occupancy of 50%. While split positions can indicate presence of a superstructure, we did not see any signs of a superstructure in the reciprocal space of $RE_8Sb_3O_8$. The 50% occupancy provides the right number of atoms in the unit cell and accounts for artificially short Sb2-Sb2 distances of ca. 0.4 Å. The new structural model yielded improved thermal parameters for the Sb2 sites and lower *R* values (Table 3.4). In addition, the Sb2 site is refined to be deficient. Upon releasing the Sb2 occupancies, the *R* factors were either preserved or improved while the thermal vibration parameters of Sb2 atoms were further reduced (Table 3.4). The most pronounced Sb2 deficiency was observed for $Ho_8Sb_3O_8$. During the refinement, atomic deficiencies and temperature factors are usually correlated, however they can be untangled from the high-angle diffraction data, as their contribution to the structure factor is very different at high angles. Additionally, lower temperatures decrease thermal vibrations and allow further differentiation of the two effects. The single crystal data for $Ho_8Sb_3O_8$ were recollected up to $2\theta = 90^o$ and at 100 K and they confirmed both the deficiency for and the assignment of the 4*g* site to the Sb2 atoms. Therefore, the composition of the $RE_8Sb_3O_8$ phases is given as $RE_8Sb_{3-\delta}O_8$.

Table 3.4. Effects of moving the Sb2 atom from the 2*a* site ($y = 0$) into the 4*g* site ($y \neq 0$) and refining its occupancy on the thermal vibration parameters and R_1 values for the $Sm_8Sb_3O_8$ (293 K), $Gd_8Sb_3O_8$ (293 K) and $Ho_8Sb_3O_8$ (293 K & 100 K) crystals.

Single Crystals	Sb2 site	Occupancy	y	U_{22}	U_{eq}	R_1 value
$Ho_8Sb_3O_8$ (293K)	2*a*	1.0	0.0	0.066(1)	0.0293(4)	0.0417
$Ho_8Sb_3O_8$ (293K)	4*g*	0.5	0.050(1)	0.024(3)	0.0156(9)	0.0413
$Ho_8Sb_3O_8$ (293K)	4*g*	0.475(4)	0.050(1)	0.018(2)	0.012(1)	0.0410
$Ho_8Sb_3O_8$ (100K)	2*a*	1.0	0.0	0.0592(7)	0.0234(2)	0.0399
$Ho_8Sb_3O_8$ (100K)	4*g*	0.5	0.0516(3)	0.020(1)	0.0106(3)	0.0360
$Ho_8Sb_3O_8$ (100K)	4*g*	0.473(2)	0.0516(3)	0.0166(9)	0.0084(3)	0.0353
$Sm_8Sb_3O_8$	2*a*	1.0	0.0	0.068(1)	0.0270(4)	0.0391
$Sm_8Sb_3O_8$	4*g*	0.5	0.048(2)	0.027(4)	0.013(1)	0.0389
$Sm_8Sb_3O_8$	4*g*	0.488(4)	0.048(2)	0.019(2)	0.014(2)	0.0389
$Gd_8Sb_3O_8$	2*a*	1.0	0.0	0.059(7)	0.0234(2)	0.0468
$Gd_8Sb_3O_8$	4*g*	0.5	0.053(1)	0.024(3)	0.0165(9)	0.0463
$Gd_8Sb_3O_8$	4*g*	0.488(5)	0.053(1)	0.022(7)	0.015(1)	0.0462

Bonding in the structure and its correlation with electrical resistivity are analyzed in depth in the later part of this work. Further details of the crystal structure investigations can be obtained from the Fachinformationszentrum Karlsruhe, 76344 Eggenstein-Leopoldshafen, Germany, (fax: (49) 7247-808-666; e-mail: crysdata@fiz.karlsruhe.de) on quoting the depository CSD numbers 380456 for La_3SbO_3, 380455 for Sm_3SbO_3, 380454 for $Sm_8Sb_3O_8$, 380460 for Gd_3SbO_3, 380459 for $Gd_8Sb_3O_8$, 380458 for Ho_3SbO_3 and 380457 for $Ho_8Sb_3O_8$.

3.2.3 X-ray powder diffraction

Table 3.5. Lattice constants and phase analysis from the X-ray powder diffraction data of the RE_3SbO_3 and the $RE_8Sb_3O_8$ samples (*RE* = La, Sm, Gd, Ho).

Major phase	Space Group	*a* /Å	*b*/Å	*c*/Å	*β* /°	Impurities and amount (w. t. %)	
La_3SbO_3	*C2/m*	13.847(3)	4.0913(2)	12.387(3)	117.91(7)	Mixed with $La_8Sb_3O_8$	
$La_8Sb_3O_8$	*C2/m*	13.898(2)	4.0264(4)	15.774(2)	106.26(6)	Mixed with La_3SbO_3	
Sm_3SbO_3	*C*2/*m*	13.331(7)	3.0952(1)	11.918(4)	118.31(6)	$Sm_8Sb_3O_8$	6.2(5)%
Sm_8SbO_8	*C*2/*m*	13.461(5)	3.8670(4)	15.229(3)	106.76(4)	Pure	
Gd_3SbO_3	*C*2/*m*	13.245(5)	3.9045(1)	11.847(4)	118.44(2)	Gd_8SbO_8	12.6(3)%
Gd_8SbO_8	*C*2/*m*	13.478(3)	3.8218(2)	14.972(7)	106.15(5)	Pure	
Ho_3SbO_3	*C*2/*m*	13.029(4)	3.8302(2)	11.676(3)	118.23(2)	$Ho_8Sb_3O_8$	8.9(3)%
$Ho_8Sb_3O_8$	*C*2/*m*	13.169(4)	3.7513(3)	14.907(5)	106.88(3)	HoSb	1.4(1)%

The sintered samples were subjected to X-ray powder diffraction analysis to assess their purity, derive the lattice constants and to understand the transformation pathways between the RE_3SbO_3 and $RE_8Sb_3O_8$ phases. Between 20 and 50 mg of sample were used for each data collection. Diffraction data in the 20–70° 2θ range were collected on a PANalytical X'Pert Pro diffractometer with an X'Celerator detector and a Cu$K_{\alpha 1}$ radiation. The full-profile Rietveld refinement (Rietica program[63]) was used to refine the lattice constants and amount of impurities. The structural models obtained from X-ray single crystal diffraction were used during the Rietveld refinement. (See Appendix A1.1) The lattice constants and phase analysis of the samples is provided in Table 3.5.

3.2.4 Energy-dispersive X-ray spectroscopy

In order to verify the sample compositions and test for possible contamination, bulk sample pieces and single crystals of the phases prepared were analyzed by energy-dispersive X-ray spectroscopy. The EDS experiments were conducted on a JEOL 7000F scanning electron microscope. Copper metal was used to standardize the signals. The qualitative information obtained from experiments was in agreement with the X-ray single crystal and powder diffraction results. No contamination, including Ta impurities, was observed in the RE_3SbO_3 and the $RE_8Sb_3O_8$ samples.

3.2.5 Microprobe analysis

The quantitative analysis of elemental composition of selected samples was performed by electron probe microanalysis (EPMA) using a wavelength dispersive (WDS) X-ray spectroscopy (Model JXA-8500F, JEOL, Tokyo, Japan). Samples were mounted in an epoxy resin 1 inch in diameter and 10mm in thickness. Surface of the samples were polished by ~10μm diamond dust. Antimony metal, $Sm_3Ga_5O_{12}$ and HoP_5O_{14} were used as standard materials to determine the concentration of Sb, Ho, Sm and O in the RE_3SbO_3 and $RE_8Sb_3O_8$ samples.

3.2.6 Physical property measurements

Four-probe DC electrical resistivity was measured on Quantum Design Physical Properties Measurement System (QD, USA) in the temperature interval of 2-300 K. Gold wires of 50 μm diameter were attached to the samples using silver ink. Due to irregular shape of the samples, the Y-axis error bars in Figure 3.7 correspond to around 30% of the absolute value of electrical resistivity. Quite often the high resistivity of the

polycrystalline samples originates from the scattering of the charge carriers on the grain boundaries. This effect cannot be distinguished by the DC measurements[76]. To confirm that the resistivity at low temperatures is not attributed to the grain boundaries but is a true bulk property of the samples, we performed complex impedance analysis of the $Ho_8Sb_3O_8$ at 3-300K and AC frequency range of 10^2 -20^6 Hz using Agilent E4980 Precision LCR Meter (Agilent, USA). We found no evidence of the grain boundary effect and confirmed that the reported resistivity is characteristic of the bulk of the material.

3.2.7 Electronic structure calculations

Tight-binding, linear-muffin-tin-orbital calculations using the atomic sphere approximation (TB-LMTO-ASA)[65] were performed for RE_3SbO_3 and $RE_8Sb_3O_8$ with the Stuttgart program[66]. The single crystal lattice and atomic parameters were used during calculations. Exchange and correlation were treated by the local density approximation (LDA).[67] All relativistic effects except spin-orbit coupling were taken into account by using a scalar relativistic approximation[68]. In the ASA method, space is filled with overlapping Wigner-Seitz (WS) atomic spheres, the radii of which were obtained by requiring the overlapping potential to be the best possible approximation to the full potential. To satisfy the overlap criteria of the atomic spheres in the TB-LMTO-ASA method, empty spheres were included in the unit cell employing an automatic sphere generation[69].

3.3 Results and Discussion

3.3.1 Structures

The RE_3SbO_3 and $RE_8Sb_{3-\delta}O_8$ suboxides adopt novel crystal structures with $C2/m$ symmetry (Figure 3.1). The two structures feature similar *RE*O frameworks built from RE_4O edge-sharing tetrahedra. Also, in both structures the empty channels running along the *b* direction are filled with Sb atoms. There are two types of building blocks, *A* and *B*, in the *RE*O framework of RE_3SbO_3 (Figure 3.1, left). Block *A* consists of four edge-sharing RE_4O tetrahedra and block *B* of two such tetrahedra. The two blocks, connected via corner sharing, form a 2*D* slab within the *ac* plane. These slabs stack along the *b* axis via edge sharing and form the 3*D* *RE*O framework. The empty channels within the *RE*O framework of RE_3SbO_3 are occupied by two rows of Sb atoms.

Compositionally, the RE_3SbO_3 phases are direct combination of the *RE*Sb and RE_2O_3 binaries. Thus, it is interesting to know if there are any structural similarities. Indeed, the RE_4O tetrahedra, which define the *RE*O framework of RE_3SbO_3, are also found in RE_2O_3, in fact, the entire framework of the *C*-type RE_2O_3 oxides is built from the edge-sharing RE_4O tetrahedra[77]. However, the *RE* cubic environment of the Sb atoms in RE_3SbO_3 is different from the *RE* octahedral environment of the Sb atoms in the NaCl-type *RE*Sb binaries[38]. This new coordination for Sb can be seen as a structural adaptation of the Sb atoms (and Sb–*RE* interactions) to the presence of the *RE*O framework. Similar structural relationships are observed between $RE_8Sb_{3-\delta}O_8$, *RE*Sb and RE_2O_3.

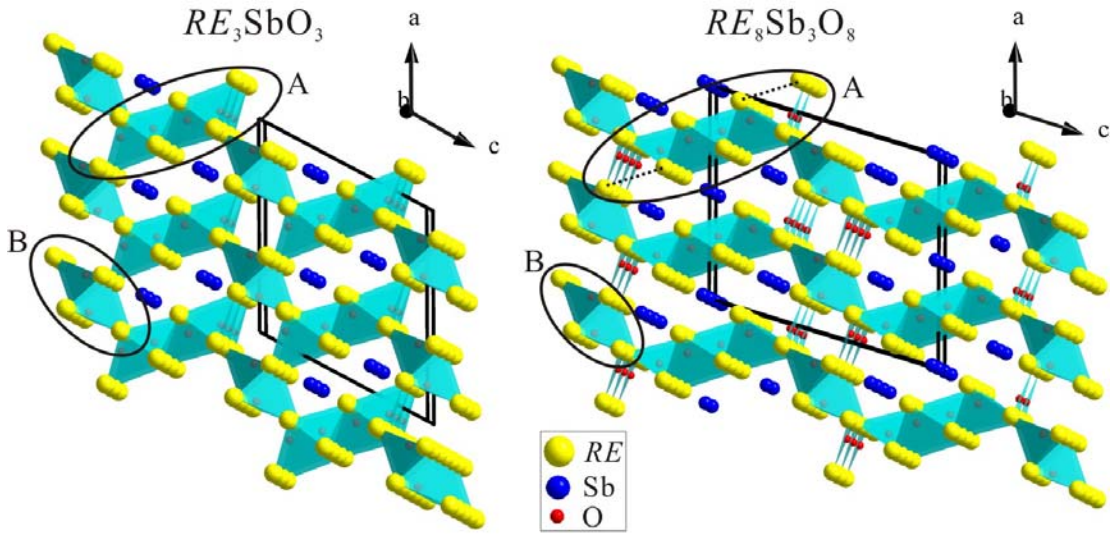

Figure 3.1. Crystal structures of the RE_3SbO_3 and $RE_8Sb_3O_8$ phases and their building blocks.

In the $RE_8Sb_{3-\delta}O_8$ structure, building block *B* of RE_3SbO_3 is retained (Figure 3.1, right), but block *A* is expanded with two additional, highly distorted RE_4O tetrahedra. E.g. in $Ho_8Sb_{3-\delta}O_8$, the longest Ho-Ho distance (a dotted line in Figure 3.1, right) in these distorted tetrahedra is 3.94(2) Å while the five other distances are within the 3.80-3.84 Å range. In addition to being strongly stretched, these RE_4O units have oxygen atoms (the O1 site) almost in the center of their terminal triangular faces. As a result, the O1 atoms adopt a rather unusual, trigonal planar environment: e.g. in $Ho_8Sb_{3-\delta}O_8$ the O1 atoms have three Ho atoms at 2.19-2.22 Å and a fourth one at 2.92 Å. Similar oxygen shifts are also observed for the terminal RE_4O tetrahedra of the *A* block in RE_3SbO_3, but they are less pronounced, e.g. in Ho_3SbO_3, the O atoms (the O3 site) have three Ho atoms at 2.21-2.23 Å and fourth one at 2.66 Å. The unusual coordination for the O1 atoms in $RE_8Sb_{3-\delta}O_8$ manifests itself in displacement parameters that are highly elongated along the normal to the *RE* trigonal face (Figure 3.2). Such behavior is due to the absence of

strong interactions outside of the trigonal face. Presence of highly elongated thermal ellipsoids at 100 K similar to the room temperature ones (Figure 3.2) further supports the argument that the origin of these vibrations lies in the unusual environment of the O1 atoms.

The extended *A* blocks of $RE_8Sb_{3-\delta}O_8$ create larger channels which are now occupied by 3 rows of Sb atoms (only such 2 rows are present in RE_3SbO_3). Conversely, it can be also argued that the extra Sb row in $RE_8Sb_{3-\delta}O_8$ puts additional pressure on the dimension of the *A* block, which results not only in the extension of this block by two RE_4O tetrahedra but also in the stretching of the terminal RE_4O tetrahedra and thus unusual bonding environment for the O1 atoms. While block *A* is larger in $RE_8Sb_{3-\delta}O_8$, connectivity between and stacking of blocks *A* and *B* is identical to those in RE_3SbO_3.

Another interesting structural feature of $RE_8Sb_{3-\delta}O_8$ is anisotropic thermal vibrations and positions of the Sb2 atoms (the central row of Sb atoms) along the *b* direction. In the original structure model with the Sb2 atoms on the mirror plane (model 1 in Figure 3.3), the Sb2-Sb2 distances equaled the *b* parameter and were identical to the Sb1-Sb1 distances. However, the thermal vibrations of Sb2 were found to be extremely elongated along the *b* direction and much larger than those of the Sb1 atoms despite the fact that the atomic environments of Sb1 and Sb2 were rather similar. Furthermore, the electron density map generated from the experimental intensities showed that the Sb2 site has a large spatial distribution along the *b* direction (Figure 3.4). In order to account for such smeared electron density, the Sb2 atoms were shifted from the mirror plane: from the *2a* site (0, 0, 0) into the 4*g* site (0, *y*, 0) (model 2 in Figure 3.3). The occupancy of the new

site was set to 50% to avoid overlapping between the Sb2 atoms, but after the refinement it became even lower (e.g. 47.3(2) % for $Ho_8Sb_{3-\delta}O_8$ at 100 K). The distribution of Sb2 above and below the mirror plane appears to be random as no superstructure could be detected and also static as the refinements of the room-temperature and 100 K data yielded identical structural models.

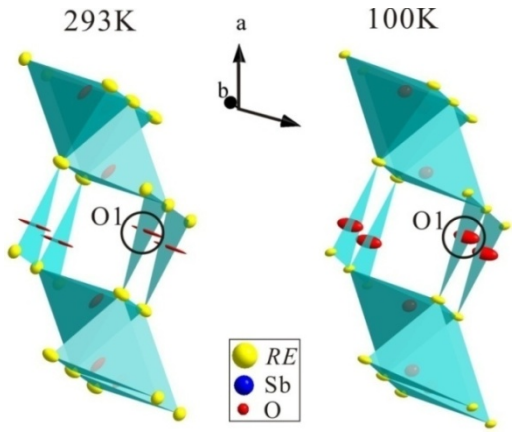

Figure 3.2. Thermal vibration (90% probability) of O1 in the structure of the $RE_8Sb_3O_8$ compounds.

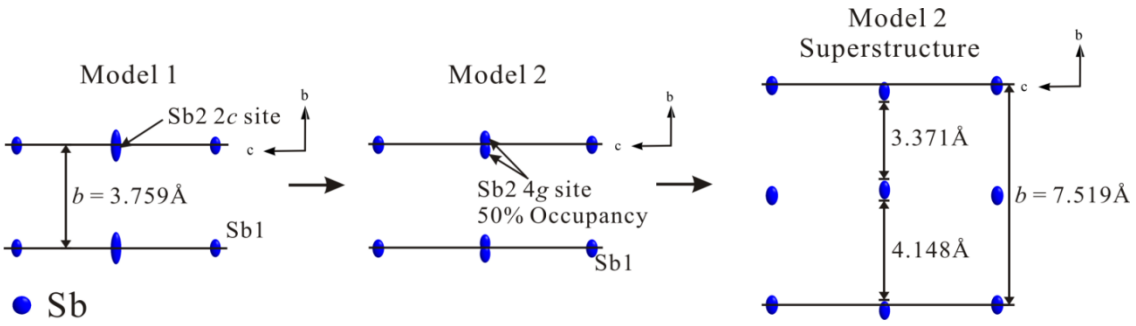

Figure 3.3. Structure models of different Sb2 positions used in the X-ray single crystal data refinements of the $RE_8Sb_3O_8$ crystals.

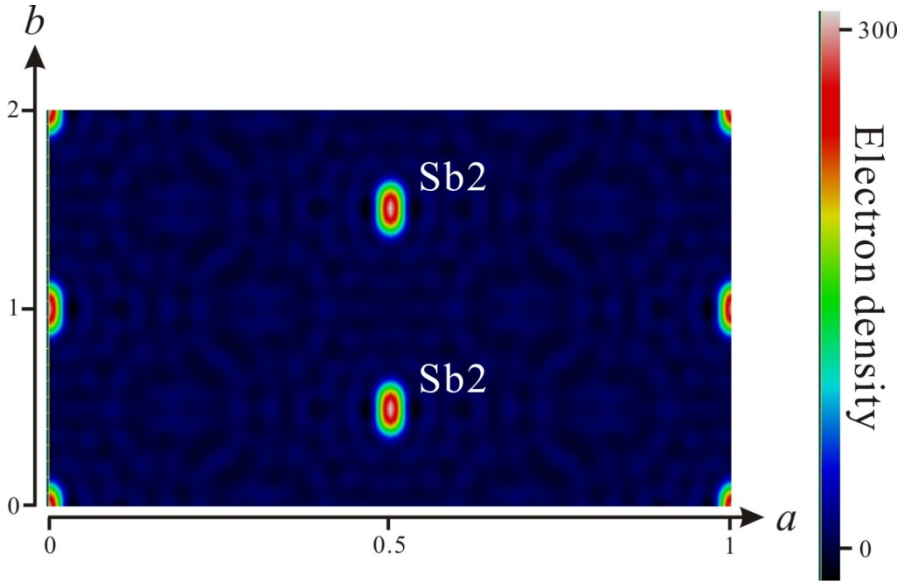

Figure 3.4. Real space electron density map obtained from the $Ho_8Sb_3O_8$ single crystal data collected at 100K.

The Sb2 shifts in $RE_8Sb_{3-\delta}O_8$ results in unequal Sb2-Sb2 distances along the *b* direction. Such distances can be visualized through the construction of a superstructure ("Superstructure" model in Figure 3.3), in which the *b* axis is doubled and half of the Sb2 atoms are removed. As mentioned above, no evidence for such a superstructure could be detected from single crystal experiments. Now, there are two distinct sets of the Sb2-Sb2 distances: longer ones of 4.148(1) Å and shorter ones of 3.371(1) Å. While the shorter distances are longer than a typical single Sb-Sb bond (e.g. $d_{Sb\text{-}Sb}$ = 2.83-2.85 Å in KSb[78]), they are indicative of increased Sb2-Sb2 interactions and, thus, of the formation of Sb2-Sb2 bonds which can be treated as elongated dimers. A similar behavior has been also observed in $Yb_{14}MnSb_{11}$[72], where a central Sb atom of the Sb_3 linear unit randomly shifts towards and form a dimer with one of the terminal Sb atoms[79]. Such random dimer formation is believed to be one of the key factors responsible for the low thermal conductivity and outstanding thermoelectric performance of $Yb_{14}MnSb_{11}$ [80].

It is worth noting that refinements of the Sb2 site for different $RE_8Sb_{3-\delta}O_8$ (RE = Sm, Gd, Ho) single crystals yielded occupancies smaller than 50%. Such deficiency does not appear to be a simple correction to the thermal motion of the atom, since the refinement on the 100 K data for $Ho_8Sb_{3-\delta}O_8$ yielded similar results. While the deficiencies are rather minor, they are statistically significant for the Gd and Ho structures and according to the Hamilton test[81] they should be accepted with a larger than 99.5% confidence level. It can be argued that formation and random distribution of the Sb2-Sb2 dimers is the cause for the Sb2 deficiencies. If all Sb2 atoms form dimers and no isolated Sb2 atoms are allowed, then a random distribution of the dimers can only be achieved if some of the Sb2 atoms are missing.

3.3.2 Stability and transformation of the suboxides

From the analysis of the products at different stages, we have observed that the formation of RE_3SbO_3 always precedes the formation of $RE_8Sb_{3-\delta}O_8$ even if the loading composition is $RE_8Sb_{3-\delta}O_8$. Also if one starts with the RE_3SbO_3 compositions, one obtains the RE_3SbO_3 phases first, which then transform into the $RE_8Sb_{3-\delta}O_8$ phases upon longer annealing. Figure 3.5 demonstrates conversion from Ho_3SbO_3 into $Ho_8Sb_{3-\delta}O_8$ as seen from X-ray powder diffraction. The loading composition of Ho_3SbO_3 yields the desired phase in high purity (>atomic 90%) after 1.5 hours of heating at 1500°C, accompanied only by small amounts of $Ho_8Sb_{3-\delta}O_8$. As the same loading composition is annealed for 2 hours at the same temperature, the $Ho_8Sb_{3-\delta}O_8$ phase starts to grow at the expense of Ho_3SbO_3. After 6 hours at 1500°C, the Ho_3SbO_3 sample yields an almost pure $Ho_8Sb_3O_8$ phase. The same trends were observed for other systems.

Thus, the $RE_8Sb_{3-\delta}O_8$ phases appear to be thermodynamically more stable under our synthetic conditions. It has also been found that transformation of RE_3SbO_3 into $RE_8Sb_{3-\delta}O_8$ occurs more fully at lower temperatures. Taking advantage of different stabilities, synthetic procedures were designed to produce either RE_3SbO_3 or $RE_8Sb_{3-\delta}O_8$ in high purity for Sm, Gd and Ho. As summarized in Table 3.1, the RE_3SbO_3 phases can be obtained from shorter treatments at higher temperature, and the $RE_8Sb_{3-\delta}O_8$ ones from longer annealing at lower temperatures. Regardless of the annealing temperature and duration, La_3SbO_3 and $La_8Sb_{3-\delta}O_8$ could be obtained only as mixtures.

The transformation and relative stability of RE_3SbO_3 and $RE_8Sb_{3-\delta}O_8$ can be explained by considering their compositions and structures. Compositionally, the RE_3SbO_3 phases are direct combinations of the *RE*Sb and RE_2O_3 binaries, and their structures are simpler than those of $RE_8Sb_{3-\delta}O_8$. Thus, during synthesis the RE_3SbO_3 suboxides appear first, but additional heat treatment permits further structural and compositional modifications towards the $RE_8Sb_{3-\delta}O_8$ phases. Since the $RE_8Sb_{3-\delta}O_8$ phases always appear as the final product, even in the RE_3SbO_3 samples, one may question their real compositions. To verify compositions, quantitative electron microprobe analysis was performed for the RE_3SbO_3 and $RE_8Sb_3O_8$ samples with *RE* = Sm, Ho. As summarized in Table 3.6, the *RE*:Sb ratios are significantly different for the RE_3SbO_3 and $RE_8Sb_3O_8$ samples (oxygen amount had to be treated with caution as the surfaces are oxidized). Therefore, the RE_3SbO_3 and $RE_8Sb_{3-\delta}O_8$ phases do possess distinct chemical compositions, i.e. they are not structural polymorphs. Also, no impurities were detected in the samples.

The RE_3SbO_3 suboxides transform into $RE_8Sb_{3-\delta}O_8$ upon prolonged annealing, however byproducts of this reaction have never been detected in the bulk samples from the X-ray powder analysis. The "missing" byproducts were found during the SEM analysis of the tantalum ampoule, in which Ho_3SbO_3 was allowed to convert into $Ho_8Sb_{3-\delta}O_8$. Small crystalline clusters about 5-10 μm in size were deposited uniformly on the inside surface of the Ta ampoule (Figure 3.6). The energy-dispersive X-ray spectroscopy analysis of these clusters yielded only Ho and O as their constituents, but their exact ratio could not be determined accurately due to the bias in oxygen content. We believe that RE_2O_3 and *RE* metals precipitate out during the $RE_3SbO_3 \rightarrow RE_8Sb_{3-\delta}O_8$ transformation.

Table 3.6 Composition of the RE_3SbO_3 and $RE_8Sb_3O_8$ samples with *RE* = Sm, Ho from the electron microprobe analysis. The elemental ratios were normalized to 3 and 8 *RE* atoms.

Elements	Atomic Percentage	Ratio	Atomic Percentage	Ratio
	Ho_3SbO_3		Sm_3SbO_3	
RE	41.5(5)	3.00(4)	41.8(5)	2.90(3)
Sb	13.7(8)	1.00(5)	14.5(8)	1.00(5)
O	44.8(7)	3.30(5)	43.7(7)	3.00(5)
	$Ho_8Sb_3O_8$		$Sm_8Sb_3O_8$	
RE	40.8(5)	8.4(1)	40.3(5)	8.0(1)
Sb	14.6(8)	3.0(2)	15.0(7)	3.0(1)
O	44.7(7)	9.2(1)	44.9(6)	8.9(1)

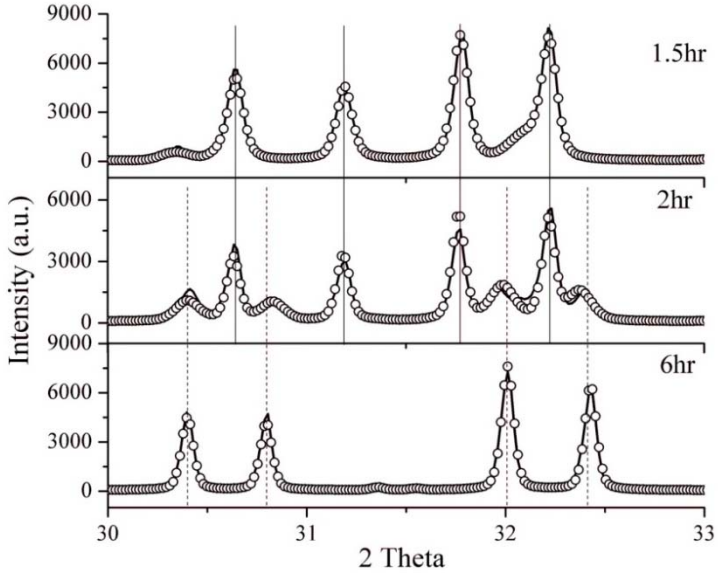

Figure 3.5. X-ray powder diffraction data of Ho_3SbO_3 samples after 1.5, 2 and 6 hours of heating at 1600℃.Dashed lines mark the peak positions of the Ho_3SbO_3 phase, and solid lines mark peak positions of $Ho_8Sb_3O_8$ phase.

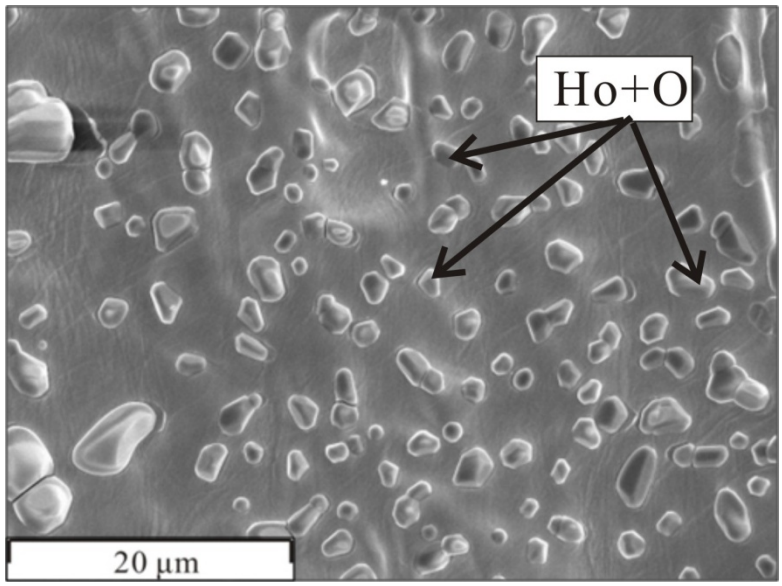

Figure 3.6. SEM image of inside surface of the Ta ampoule, in which Ho_3SbO_3 was converted into $Ho_8Sb_3O_8$.

3.3.3 Electrical resistivity

Electric resistivity measurements were performed on the Sm_3SbO_3, $Sm_8Sb_3O_8$, Ho_3SbO_3 and $Ho_8Sb_3O_8$ samples. As shown in Figure 3.7, an exponential decrease in electric resistivity indicative of a semiconducting-type behavior is observed for all samples. The room temperature electrical resistivity and band gap values are listed in Table 3.7. The band gaps were calculated from the high-temperature data assuming an Arrhenius-type behavior and two types of charge carriers. In general, the Ho samples are more conductive that the Sm analogs, besides the RE_3SbO_3 samples are more conductive than the $RE_8Sb_3O_8$ ones. Unfortunately, the room-temperature electrical conductivities for both the RE_3SbO_3 and $RE_8Sb_3O_8$ samples are 10^2-10^3 times smaller than those of the high-performance thermoelectric materials (resistivity of $Yb_{14}MnSb_{11}$ and Zn_4Sb_3 are both ~ 2mΩ cm at room temperature[72, 82]). Such low conductivities render these phases in their current state unsuitable for thermoelectric applications.

Table 3.7. Room temperature electrical resistivity and calculated and gap for samples of Sm_3SbO_3, $Sm_8Sb_3O_8$, Ho_3SbO_3 and $Ho_8Sb_3O_8$.

Parameter	Sm_3SbO_3	$Sm_8Sb_3O_8$	Ho_3SbO_3	$Ho_8Sb_3O_8$
Resistivity /Ω cm	1.03	86.3	1.05	3.34
Band Gap /eV	0.006	0.089	0.011	0.116

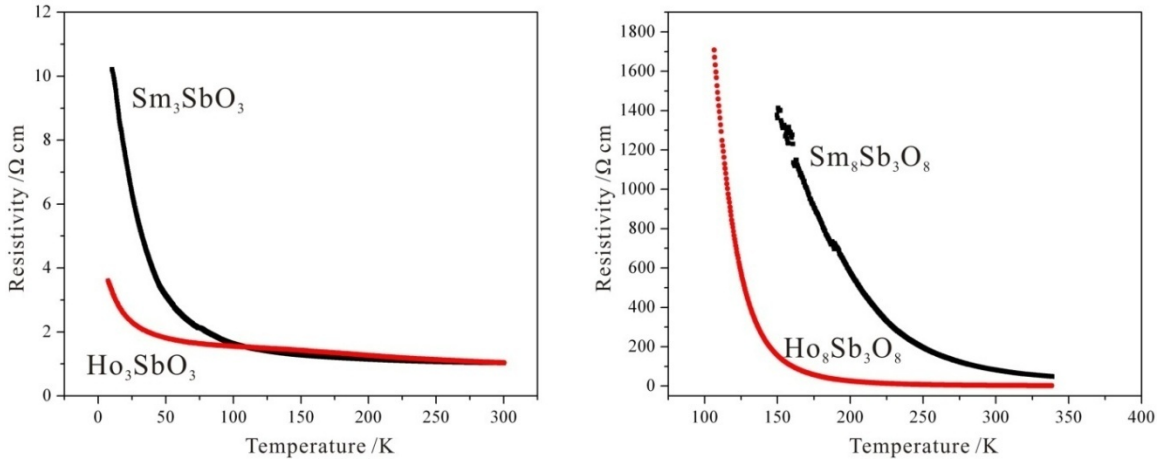

Figure 3.7. Electrical resistivity of Sm_3SbO_3 and Ho_3SbO_3 (Left). Electrical resistivity of $Sm_8Sb_3O_8$ and $Ho_8Sb_3O_8$ (Right).

3.3.4 Electronic structure of RE_3SbO_3

Qualitatively, a semiconductor behavior of the RE_3SbO_3 phases can be explained using a simple electron counting formalism. Since the *RE* atoms have no close *RE* neighbors, they can be treated as RE^{3+}. The Sb and O anions are assumed to satisfy the octet rule, and since there are no anion-anion interactions, the RE_3SbO_3 formula can be written as $RE_3^{+3}Sb^{-3}O_3^{-2}$. In terms of the electronic structure, such charge assignment would mean that the valence band composed primarily of the Sb states (O states will be lower) is fully occupied and the conduction band made primarily of the Ho states is empty. Obviously, an energetic separation between the two bands cannot be predicted from such a qualitative approach, but if a band gap is assumed, the RE_3SbO_3 phases will be semiconducting. These simple arguments are supported by the LMTO calculations for Ho_3SbO_3 (Figure 3.8). The calculated densities of states (DOS) exhibit a small band gap of 0.2 eV between the valence band dominated by the Sb *p* orbitals and the conduction band formed primarily by Ho *d* orbitals. The Fermi energy level resides at the top of the

valence band and Ho_3SbO_3 is predicted to be a small-band semiconductor, which agrees with the experimental resistivity data.

3.3.5 Electronic Structure of $RE_8Sb_{3-\delta}O_8$

Analysis of the electronic structure of the $RE_8Sb_{3-\delta}O_8$ phases is more complicated due to their increased structural complexity. For an idealized $RE_8Sb_3O_8$ structure (no Sb2 deficiencies and Sb2 on the 2*a* site, i.e. no Sb2-Sb2 dimers), the electron counting approach yields a charge *unbalanced* formula, $RE_8^{+3}Sb_3^{-3}O_8^{-2}$, and electron deficiency of $1e^-$. The Sb2 deficiency, δ, reduces the electron deficiency to $(1-3\delta)e^-$, but considering that experimental δ values are much smaller than 1/3, the $RE_8Sb_{3-\delta}O_8$ phases are predicted to be metallic. However when all Sb2 atoms are considered to form Sb2-Sb2 dimers (Sb2 on the 4*g* site), one obtains a $RE_8^{+3}Sb_2^{-3}Sb(2)^{-2}O_8^{-2}$ formula which is charge balanced (deficiency is omitted for simplicity) and the semiconducting properties can be expected. But the Sb2-Sb2 distances in $RE_8Sb_{3-\delta}O_8$ are 3.489(1) Å, 3.411(1) Å and 3.371(1) Å for *RE* = Sm, Gd and Ho, and they are much larger than the classical 2c2e Sb-Sb bonds, e.g. the Sb-Sb dimer is 2.82 Å in β-Zn_4Sb_3[80]. Such larger distances imply much weaker Sb-Sb interactions and thus additional, in excess of $2e^-$, electron requirements for the Sb2 atoms in $RE_8Sb_{3-\delta}O_8$.

The LMTO calculations support the metallic behavior of the idealized $Ho_8Sb_3O_8$ structure without Sb2-Sb2 dimers, and they also reveal some interesting details. As expected, the Fermi level sits deep in the valence band, but surprisingly, there is a non-zero DOS between the valence and conduction bands. Analysis of the partial DOS and COHP for individual interactions reveals that the weak Sb2-Sb2 interactions of 3.76 Å

are responsible for the disappearance of the band gap. This is rather remarkable as the Sb2-Sb2 distances are identical to the Sb1-Sb1 ones and the first-nearest neighbor environments for Sb2 and Sb1 are similar. Currently, we do not fully understand the origin of such behavior, but we think that the second-nearest neighbor coordination of Sb2 with fewer O atoms is responsible for the observed changes. Introducing the Sb2 deficiency of $\delta = 0.046$ in $Ho_8Sb_{3-\delta}O_8$ will raise the Fermi level through decreasing the number of the Sb2 states in the valence band, but it will not be sufficient to place the Fermi level at the top of the valence band. Besides, such deficiency even if large will not change the nature of electrical conductivity for idealized $Ho_8Sb_3O_8$ as there is no band gap.

Electronic effects of the Sb2-Sb2 dimer formation ($d_{Sb2\text{-}Sb2} = 3.37$ Å) were studied by creating a "superstructure" of $Ho_8Sb_3O_8$ in which the *b* axis was doubled and symmetry was reduced to *P*2 (see model 3 in Figure 3). Due to the shorter Sb2-Sb2 bonds ($d_{Sb2\text{-}Sb2} = 3.37$ vs. 3.76 Å), the Sb2 states originating from the Sb2-Sb2 bonding interactions dropped in energy while the antibonding states went up. As a result, a band gap opened between the valence and conduction bands. However, the Fermi level is still deep in the valence band which suggests that not enough of the Sb2 states were transferred to the higher-energy conduction band. This behavior may not be so surprising as the Sb2-Sb2 interactions are rather weak. Presence of small Sb2 deficiencies will not change the DOS significantly.

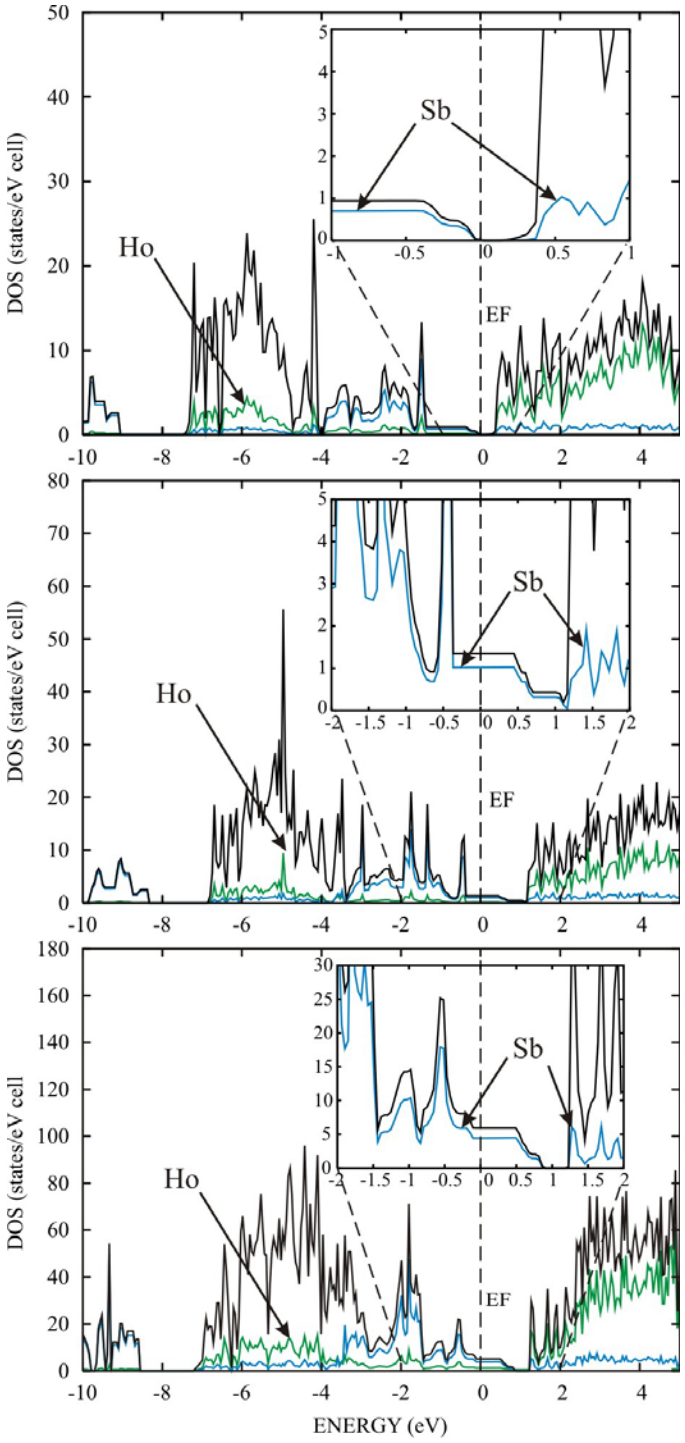

Figure 3.8. Electronic structures of the RE_3SbO_3 (top) and $RE_8Sb_3O_8$ (middle) phases and the electronic structure of the $RE_8Sb_3O_8$ phase with the "superstructure model" (bottom).

Thus, the DOS calculations point at the metallic behavior for $Ho_8Sb_{3-\delta}O_8$, though the phase is semiconducting. We suggest that semiconducting properties of $Ho_8Sb_{3-\delta}O_8$ as well as of $Sm_8Sb_{3-\delta}O_8$ result from the Anderson-type localization of electrons. According to Anderson, in disordered structures with a non-periodic potential the electrons can be localized within the vicinity of a particular atom[83]. Crystal orbitals in such crystals are divided into two types: those in the middle of the band extend through the solid as in a normal crystal, and those close to the top and bottom of the band are localized. The region of localized states in the band will depend on the degree of disorder; in an extreme case all the states may become localized[84]. If the Fermi level lies at the top of the valence band, electrons cannot conduct current well through the solid[85]. It has been suggested that the Anderson mechanism is mainly responsible for metal-insulator transitions in some oxides, such as $La_{1-x}Sr_xCoO_3$ and $La_{1-x}Sr_xVO_3$[86]. In case of $Ho_8Sb_{3-\delta}O_8$ and $Sm_8Sb_{3-\delta}O_8$, disorder of the Sb2-Sb2 dimers as well as deficiencies on the Sb2 sites can lead to the localized states at the top of the valence band. It is worth mentioning that this part of the valence band has significant contributions from the Sb2 orbitals and thus any loss of the periodicity within the Sb2 sublattice should have a significant impact on electron mobility.

3.4 Conclusions

Discovery of the novel RE_3SbO_3 and $RE_8Sb_{3-\delta}O_8$ suboxides was driven by the idea of creating small-band semiconductor through combining semimetallic *RE*Sb and insulating RE_2O_3 binaries. This strategy worked for both families of phases as the band

gap opened between the valence band dominated by the Sb states and the conduction band composed primarily of the Ho states. For RE_3SbO_3, the Fermi level is at the top of the valence band and these phases are regular semiconductors. For $RE_8Sb_{3-\delta}O_8$, the Fermi level lies in the valence band due to an insufficient electron count, nevertheless these phases are semiconducting. The semiconducting behavior of $RE_8Sb_{3-\delta}O_8$ is attributed to the Anderson localization resulting from the random distribution of the Sb-Sb dimers as well as small deficiencies on the Sb site.

Extraordinary thermal stability of the *RE*Sb and RE_2O_3 binaries was treated as an indicator that very high temperatures might be required for the synthesis. Indeed, only temperatures higher than 1350°C allowed to fuse *RE*Sb and RE_2O_3 and to obtain the RE_3SbO_3 and $RE_8Sb_{3-\delta}O_8$ suboxides. We believe that this approach can be applied to the synthesis of other ternary phases from the "stable" binaries.

The compositional and structural similarity of RE_3SbO_3 and $RE_8Sb_{3-\delta}O_8$ appears to control their stability and transformation pathways. In general, the $RE_8Sb_{3-\delta}O_8$ suboxides are more thermodynamically stable and are final products regardless of the starting composition. In practice, tuning the temperature and duration of the heat treatment allows to obtain selectively either the RE_3SbO_3 or $RE_8Sb_{3-\delta}O_8$ phases.

While we were successful in preparing small-band semiconducting suboxides, we failed in having these suboxides reasonably conductive which is a requirement for thermoelectric applications.

Chapter 4. Resolving Composition and Structure of *RE*-Sb-O-C Natural Superlattice Phases (*RE* = La, Ho)

This chapter encompasses the manuscript "Resolving Composition and Structure of *RE*-Sb-O-C Natural Superlattice Phases (*RE* = La, Ho)", published in the European Journal of Inorganic Chemistry (*Eur. J. Inorg. Chem.* **2010**, (26), 3887-3895.). The candidate prepared all the targeted compounds, investigated their structures and designed the parallel preparative experiments for composition analysis. Mr. Scott Forbes was involved in optimization of the synthetic routines. Dr. Volodymyr Svitlyk and Dr. Ashur Aushana carried out some of the earlier explorative synthetic work and the preliminary structural study.

A family of rare-earth antimonide oxycarbides have been prepared and structurally characterized. These superlattice phases are constructed from NaCl-type *RE*Sb slabs sandwiched between *RE*-O-C layers. Depending on the carbon content and synthetic conditions, three different *RE*-Sb-O-C structures can be obtained. At lower temperatures, $RE_{9-\delta}Sb_5(O,C)_5$ phases are obtained for *RE* = La, Ho. These phases adopt a stuffed Sc_2Sb type structure with the *P*4/*nmm* symmetry. A O/C mixture, with the O:C ratio of larger than 4:1, is randomly distributed within the *RE*-O-C layers. Also, the *RE* atoms are highly disordered within the oxide layer. At higher temperatures above the melting point of the samples, $RE_9Sb_5O_4C$ phases with the *P*4/*n* symmetry are produced. The *RE*-O-C layers in $RE_9Sb_5O_4C$ are fully ordered: the *RE* sites are well defined and the oxygen and carbon atoms occupy the tetrahedral and square-pyramidal voids, respectively. Also at high temperatures, a new ordered $La_{14}Sb_8O_7C$ structure with *P*4*bm* symmetry was discovered. The $La_{14}Sb_8O_7C$ phase is structurally similar to $RE_9Sb_5O_4C$ and features ordered arrangements of *RE* and O/C atoms in the La-O-C layer. The $RE_{9-\delta}Sb_5(O,C)_5$, $RE_9Sb_5O_4C$ and $La_{14}Sb_8O_7C$ phases appear to be charge balanced, and their compositions and structures are controlled by the O/C ratio. Parallel preparative experiments revealed the importance of carbon in the formation of these layered phases. In addition, it has been established that the purity of the rare-earth metals influences the compositions and structures of the products.

4.1 Introduction

Recently, a new approach known as a natural superlattice approach[35] has been employed in the design and preparation of new materials for thermoelectric applications. An ideal thermoelectric material has to have a large Seebeck coefficient α and low thermal conductivity κ, while retaining a high electrical conductivity σ.[2] However, these desired physical properties are rarely found simultaneously in a single homogenous material. By constructing a natural superlattice, a material with desired electrical properties is combined with a thermally insulating material in such a way that both of their basic structural building blocks are preserved and interwoven into a single structure.[25] Such structural design has been realized in the $Ca_xYb_{1-x}Zn_2Sb_2$ phases.[36] The structure of the $Ca_xYb_{1-x}Zn_2Sb_2$ system consists of two alternating layers: the cationic Ca^{2+}/Yb^{2+} layer and the anionic $Zn_2Sb_2^{2-}$ layer. Thermoelectric performance is improved as the disordered cationic layer functions as a phonon barrier to reduce the thermal conductivity, while the electrical properties of the anion layer remain unperturbed.

Inspired by the natural superlattice approach, we have undertaken systematic structural and compositional analyses of the partially oxidized rare-earth antimonide oxides $RE_9Sb_5O_5$ (*RE* = La, Ho).[49, 51, 75] Previous works[49, 51, 75] have revealed some interesting structural features of these compounds. As shown in Figure 4.1, their structure can be understood as a variant of the Sc_2Sb structure.[49] The unit cell of Sc_2Sb consists of a layer of Sc atoms sandwiched between slightly puckered NaCl-type ScSb slabs. In the case of the $RE_9Sb_5O_5$ phases, the unit cells consist of the $[RE_4O_5]$ layers and NaCl-type

[RE_5Sb_5] slabs. The oxide layer has 4 *RE* atoms occupying 4 out of 5 metal positions present in the Sc_2Sb structure, and the O atoms fill the interstitial sites. [51]

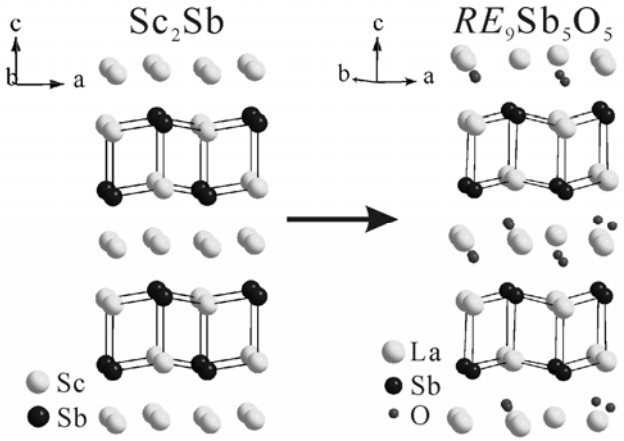

Figure 4.1. Structures of Sc_2Sb and $RE_9Sb_5O_5$

The [RE_5Sb_5] slabs in the $RE_9Sb_5O_5$ system are expected to retain the electrical properties of the *RE*Sb binaries as they share the same structure. The pristine *RE*Sb binaries are semimetallic/metallic materials[39] containing some of the heaviest elements in the periodic table. However, these binary phases, adopting a simple NaCl-type crystal structure, are expected to possess a relatively high thermal conductivity due to the small number of atoms in their unit cells.[41, 42] The [RE_4O_5] layer sandwiched between two [RE_5Sb_5] slabs adopts a completely different structure and is expected to perturb phonon propagation by increasing the structural complexity.

It was also noticed that there are two dissimilar oxygen positions within the RE_4O_5 layer. One of the site (8*g*) is surrounded by 4 neighboring rare-earth elements in a tetrahedral arrangement, while the other one (2*c*) has a rather unusual square-pyramidal environment of 5 *RE* atoms. With oxygen atoms fully occupying the two sites, the electron rich formula, $RE_9Sb_5O_5$ ($RE^{3+}{}_9Sb^{3-}{}_5O^{2-}{}_5(2e^-)$), results. An electron-balanced

formula, $RE_9Sb_5O_4C$ ($RE^{3+}{}_9Sb^{3-}{}_5O^{2-}{}_4C^{4-}$) with carbon instead of oxygen in the 2*c* site, was also suggested.[49] However, the electrical resistivity measurements performed on the bulk samples revealed a metallic type behavior, thus supporting the electron-rich model.

The metallic-type conductivity imply that the $RE_9Sb_5O_5$ phases would possess a low thermopower α, unattractive for industrial applications. Nonetheless, the observed electrical properties may also result from a partial substitution of carbon on the 2*c* site by oxygen (if the 2*c* site is assumed to be primarily occupied by carbon). The refinement results for the $RE_9Sb_5O_5$ single crystals[49] yielded large thermal vibrations for the 2*c* oxygen atoms, suggesting the presence of a lighter element on this site. Existence of pure $RE_9Sb_5O_5$ may be also questionable considering the existence of the semiconducting RE_3SbO_3 and $RE_8Sb_{3-\delta}O_8$ antimonide oxides, where O atoms have a typical tetrahedral *RE* environment (See Chapter 3). The RE_3SbO_3 phases are produced by direct high-temperature fusion of the *RE*Sb and RE_2O_3 binaries, while $RE_8Sb_{3-\delta}O_8$ can be derived from RE_3SbO_3 via loss of *RE* and O.

Considering the above-discussed factors, it is likely that "$RE_9Sb_5O_5$" phases were stabilized by light elements other than oxygen. If carbon can replace oxygen on the 2*c* site in "$RE_9Sb_5O_5$", the electrical properties could be adjusted to render these phases semiconducting and in favor of good thermoelectric performance. This work focuses on the synthesis, compositions and structural characterization of phases related to the $RE_9Sb_5O_5$/$RE_9Sb_5O_4C$ (*RE* = La, Ho) phases, in an effort to uncover the significance of carbon on their structural, chemical and physical properties.

4.2 Experimental

4.2.1 Synthesis

The rare-earth antimonide oxide/oxycarbide samples were prepared from antimony metal (99.999 wt. %, CERAC Inc), La_2O_3 and Ho_2O_3 powders (99.99 wt. %, Rhône-Poulenc) and carbon powder (99.995 wt. %, Alfa Aesar). Rare-earth metals with different level of purities, including the commercial grade *RE* metal (~93 at. %, CERAC Inc) and the *RE* metals purified by Ames Laboratory (99.9 at. %), were used for parallel syntheses and analyses.

The general synthetic schemes involve three steps. As the first step, *RE*Sb binaries were prepared by direct sintering of the elements. Mixtures of the filed rare-earth metals and ground elemental antimony in the 1:1 atomic ratio were pressed into 1 gram pellets in a glove box. The samples were sealed in evacuated silica tubes 10-15cm in length, then heated to 600^{o}C at a rate of 50^{o}C /hour. The sintering temperature was maintained at 600^{o}C to allow the antimony to react with the rare earth metal. After 12 hours, the temperature was raised to 850^{o}C at a rate of 50^{o}C/hour and held for 48 hours to drive the reaction to completion. Black pellets were obtained after cooling in air. The purity of these binaries was confirmed by X-ray powder diffraction analysis.

The second step involved preparing pseudo compounds "RE_4O_5" and "RE_4O_4C" from stoichiometric amount of *RE* metal filings, pre-fired RE_2O_3 powders and carbon powder. The mixtures were pressed into 0.5g pellets under argon atmosphere. Subsequently, the sample pellets were sintered in evacuated silica tubes at 1000^{o}C for 48 hours. Uniform black pellets were obtained after cooling in air. The products were air-

sensitive, therefore they were handled and stored in a glove box. Finally, the precursors were mixed in different ratios according to:

$$5RESb + 1\text{-}x\text{“}RE_4O_5\text{”} + x\text{“}RE_4O_4C\text{”} = RE_9Sb_5O_{5-x}C_x \quad (x = 0, 0.5 \text{ and } 1)$$

Samples of 0.3 gram were pressed into pellets and sealed in tantalum tubes under argon atmosphere. The Ta tubes were placed into a molybdenum susceptor and heated in a high frequency induction furnace under a dynamic vacuum below 10^{-5} torr. The reaction temperature was monitored by an optical pyrometer. All the samples were annealed at the desired temperature for 8 hours, and then were left to cool to room temperature under dynamic vacuum. The products obtained either remained in a pellet form or were solidified from a melt. All the samples appeared to be dark grey in color with a metallic luster. The La samples were sensitive to air and decomposed into a white/grey powder while the Ho samples were stable in air.

Table 4.1. Annealing temperature, carbon content and product appearances of the $RE_9Sb_5O_{5-x}C_x$ samples.

			A	B	C	D	E
	T, °C	General Formula	$x = 0$ Commercial grade *RE* metal	$x = 0$	$x = 0.5$	$x = 1$	$x = 1$ with extra 0.5 mol of Carbon
1	1400	$La_9Sb_5O_{5-x}C_x$	---	---	---	Sintered	---
2	1550	$La_9Sb_5O_{5-x}C_x$	Molten	Molten	Molten	Molten	Molten
3	1650	$Ho_9Sb_5O_{5-x}C_x$	Sintered	Sintered	Sintered	Sintered	Molten
4	1575	$Ho_9Sb_5O_{5-x}C_x$ + 0.3 Ho_5Sb_3	---	---	---	Molten	---

Twelve samples were prepared following the general synthetic procedures. As shown in Table 4.1, these samples can be placed into five groups according to the synthetic conditions and purity of the rare-earth elements. Samples labeled B, C, D and E

(Table 4.1) were prepared from high-purity *RE* metals. Samples A were produced to illustrate the impact of impurities in commercial grade *RE* metals. Lastly, samples E were synthesized with additional carbon to determine the maximum amount of carbon that can be retained in the system.

4.2.2 X-ray single-crystal diffraction and structure refinement

X-ray single crystal diffraction studies were performed on crystals extracted from the crushed samples. Room temperature diffraction data were collected on a STOE IPDSII diffractometer with MoK_α radiation in the whole reciprocal sphere. A numerical absorption correction was based on the crystal shape that was originally derived from the optical face indexing but was later optimized against equivalent reflections using the STOE X-Shape software.[60] The data for the $La_{8.80(1)}Sb_5(O,C)_5$ and $La_{14}Sb_8O_7C$ single crystals were collected on a Bruker SMART Apex II CCD diffractometer (MoK_α radiation) at 100(2) K in a reciprocal hemisphere. Intensities were extracted and then corrected for Lorentz and polarization effects through the SAINT program.[61] Numerical absorption correction was based on the crystal shape obtained from the optical face indexing. Structural determinations and refinements of all the data sets were performed using the SHELXL program. [62]

Crystal structures were determined for five new phases. These new compounds are identified by their refined compositions and space group as the following: $La_{14}Sb_8O_7C$ with *P*4*bm* symmetry, $La_{8.80(1)}Sb_5(O,C)_5$ and $Ho_{8.84(3)}Sb_5(O,C)_5$ with *P*4/*nmm* symmetry, $La_9Sb_5O_4C$ and $Ho_9Sb_5O_4C$ with *P*4/*n* space group. The crystallographic information of

$La_{14}Sb_8O_7C$, $La_{8.80(1)}Sb_5(O,C)_5$, $Ho_{8.84(3)}Sb_5(O,C)_5$, $La_9Sb_5O_4C$ and $Ho_9Sb_5O_4C$ is given in Table 4.2 and 4.3.

Further details of the crystal structure investigations can be obtained from the Fachinformationszentrum Karlsruhe, 76344 Eggenstein-Leopoldshafen, Germany, (fax: (49) 7247-808-666; e-mail: crysdata@fiz.karlsruhe.de) on quoting the depository CSD numbers 422097 for $La_{14}Sb_8O_7C$, 422098 for $La_{8.80(1)}Sb_5(O,C)_5$, 422099 for $La_9Sb_5O_4C$, 422095 for $Ho_{8.84(3)}Sb_5(O,C)_5$, 422096 for $Ho_9Sb_5O_4C$.

Table 4.2. Crystallographic data and refinement results for the $La_{14}Sb_8O_7C$, $La_{8.80}Sb_5(O,C)_5$, $La_9Sb_5O_4C$, $Ho_{8.84}Sb_5(O,C)_5$, and $Ho_9Sb_5O_4C$ single crystals, MoKα radiation

Sample code **[a]**	2B	1D	2D	3C	4D
Refined composition	$La_{14}Sb_8O_7C$	$La_{8.80(1)}Sb_5(O,C)_5$ **[b]**	$La_9Sb_5O_4C$	$Ho_{8.84(3)}Sb_5(O,C)_5$ **[b]**	$Ho_9Sb_5O_4C$
Formula weight	3042.75	1911.16	1934.95	2148.38	2169.13
Temperature, K	100(2)	100(2)	293(2)	100(2)	293(2)
Space group	*P*4*bm*	*P*4/*nmm*	*P*4/*n*	*P*4/*nmm*	*P*4/*n*
Unit cell dimensions, Å	13.0788(1), 9.3886(2)	4.623(1), 9.388(2)	10.414(2), 9.334(2)	4.3628(2), 8.8084(7)	9.782(1), 8.768(1)
Volume /Å^3	1605.97(4)	200.63(5)	1012.2(3)	167.659(7)	838.94(1)
Z	4	0.40**[c]**	2	0.40**[c]**	2
D_{calcd} /g cm^{-3}	6.292	6.327	6.349	8.462	8.587
Abs. coeff., mm^{-1}	24.641	24.878	25.063	48.760	49.763
θ range / degrees	3.09 to 52.22	2.17 to 45.21	3.52 to 34.74	4.63 to 44.94	2.32 to 29.23
Index ranges	-26 ≤ h ≤ 28, -19 ≤ k ≤ 29, -18 ≤ l ≤ 20	-9 ≤ h ≤ 8, -9 ≤ k ≤ 8, -17 ≤ l ≤ 16	-16 ≤ h ≤ 15, -16 ≤ k ≤ 16, -14 ≤ l ≤ 14	-8 ≤ h ≤ 7, -8 ≤ k ≤ 7, -17 ≤ l ≤ 14	-13 ≤ h ≤ 10, -13 ≤ k ≤ 13, -10 ≤ l ≤ 11
Reflections collected	33821	5866	21750	3101	5452
Independent reflections	8703 (R_{int} = 0.1029)	520 (R_{int}=0.0359)	2112 (R_{int}=0.1163)	456 (R_{int}=0.2166)	1142 (R_{int}=0.0859)
Completeness to max. 2θ	98.2 %	95.6 %	96.4 %	99.8 %	99.4 %
Data / restraints / param.	8703 / 1 / 83	520 / 0 / 17	2112 / 0 / 47	456 / 0 / 17	1142 / 0 / 47
Goodness-of-fit on F^2	1.007	1.044	1.083	0.908	0.760
Final R indices [I>2σ(I)]	R1 = 0.0570, wR2 =0.1036	R1 = 0.0184, wR2 = 0.0359	R1 = 0.0531, wR2 = 0.0902	R1 = 0.0481, wR2 = 0.1045	R1 = 0.0263, wR2 = 0.0421
R indices (all data)	R1 = 0.1084, wR2 = 0.1233	R1 = 0.0245, wR2 = 0.0372	R1 = 0.1027, wR2 = 0.1024	R1 = 0.0642, wR2 = 0.1081	R1 = 0.0596, wR2 = 0.0469
Extinction coefficient	0.00007(2)	0.0046(5)	0.00046(6)	0.0040(9)	0.00103(4)
Diffr. peak/hole, e/Å^3	6.200/-5.423	1.239/-1.860	4.056/-3.991	3.452/-6.895	1.946/-2.557

[a] Sample code refer to the synthetic conditions listed in Table 4.1. [b]The composition refined with oxygen atoms occupying all interstitial sites, since the ratio of O and C could not be determined unambiguously. [c] Fraction number used for *Z* to account for the refined compositions.

Table 4.3. Atomic and isotropic temperature (*U*) parameters for the $La_{14}Sb_8O_7C$, $La_{8.80}Sb_5(O,C)_5$, $La_9Sb_5O_4C$, $Ho_{8.84}Sb_5(O,C)_5$, and $Ho_9Sb_5O_4C$ single crystals.

Atom	Site	Occupancy	*x/a*	*y/b*	*z/c*	*U* (Å^2)
			$La_{14}Sb_8O_7C$ 100(2)K			
La(1)	2*a*	1	0	0	0.0188(2)	0.0040(2)
La(2)	2*b*	1	0	1/2	0.0029(1)	0.0047(1)
La(3)	4*c*	1	0.24915(3)	0.25085(3)	0.00983(8)	0.0042(1)
La(4)	4*c*	1	0.10905(3)	0.60905(3)	0.3462(1)	0.00448(8)
La(5)	8*d*	1	0.99027(4)	0.24992(4)	0.69143(5)	0.00427(7)
La(6)	8*d*	1	0.15480(3)	0.88289(3)	0.3529(1)	0.00418(5)
Sb(1)	2*a*	1	0	0	0.6582(1)	0.0044 (2)
Sb(2)	2*b*	1	0	1/2	0.6464(1)	0.0047(2)
Sb(3)	4*c*	1	0.23992(4)	0.26008(4)	0.65386(9)	0.0049(1)
Sb(4)	8*d*	1	0.00157(4)	0.75143(4)	0.04785(7)	0.0041(1)
O(1)	2*b*	1	0	1/2	0.239(1)	0.008(2)
O(2)	4*c*	1	0.2387(5)	0.7387(5)	0.262(1)	0.007(1)
O(3)	8*d*	1	0.2390(4)	0.0271(4)	0.4393(7)	0.0066(8)
C(1)	2*a*	1	0	0	0.278(1)	0.0013(2)
			$La_{8.80(1)}Sb_5(O,C)_5$ 100(2)K			
La(1)	2*c*	1	1/4	1/4	0.3405(1)	0.0075(1)
La(2)	8*i*	0.1897(7)	3/4	0.1810(2)	0.9972(2)	0.0175(2)
Sb(1)	2*c*	1	1/4	1/4	0.6974(1)	0.0074(1)
O(1)[a]	2*c*	1	1/4	1/4	0.0889(7)	0.045(2)
			$Ho_{8.84(3)}Sb_5(O,C)_5$ 100(2)K			
Ho(1)	2*c*	1	1/4	1/4	0.33855(7)	0.0122(2)
Ho(2)	8*i*	0.192(1)	3/4	0.1905(8)	0.999(2)	0.025(1)
Sb(1)	2*c*	1	1/4	1/4	0.6933(1)	0.0122(2)
O(1)**[a]**	2*c*	1	1/4	1/4	0.086(2)	0.051(5)
			$La_9Sb_5O_4C$ 293(2)K			
La(1)	2*c*	1	1/4	1/4	0.6663(2)	0.0071(3)
La(2)	8*g*	1	0.3535(1)	0.9536(1)	0.3460(1)	0.0069(1)
La(3)	8*g*	1	0.1692(1)	0.0219(1)	0.0020(1)	0.0076(1)
Sb(1)	2*c*	1	1/4	1/4	0.3070(3)	0.0108(4)
Sb(2)	8*g*	1	0.3471(1)	0.9472(1)	0.7018(1)	0.0072(1)
O(1)	8*g*	1	0.3722(8)	0.9727(9)	0.092(1)	0.010(2)
C(1)	2*c*	1	1/4	1/4	0.929(3)	0.011(4)
			$Ho_9Sb_5O_4C$ 293(2)K			
Ho(1)	2*c*	1	1/4	1/4	0.6713(2)	0.0104(3)
Ho(2)	8*g*	1	0.3540(1)	0.9547(1)	0.3443(1)	0.0096(1)
Ho(3)	8*g*	1	0.1682(1)	0.0233(1)	0.0022(1)	0.0094(1)
Sb(1)	2*c*	1	1/4	1/4	0.3155(3)	0.0125(4)
Sb(2)	8*g*	1	0.3458 (1)	0.9455(1)	0.6986(1)	0.0094(2)
O(1)	8*g*	1	0.3699(6)	0.9740(8)	0.090(1)	0.011(2)
C(1)	2*c*	1	1/4	1/4	0.931(4)	0.016(6)

[a]Atomic sites that were expected to be occupied by a mixture of O and C.

4.2.3 X-ray powder diffraction

Table 4.4. Lattice parameters and impurity phases in the bulk samples of $La_{9-\delta}Sb_5(O,C)_5$, $Ho_{9-\delta}Sb_5(O,C)_5$, $La_9Sb_5O_4C$ and $Ho_9Sb_5O_4C$.

Sample code	Major Phase (Mol %)	Space Group	Lattice Parameter	Side Product 1 (Mol %)	Side Product 2 (Mol %)	Side Product 3 (Mol %)
1D	$La_{9-\delta}Sb_5(O,C)_5$ 79.4(7)%	*P*4/*nmm*	4.6296(1), 9.3738(3)	La_3SbO_3 11.7(5)%	LaSb 7.9(4)%	La_2O_3 0.4(2)%
2D	$La_9Sb_5O_4C$ 91.2(6)%	*P*4/*n*	10.4147(2), 9.3391(3)	La_4Sb_3 8.8(3)%	--	--
3C	$Ho_{9-\delta}Sb_5(O,C)_5$ ~100%	*P*4/*nmm*	4.3524(1), 8.8092(3)	--	--	--
4D*	$Ho_9Sb_5O_4C$ 85.2(8)%	*P*4/*n*	9.7789(1), 8.7414(3)	Ho_2O_3 9.5(6)%	Ho_5Sb_3 5.2(2)%	--

* Isolated clusters of crystals

The sintered samples were subjected to X-ray powder diffraction analysis. Between 20 and 50 mg of sample were used for each data collection. Diffraction data in the 20–70° 2θ range were collected on a PANalytical X'Pert Pro diffractometer with an X'Celerator detector and Cu$K_{\alpha 1}$ radiation. From the X-ray powder pattern, the desired phase in each sample was identified along with the side products (Figure 4.2). The full-profile Rietveld refinement (Rietica program)[63] was used to refine the lattice constants and amount of side products. The structural models obtained from X-ray single crystal diffraction studies were used for the Rietveld refinement. The $La_{9-\delta}Sb_5(O,C)_5$, $Ho_{9-\delta}Sb_5(O,C)_5$, $La_9Sb_5O_4C$ and $Ho_9Sb_5O_4C$ phases were identified in the bulk samples. The extracted lattice constants, purity and corresponding side products are listed in the Table 4.4 with the sample codes representing the synthetic conditions given in Table 4.1.

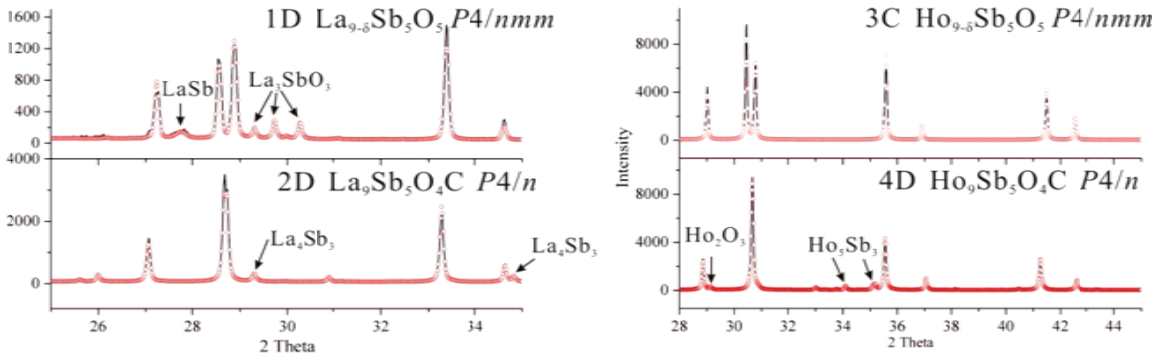

Figure 4.2. Identification of the impurity phases by Rietveld refinement.

4.3 Results and Discussion

The experimental results revealed interesting compositional and structural features as well as relationships between the various phases. Percentage yield (in wt. %) of the desired phase in bulk samples is plotted against the loaded amount of carbon in Figure 4.3. The products are identified by their crystal structures. The different symbols represent the purity of the La and Ho metals and annealing conditions (Table in Figure 4.3). For $x = 0$ (no carbon added), the samples from the commercial and purified La and Ho were prepared. The graph in Figure 4.3 reveals two trends: (1) the yield of the product depends on the carbon content in the starting material; (2) the synthetic conditions determine the structure of the products. However, in order to explain the observed trends, the crystal structure and composition of each phase has to be discussed first.

4.3.1 $RE_9Sb_5O_4C$

According to the X-ray single crystal analysis, the $La_9Sb_5O_4C$ and $Ho_9Sb_5O_4C$ phases adopt the $La_9Sb_5O_5$-type structure with the *P*4/*n* space group. As discussed in the Introduction, in the $La_9Sb_5O_5$ structure oxygen atoms occupy both the tetrahedral (8*g*) and square-pyramidal (2*c*) interstitial sites. The $La_9Sb_5O_5$ model was used to refine the

$La_9Sb_5O_4C$ and $Ho_9Sb_5O_4C$ structures. However, it was observed that the thermal parameters of the oxygen atoms in the 2*c* site were abnormally large in comparison to those of the 8*g* oxygen. A modified model (Figure 4.4) with carbon atoms instead of oxygen ones on the 2*c* site was tried. In the new model, the thermal vibration parameters for the 2*c* site were significantly improved (Table 4.5), while other atomic parameters remained unaffected. As a result, the compositions of the La and Ho phases were assumed to be $La_9Sb_5O_4C$ and $Ho_9Sb_5O_4C$, respectively.

Table 4.5. Thermal parameters of the O/C atoms on the 2c square-pyramidal sites and resulting R1 values in the $RE_9Sb_5O_5$ / $RE_9Sb_5O_4C$ models.

Refined Composition	Atom on 2*c* site	U_{eq}	R_1 value
$La_9Sb_5O_5$	O	0.024(5)	0.0531
$La_9Sb_5O_4C$	C	0.011(4)	0.0531
$Ho_9Sb_5O_5$	O	0.050(8)	0.0264
$Ho_9Sb_5O_4C$	C	0.016(6)	0.0263

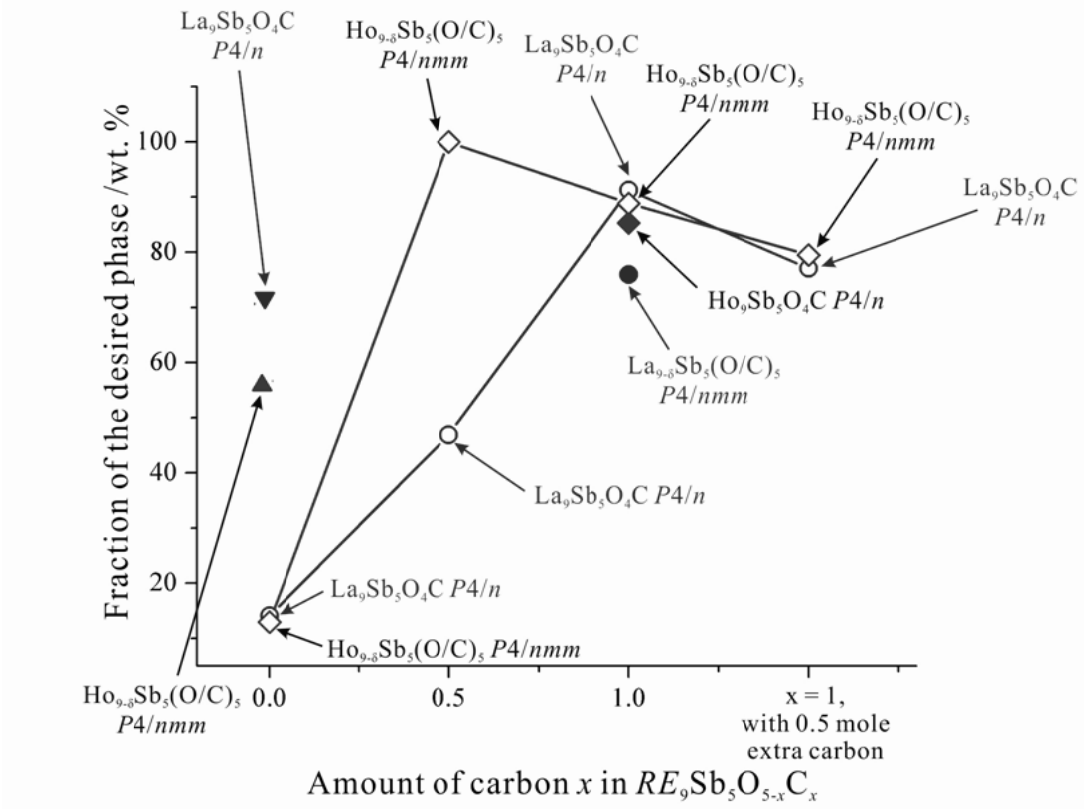

Symbol	Formula	Temperature	Starting Material
—○—	$La_9Sb_5O_{5-x}C_x$	1550°C	with purified La
●	$La_9Sb_5O_{5-x}C_x$	1400°C	with purified La
▼	$La_9Sb_5O_{5-x}C_x$	1550°C	with commercial La
—◇—	$Ho_9Sb_5O_{5-x}C_x$	1650°C	with purified Ho
◆	$Ho_9Sb_5O_{5-x}C_x$	1575°C	with purified Ho and Ho_5Sb_3 flux
▲	$Ho_9Sb_5O_{5-x}C_x$	1650°C	with commercial Ho

Figure 4.3. Yield of the desired phases in each sample is plotted against the amount of added carbon.

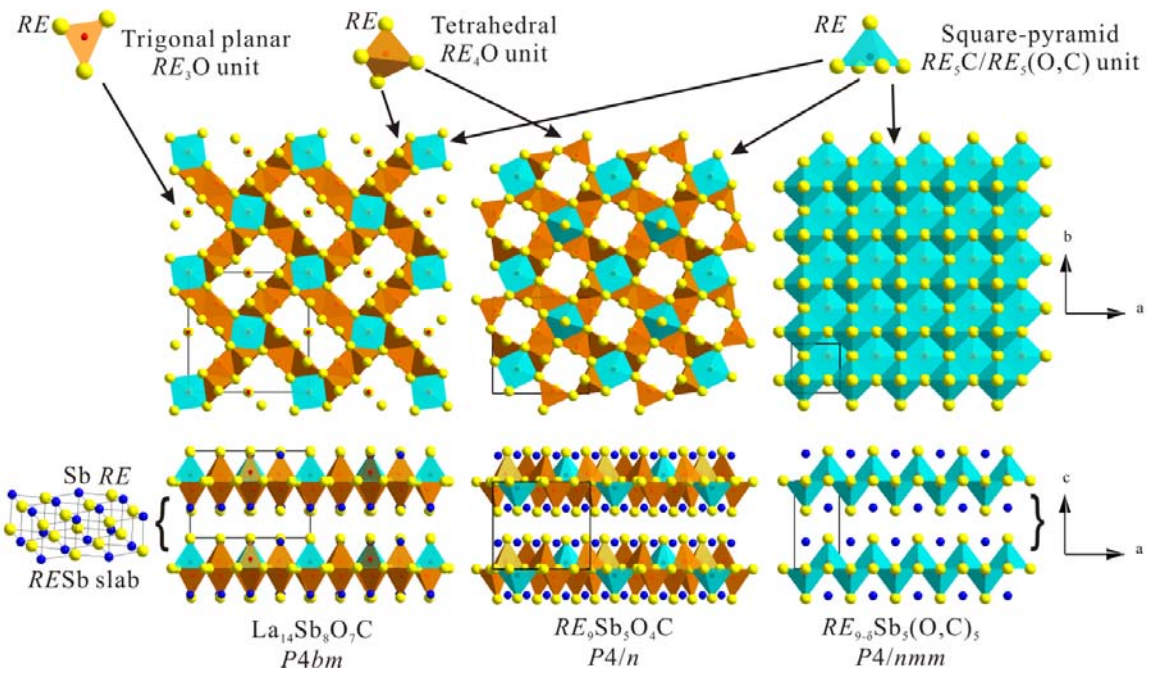

Figure 4.4. Crystal structures of $La_{14}Sb_8O_7C$, $RE_9Sb_5O_4C$, $RE_{9-\delta}Sb_5(O,C)_5$ and their building blocks.

In addition to the refinement results, other factors support carbon rather than oxygen in the square-pyramidal interstitial 2*c* site defined by 5 *RE* atoms. For example, in the rare-earth dicarbides REC_2[87, 88] with the CaC_2 structure, the carbon atoms have 5 *RE* atoms in their first coordination sphere (Figure 4.5, top), similarly to the 2*c* site environment in $RE_9Sb_5O_4C$. It has to be emphasized that in REC_2, the square-pyramidal RE_5C units share square faces, which results in short C-C bonds, but no such C-C bonds are present in $RE_9Sb_5O_4C$. In the RE_2O_3 oxides,[56] oxygen atoms reside inside the *RE* tetrahedra (Figure 4.5, bottom), and this environment is analogous to that of the 8*g* oxygen site in $RE_9Sb_5O_4C$.

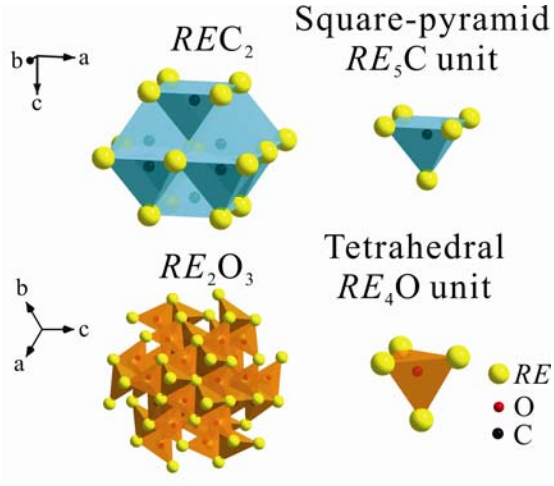

Figure 4.5. The oxygen environments in *RE*C_2 (top) and *RE*$_2O_3$ (bottom).

Also, the bond valence sum method[89] has been employed to test site preferences in the $La_9Sb_5O_4C$ and $Ho_9Sb_5O_4C$. The Ho-C R_0 parameter was derived from the bond distances and coordination geometry of Ho_2C,[90] in which C is assumed to be four valent. Unfortunately, the R_0 parameter for the La-C bond could not be extracted as no comparable compound exists. The R_0 parameters for the La-O and Ho-O bonds were taken from the work by Brese *et al.*[91] The calculated bond valence (B-V) sums for both oxygen and carbon in the 2*c* site are listed in Table 4.6. The results suggest the presence of carbon on the 2*c* site in agreement with the X-ray results.

Table 4.6. Bond Valence sum values for atom in the 2*c* site.

Atom in 2*c* site	R_0 value	Expected B-V sum	Calculated B-V sum
		$La_9Sb_5O_4C$	
O	2.172 Å	2	1.693
C	---	4	---
		$Ho_9Sb_5O_4C$	
O	2.023 Å	2	1.801
C	2.318 Å	4	3.997

4.3.2 $RE_{9-\delta}Sb_5(O,C)_5$.

Similar to the $RE_9Sb_5O_4C$ structure, the $RE_{9-\delta}Sb_5(O,C)_5$ structure also consists of a *RE*-O-C layer sandwiched between the NaCl-type *RE*Sb slabs. Initially, the $RE_{9-\delta}Sb_5(O,C)_5$ crystals were solved in the Sc_2Sb structure, with full *RE* occupancies and O/C atoms filling the interstitial sites between the *RE*Sb slabs. During the refinement, the *RE*(2) metal atoms on the 2*a* position (¾, ¼, 0) in the *RE*-O-C layer exhibited large disk-shaped thermal ellipsoids in the *ab*-plane. Structural refinement of the low-temperature (100K) data of the $La_{9-\delta}Sb_5(O,C)_5$ crystal suggested two alternative models, with the *RE*(2) atoms having either 8*i* or 8*g* position. The new models yielded improved *RE*(2) thermal parameters and lower *R* values both for $La_{9-\delta}Sb_5(O,C)_5$ and $Ho_{9-\delta}Sb_5(O,C)_5$. But the structural model with the *RE*(2) atoms on the 8*i* site yielded either a lower *R* value or more reasonable thermal parameters for both the *RE*(2) and interstitial O/C(1) atoms, therefore it is believed to be the best representation of the overall structure. Comparison of the different models is given in the Table 4.7.

Table 4.7. Atomic positions, occupancy and isotropic thermal vibration parameters of *RE*(2) and O(1) atoms extracted from refinements of 3 structural models with *RE*(2) on different crystallographic sites.

RE(2) site	*RE*(2) position *x/a, y/b, z/c*	*RE*(2) occupancy	U_{eq} / *RE*(2)	U_{eq} / O(1)	R_1
		$La_{8.80(1)}Sb_5(O,C)_5$ (100K)			
2*a*	3/4, 1/4, 0	0.79(2)	0.080(3)	0.035(8)	0.0966
8*g*	0.802(4), 0.197(3), 0	0.189(1)	0.0109(3)	0.056(3)	0.0201
8*i*	3/4, 0.1810(2), 0.9971(2)	0.1897(7)	0.0175(3)	0.045(2)	0.0184
		$Ho_{8.84(3)}Sb_5(O,C)_5$ (100K)			
2*a*	3/4, 1/4, 0	0.80(1)	0.088(2)	0.05(1)	0.0799
8*g*	0.7999(3), 0.2001(3), 0	0.189(1)	0.0143(5)	0.057(5)	0.0479
8*i*	3/4, 0.1903(8), 0.9986(2)	0.192(1)	0.024(1)	0.050(5)	0.0481

The *RE* deficiencies were always present regardless of the model chosen, and thus the general formula for these phases is given as $RE_{9-\delta}Sb_5(O,C)_5$ (the refined compositions were $La_{8.80(1)}Sb_5(O,C)_5$ and $Ho_{8.84(4)}Sb_5(O,C)_5$). During the refinement, the atomic site occupancy of the *RE*(2) atom and the thermal vibration parameters of C/O atoms in the *RE*-O-C layers were correlated, as a result, the *RE* occupation and O/C ratio could not be refined simultaneously. Another interesting outcome is that the O/C ratio in $RE_{9-\delta}Sb_5(O,C)_5$ is larger than in $RE_9Sb_5O_4C$ and likely leads to the *RE* deficiencies, as O is divalent and C is tetravalent. The larger O/C ratio also follows from the synthesis of the $Ho_9Sb_5O_{4.5}C_{0.5}$ sample which yielded the $RE_{9-\delta}Sb_5(O,C)_5$ phase with high purity (Figure 4.3, $x = 0.5$, ◇).

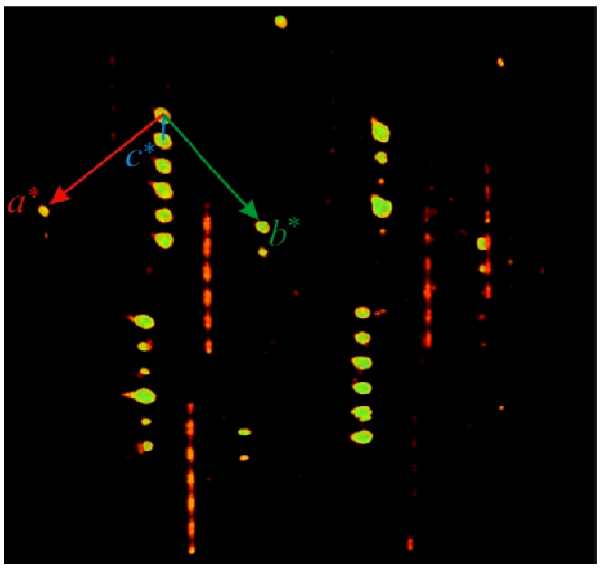

Figure 4.6. Reciprocal lattice of the $La_{8.80}Sb_5(O,C)_5$ crystal, generated from the diffraction data collected at 100K.

Since the *RE*(2) disorder might be indicative of a superstructure, we decided to check for superstructure reflections. Analysis of the reciprocal space of the room-temperature diffraction data both for $La_{8.80(1)}Sb_5(O,C)_5$ and $Ho_{8.84(4)}Sb_5(O,C)_5$ revealed no

signs of a superstructure. But at 100 K, streaks of weak diffused spots were observed along the *c*-direction in the reciprocal space of $La_{8.80(1)}Sb_5(O,C)_5$ (Figure 4.6). Such diffused scattering can imply some degree of ordering on the 8*i* site. From the structural prospective, the *RE*(2) disorder on the 8*i* site allows the *RE* environment around the O/C atoms to change from the square-pyramidal one into the distorted tetrahedral one (Figure 4.7). Such change may be preferred if a particular site is occupied by O. On the other hand, absence of the distortion, i.e. retention of the *RE* square-pyramidal environment, can be associate with the presence of a C atom. It is difficult to establish, what factors causes the *RE*(2) disorder: the absence of the O/C ordering, the O/C ratio, which is incommensurate with the atomic ordering and prevents it, or other parameters.

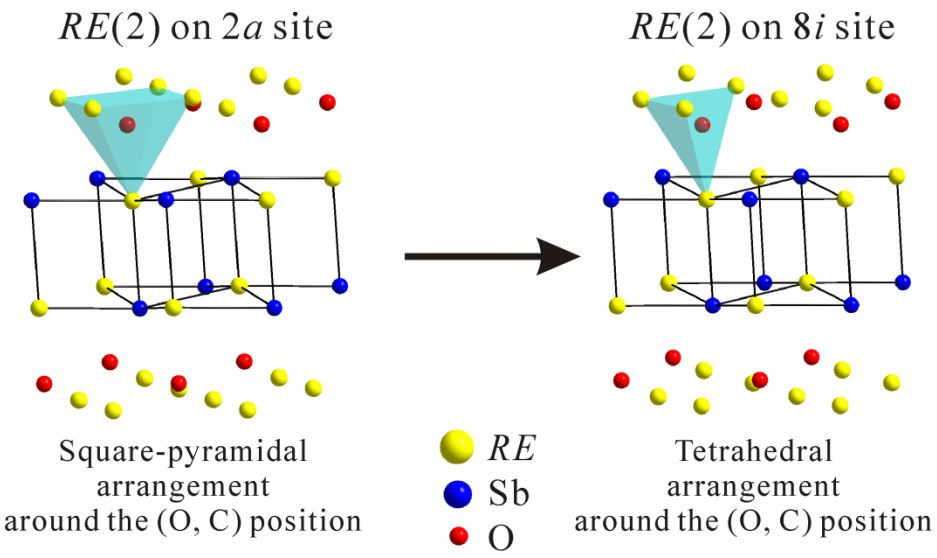

Figure 4.7. Structural models of $RE_{9-\delta}Sb_5(O,C)_5$ with *RE*(2) atoms on the 2*a*, 8*i* sites, respectively. The possible metal environments around the oxygen interstitial sites are identified with the polyhedra.

4.3.3 $La_{14}Sb_8O_7C$

The $La_{14}Sb_8O_7C$ structure also consists of the NaCl-type LaSb slabs and the La-O-C layers, but it possesses a larger unit cell with the *P*4*bm* symmetry. The LaSb slabs of $La_{14}Sb_8O_7C$ are similar to that of $La_9Sb_5O_4C$, but there are four rather than two C/O sites in the La-O-C layer in each unit cell. The O1, O2 sites have tetrahedral environments typical for O atoms in this family of compounds, therefore these sites are assumed to be fully occupied by O atoms. The C site has a square-pyramidal La coordination, which is similar to that observed in $RE_9Sb_5O_4C$. The single crystal structural refinement performed against all collected reflections yielded a smaller temperature factor on the carbon site in comparison to that of the tetrahedral coordinated oxygen atoms. However, the thermal vibration of the carbon became normal when the structural model was refined against high angle reflections ($2\theta > 30^{o}$). While some oxygen atoms can be present, based on the structural analogy to $La_9Sb_5O_4C$, we believe that this site is predominantly occupied by the C atoms. There is also an additional oxygen site (O3), which has only 3 neighboring La atoms in the trigonal-planar arrangement. A similar O environment has been also observed in the $RE_8Sb_{3-\delta}O_8$ structures (Chapter 3).

4.3.4 Structural and compositional relationships

The common building blocks of the $RE_{9-\delta}Sb_5(O,C)_5$, $RE_9Sb_5O_4C$ and $La_{14}Sb_8O_7C$ structures are the NaCl-type *RE*Sb slabs and *RE*-O-C layers. While the NaCl-type *RE*Sb slabs remain identical among the three structures, the *RE*-O-C layers are different. Arrangement and ordering of the *RE* and O/C atoms within these layers appear to dictate the unit cell size as well as its symmetry. The $RE_9Sb_5O_4C$ structure can be viewed as a

parent structure in this series. As discussed in the Introduction, this structure itself is a derivative of the Sc_2Sb structure, in which the *RE* layer, sandwiched between the *RE*Sb slabs, is deficient. Another difference to the Sc_2Sb structure is that the tetrahedral and square-pyramidal voids between the *RE* layer and the *RE*Sb slabs in $RE_9Sb_5O_4C$ are filled with O and C atoms, respectively. More detailed description of the Sc_2Sb - $RE_9Sb_5O_4C$ relationship can be found in the work by Nuss *et al.*[49] One interesting point is that the stoichiometric $RE_9Sb_5O_4C$ phases are charge balanced. This fact may explain the "deficiency" of the *RE* layer, as compared to the Sc_2Sb structure, and the overall phase composition. The NaCl-type $(RE^{+3})_5(Sb^{-3})_5$ slab (composition is per formula unit) is charge balanced, so the $(O^{-2})_4C^{-4}$ composition of the *RE*-O-C layer requires presence of only 4 *RE* atoms to maintain the charge neutrality. This reduces the overall *RE*:Sb ratio from 2:1 expected for the Sc_2Sb-type structures to 1.8:1. The arrangement of the *RE* atoms creates square voids in the *RE*-O-C layers in addition to the tetrahedral and square-pyramidal type voids.

The $RE_{9-\delta}Sb_5(O,C)_5$ phases can be considered as derivatives of the $RE_9Sb_5O_4C$ ones, in which the C content is reduced. Such reduction would lead to a decrease in the *RE* concentration within the *RE*-O-C layer, even if the C loss is offset by the equiatomic O gain. Due to the different coordination requirements of O and C, the ordered atomic arrangement within the *RE*-O-C layer can be achieved only for specific *RE* and O/C stoichiometries. While this condition is met in $RE_9Sb_5O_4C$, apparently it is not satisfied in $RE_{9-\delta}Sb_5(O,C)_5$. As a result, the *RE*-O-C layer of $RE_{9-\delta}Sb_5(O,C)_5$ contains both *RE* disorder and the O/C statistical mixtures. On the local level, both of these features

provide suitable environments for the O and C atoms. While we could not pinpoint the boundaries for the O/C ratio, based on the structural analysis and synthetic results, it appears that ratios 4:1 < O:C ≤ 9:1 are possible for $RE_{9-\delta}Sb_5(O,C)_5$.

The O/C ratio of 7:1 is of particular interest as it yields the $La_{14}Sb_8O_7C$ structure. As expected from the O/C ratio, the La-O-C layer is depleted in La (as compared to $La_9Sb_5O_4C$) to maintain the charge balance. Interestingly, the La-O-C layer with the La_6O_7C composition now finds an atomic arrangement which provides proper environments for both La ordering and the O and C atoms. When compared to $RE_9Sb_5O_4C$, the La layer in $La_{14}Sb_8O_7C$ has larger voids that can be viewed as two square voids from $RE_9Sb_5O_4C$ joint together. Since the $La_{14}Sb_8O_7C$ phase could not be prepared as a bulk, and a similar $Ho_{14}Sb_8O_7C$ could not be verified to exist, it can be assumed that even small deviations from the 7:1 C:O ratio result in the formation of the $RE_{9-\delta}Sb_5(O,C)_5$-type phases

4.3.5 Role of temperature

For the same loading composition, the structure of the resulting phase depends on the annealing temperature. If the temperature is high enough to melt the samples, the resulting structure is $La_{14}Sb_8O_7C$ (*P*4*bm*) or $RE_9Sb_5O_4C$ (*P*4/*n*) with fully ordered *RE*-O-C layers. However, if the temperature is below the sample's melting point, the resulting structure is $RE_{9-\delta}Sb_5(O,C)_5$ (*P*4/*nmm*) with disordered *RE*-O-C layers. This trend can be clearly seen for both the $La_9Sb_5O_4C$ and $Ho_9Sb_5O_4C$ samples prepared from the distilled metals (Figure 4.3). If the $La_9Sb_5O_4C$ sample is annealed at 1400°C, which is below its melting point, the major phase is $La_{9-\delta}Sb_5(O,C)_5$ (*P*4/*nmm*) (76 wt. %, Figure 4.3, ●).

But the same sample heated to 1550°C, above its melting point, contains more than 90 wt. % of the $La_9Sb_5O_4C$ (*P*4/*n*) (Figure 4.3, $x = 1$, ○) phase without any traces of the $La_{9-\delta}Sb_5(O,C)_5$ phase. The $Ho_9Sb_5O_4C$ sample could not be melted at 1650°C which is the highest temperature currently achievable with our experimental setup, and at this temperature the major phase was $Ho_{9-\delta}Sb_5(O,C)_5$ (*P*4/*nmm*) (~88 wt. %, Figure 4.3, $x = 1$, ◇). Melting of the $Ho_9Sb_5O_4C$ sample was achieved by adding a 0.3 molar fraction of Ho_5Sb_3 which acted as a low-temperature flux. After melting the sample, the major phase was $Ho_9Sb_5O_4C$ (*P*4/*n*, 85 wt. %, Figure 4.3,◆). These experiments suggest that there is a large energy barrier for the atomic ordering within the *RE*-O-C layers and a full ordering is achieved only from the liquid state.

4.3.6 Impact of carbon and purity of RE elements

One can argue that the evidence from the structural refinement may not be sufficient to fully support the $RE_9Sb_5O_4C$ composition. In addition, the X-ray diffraction studies on the $RE_{9-\delta}Sb_5(O,C)_5$ single crystals could not prove the presence of carbon. A series of preparative experiments was carried out to reveal the role of carbon and purity of the *RE* elements on the formation of the $RE_9Sb_5O_4C$ and $RE_{9-\delta}Sb_5(O,C)_5$ phases.

Commercial grade late rare-earth metals (Gd-Lu) usually contain light-atom impurities including oxygen (~1 at.%), nitrogen (~0.5 at.%), hydrogen (~3 at.%) and carbon (~1 at.%). [92, 93] While no comparable literature data could be found for the light lanthanides, it is possible that the level of impurities is somewhat higher due to their stronger affinity to the light *p*-elements. Samples with a loading composition of $La_9Sb_5O_5$ (no added carbon) were prepared from both commercial grade (~93 at %) and purified La

metals (Ames Laboratory, 99.9 at. %). According to the X-ray powder analysis, $La_9Sb_5O_4C$ was the major phase (~75 wt.%, Figure 4.3, ▼) in the sample made from the commercial La metal, while its amount in the sample with purified La metal was less than 14 wt. % (Figure 4.3, x = 0, ○). Similar results were obtained for the $Ho_9Sb_5O_5$ samples: the commercial Ho yielded 58 % (Figure 4.3, ▲), while the purified Ho metal gave only 13 % of $Ho_{9-\delta}Sb_5(O,C)_5$ (Figure 4.3, x = 0, ◇). We do not know how much carbon is present in the commercial lanthanum and whether its amount is sufficient to yield 75 wt.% of $La_9Sb_5O_4C$. If the amount of C is insufficient then potentially other impurities, although very unlikely, may stabilize these phases. Hydrogen is unlikely to be a factor, as the high temperatures and dynamic vacuum make Ta tubing transparent to hydrogen, thus allowing hydrogen to escape from the sample.[94] We believe that unintended carbon contamination during handling and preparation may be a factor.

The proof that carbon and not other light elements stabilizes the targeted phases comes from the series of experiments involving the purified La and Ho and controlled amounts of C in $RE_9Sb_5O_{5-x}C_x$ (Figure 4.3). The largest yield for the $RE_9Sb_5O_4C$ phases ($P4/n$) was achieved for the loading compositions with x = 1. Another important conclusion regards the composition of the $RE_{9-\delta}Sb_5(O,C)_5$ phases. The sintered $Ho_9Sb_5O_{4.5}C_{0.5}$ sample contained the $Ho_{9-\delta}Sb_5(O,C)_5$ phase with a high yield (99 wt. %), which suggests that the O:C ratio in some $RE_{9-\delta}Sb_5(O,C)_5$ phases may be close to 4.5:0.5 (or 9:1). As discussed before, the O:C ratio is likely to be variable (4:1 < O/C ratio ≤ 9:1). However, the amount of C retained in this series of phases is unlikely to exceed 1, since the samples with x >1 were less pure, as shown in Figure 4.3.

4.3.7 Formation of the side products

It was noticed that the side products in the carbon-deficient samples are different from the ones observed in the carbon-rich samples. In the carbon poor samples, the major side products were *RE*Sb, RE_2O_3 and RE_3SbO_3, which is the result of direct combination of *RE*Sb and RE_2O_3 (See Chapter 3). In addition to the corresponding RE_2O_3 oxides, *RE* rich *RE*-Sb binaries such as La_4Sb_3 and Ho_5Sb_3 were also found in the samples with excess carbon. It is postulated that, while carbon was essential in the formation of the *RE*Sb/*RE*-O-C superlattice, excess carbon underwent reactions with RE_2O_3 following a mechanism similar to that of the metal oxide reduction process. The rare-earth metals released from the oxides reacted with *RE*Sb to form the corresponding metal-rich binaries. This postulation is supported by all the experimental observations expect that from the preparation of $La_{9-\delta}Sb_5(O,C)_5$ (1D), since no corresponding metal rich binaries were detected by X-ray powder diffraction. Nonetheless, the LaSb impurity in the $La_{9-\delta}Sb_5(O,C)_5$ sample was found to possess a contracted unit cell, where the lattice parameter a = 6. 427(2)Å is smaller than the literature value of a = 6.490Å.[38] The unit cell contraction suggested carbon substitution in the structure. The annealing temperature selected to prepared the $La_{9-\delta}Sb_5(O,C)_5$ sample (1D) might favor the formation of carbon substituted LaSb over the formation of La_4Sb_3.

4.4 Conclusions

In the process of resolving the compositions of the $RE_9Sb_5O_4C$ phases, the novel phases $RE_{9-\delta}Sb_5(O,C)_5$ and $La_{14}Sb_8O_7C$ (*RE* = La, Ho) were discovered. All of them

belong to a family of natural superlattice phases based on intergrowth of the NaCl-type *RE*Sb slabs and the *RE*-O-C layers. The pivotal role of carbon in the formation of these phases has been clearly demonstrated. It has been also shown that the purity of rare-earth elements dictates the outcome of the synthesis.

While the O:C ratio and the positions of the O and C atoms could be unambiguously established in the $RE_9Sb_5O_4C$ phases from the X-ray single and bond valence analysis, the exact O:C ratio could not be reliably refined for the other two phases. Still, it appears that all phases tend to be charge balanced and the O:C ratio dictates both the *RE* content and the atomic arrangement within the *RE*-O-C layers. The most C-rich phases are $RE_9Sb_5O_4C$, and further C incorporation was unsuccessful. Lowering the C content results in the $RE_{9-\delta}Sb_5(O,C)_5$ phases with the O:C ratio larger than 4:1, and then in $La_{14}Sb_8O_7C$ with the O:C ratio of 7:1.

The layered nature of these phases suggests that other structures may be formed, e.g. with *RE*Bi slabs instead of *RE*Sb ones or thicker *RE*Sb slabs. Current research efforts are conducted to test these ideas.

Chapter 5. Decoupling the Electrical Conductivity and Seebeck Coefficient in the RE_2SbO_2 Compounds through Local Structural Perturbations

This chapter encompasses the manuscript "Decoupling the Electrical Conductivity and Seebeck Coefficient in the RE_2SbO_2 Compounds through Local Structural Perturbations", published in the Journal of the American Chemical Society (*J. Am. Chem. Soc.* **2012,** 134 (3), 1426-9). The candidate carried out the synthetic experiments with the assistance of Dr. Jinlei Yao. The structure determinations, electronic structure calculations and data interpretations were also performed by the candidate. Dr. Taras Kolodiazhnyi conducted the physical property measurements of the bulk samples.

Compromise between the electrical conductivity and Seebeck coefficient limits the efficiency of chemical doping in the thermoelectric research. An alternative strategy, involving the control of a local crystal structure, is demonstrated to improve the thermoelectric performance in the RE_2SbO_2 system. The RE_2SbO_2 phases, adopting a disordered *anti*-$ThCr_2Si_2$ type structure ($I4/mmm$), were prepared for *RE* = La, Nd, Sm, Gd, Ho and Er. By traversing the rare-earth series, the lattice parameters of the RE_2SbO_2 phases are gradually reduced, thus increasing chemical pressure on the Sb environment. As the Sb displacements are perturbed, different charge carrier activation mechanisms dominate the transport properties of these compounds. As a result, the electrical conductivity and Seebeck coefficient are improved simultaneously while the number of charge carriers in the series remains constant.

5.1 Introduction

The efficiency of a thermoelectric material can be denoted by the dimensionless figure-of-merit, ZT:

$$ZT = \frac{\alpha^2 \sigma}{\kappa} T \tag{1-5}$$

A high-efficiency thermoelectric material should possess a large Seebeck coefficient (α), high electrical conductivity (σ) while exhibiting low thermal conductivity (κ).[1] Chemically increasing the carrier concentration in a degenerate semiconductor generally improves its electrical conductivity since the electrical conductivity, σ, is directly proportional to the carrier concentration, n, through equation (1-7)[25]

$$\sigma = ne\mu \tag{1-7}$$

However, the Seebeck coefficient (α) is typically compromised in the process as it is inversely related to the carrier concentration,[25] as shown:

$$\alpha = \left(\frac{8\pi^2 {k_B}^2}{3eh^2}\right) m^* T \left(\frac{\pi}{3n}\right)^{2/3} \tag{1-9}$$

These relationships represent limitations of chemical doping for optimizing the power factor, $\alpha^2\sigma$. Many research attempts have been undertaken to achieve a higher power factor by increasing one of the two parameters while keeping the other one constant.[4] However, similar results are rarely realized in homogeneous bulk materials through chemical manipulation. In this work, we explore the possibility of improving the power factor in a system by chemically altering the charge carrier transport mechanism rather than by optimizing the carrier concentration.

The recent work on the rare-earth bismuthide oxides, RE_2BiO_2, can be considered as an excellent example of the chemical perturbation of transport properties without modifying the number of charge carriers.[52] The RE_2BiO_2 phases undergo a Mott-type insulator-to-metal transition as larger early rare-earth atoms are replaced by smaller late rare-earth elements. Such behavior was rationalized in terms of increasing chemical pressure on the square Bi lattice: the Bi–Bi distances decrease as the size of the *RE* atoms becomes smaller and, as a result, the metallic character of the Bi electronic band becomes dominant due to a better Bi–Bi orbital overlap.

5.2 Experimental

5.2.1 Preparation of the RE_2SbO_2 samples

Inspired by this study, we have focused our attention on the antimony analogs, RE_2SbO_2 (*RE* = rare-eath elements). The high-purity RE_2SbO_2 samples were prepared for *RE* = La, Nd, Sm, Gd, Ho and Er. Firstly, the corresponding *RE*Sb precursors were prepared from elemental rare-earth metals (99.9 wt.%) and antimony (99.999 wt.%) following the synthetic route discussed in Section 2.1. The *RE*Sb binaries, powdered Sb metal and corresponding RE_2O_3 powder (99.99 wt. %, pre-fired at 1273K for 12hrs) were mixed in the stoichiometric ratios and pressed into 0.5g pellets in an Ar-filled glove box. Subsequently, the cold-pressed pellets were sealed in Ta tubes and sintered in a high-frequency induction furnace. After sintering at 1773K for 16 hours, black pellets were obtained.

5.2.2 Structure Determination and Phase Analysis

The samples were subjected to X-ray powder diffraction analysis on a PANalytical X'Pert Pro diffractometer with an X'Celerator detector and $CuK_{\alpha 1}$ radiation. Diffraction data were collected in the 20–70° 2θ range. A full-profile Rietveld refinement (Rietica program[63]) was used to refine the lattice constants and assess the purity of the bulk products. The powder X-ray diffraction pattern of the Ho_2SbO_2 sample is shown below.

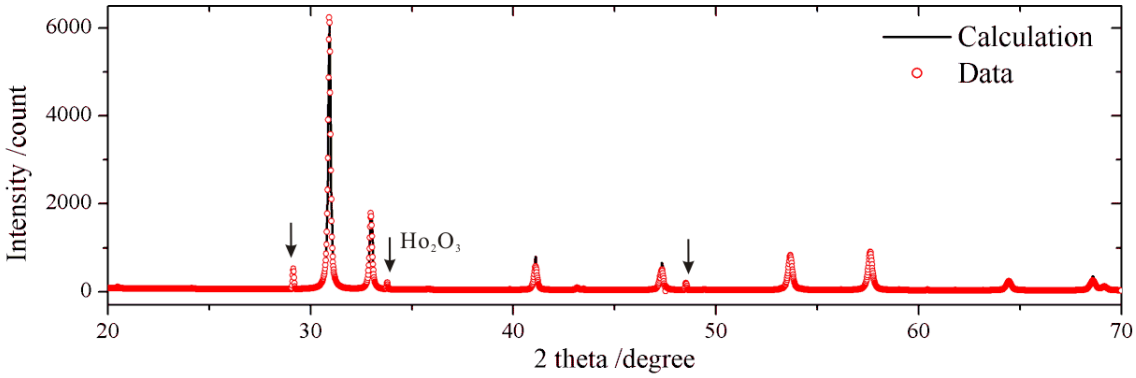

Figure 5.1. The X-ray powder diffraction patterns of the Ho_2SbO_2 sample. The arrows mark the Ho_2O_3 impurity peaks.

X-ray single crystal diffraction studies were performed on crystals extracted from the crushed samples. Room temperature diffraction data were collected on a STOE IPDSII diffractometer with MoK_{α} radiation in the whole reciprocal sphere. A numerical absorption correction was based on the crystal shape that was originally derived from the optical face indexing but was later optimized against equivalent reflections using the STOE X-Shape software. Structural determinations and refinements of all the data sets were performed using the SHELXL program.[62] The crystallographic and refinement results are given in Tables 5.1, 5.2, 5.3 and 5.4.

Table 5.1. Crystallographic data and refinement results for the RE_2SbO_2 single crystals, MoKα radiation.

Sample composition	La_2SbO_2	Nd_2SbO_2	Sm_2SbO_2	Gd_2SbO_2	Ho_2SbO_2	Er_2SbO_2
Formula weight	431.57	442.23	454.45	468.25	483.61	488.27
Temperature, K	293(2)					
Space group	*I*4/*mmm*					
Unit cell dimensions, Å	4.0674(6) 13.705(3)	3.9648(6), 13.555(3)	3.9220(6), 13.323(2)	3.8900(6), 13.277(3)	3.8279(5), 13.039(3)	3.8151(5), 13.007(3)
Volume /Å^3	226.73(7)	213.08(6)	204.94(6)	200.90(6)	191.06(5)	189.32(5)
Z	2					
D_{calc} /g cm^{-3}	6.321	6.893	7.365	7.741	8.406	8.565
Abs. coeff., mm^{-1}	24.244	30.115	34.630	39.108	47.822	50.797
θ range / degrees	2.97 to 28.94	5.36 to 34.48	3.06 to 34.29	5.46 to 34.26	5.55 to 34.44	3.13 to 34.20
Reflections collected	2126	1054	1561	1408	1005	900
Independent reflections	118 (R_{int} = 0.0479)	161 (R_{int}=0.1250)	161 (R_{int}=0.0865)	158 (R_{int}=0.0654)	151 (R_{int}=0.0441)	150 (R_{int}=0.0595)
Completeness to max. 2θ	100 %	95.3 %	100 %	99.4 %	98.7 %	100 %
Data / restraints	118 / 11	161 / 11	161 / 11	158 / 17	151 / 11	150 / 11
Goodness-of-fit on F^2	1.410	1.001	1.063	1.215	1.047	0.610
Final R indices [I>2σ(I)]	R1 = 0.0259, wR2 =0.0488	R1 = 0.0428, wR2 = 0.0742	R1 = 0.0.324, wR2 = 0.0500	R1 = 0.0352, wR2 = 0.0659	R1 = 0.0209, wR2 = 0.0408	R1 = 0.0307, wR2 = 0.1145
R indices (all data)	R1 = 0.0313 wR2 = 0.0500	R1 = 0.0744, wR2 = 0.0819	R1 = 0.0483, wR2 = 0.0532	R1 = 0.0423, wR2 = 0.0674	R1 = 0.0256, wR2 = 0.0418	R1 = 0.0426, wR2 = 0.1293
Extinction coefficient	0.0052(9)	0.007(1)	0.0032(7)	0.0040(9)	0.0075(8)	0.007(3)
Diffr. peak/hole, e/Å^3	1.044/-1.383	2.305/-3.504	3.515/-3.120	1.957/-2.119	1.868/-1.775	2.918/-1.764

Table 5.2. Atomic parameters for the RE_2SbO_2 single crystals.

Atom	Site	Occupancy	x/a	y/b	z/c	*U*eq
RE	4e	1	0	0	z*	U_{eq}(*RE*)*
O	4d	1	0	1/2	1/4	U_{eq}(O)*
Sb	8i	1/4	x*	0	0	U_{eq}(Sb)*

* Values are shown in Table 5.3

Table 5.3. z-coordinates of the *RE* atoms, x-coordinates of the Sb atoms and isotropic temperature parameters of all atoms in the RE_2SbO_2 crystal structures.

	La_2SbO_2	Nd_2SbO_2	Sm_2SbO_2	Gd_2SbO_2	Ho_2SbO_2	Er_2SbO_2
z (*RE*)	0.33934(9)	0.3373(2)	0.3378(1)	0.3272(2)	0.3271(1)	0.3294(2)
x (Sb)	0.073(2)	0.089(2)	0.0861(8)	0.0844(8)	0.075(3)	0.075(7)
U_{eq}(*RE*)	0.0186(4)	0.0175(5)	0.0138(2)	0.0117(2)	0.0119(2)	0.0121(6)
U_{eq}(O)	0.021(2)	0.020(3)	0.015(1)	0.014(2)	0.016(2)	0.021(4)
U_{eq}(Sb)	0.049(3)	0.029(1)	0.024(6)	0.023(1)	0.023(1)	0.024(2)

Table 5.4. Anisotropic displacement parameters ($Å^2×10^3$) for the RE_2SbO_2 single crystals.

Atoms	U^{11}	U^{22}	U^{33}	U^{23}	U^{13}	U^{12}
			La_2SbO_2			
La	0.014(1)	0.014(1)	0.028(1)	0	0	0
O	0.015(3)	0.015(3)	0.031(6)	0	0	0
Sb	0.078(4)	0.078(4)	0.023(1)	0	0	0
			Nd_2SbO_2			
Nd	0.012(1)	0.012(1)	0.028(1)	0	0	0
O	0.011(3)	0.011(3)	0.04(1)	0	0	0
Sb	0.029(3)	0.034(3)	0.025(3)	0	0	0
			Sm_2SbO_2			
Sm	0.008(1)	0.008(1)	0.017(1)	0	0	0
O	0.009(3)	0.009(3)	0.015(4)	0	0	0
Sb	0.024(2)	0.026(2)	0.009(1)	0	0	0
			Gd_2SbO_2			
Gd	0.009(1)	0.009(1)	0.017(1)	0	0	0
O	0.012(2)	0.012(2)	0.017(5)	0	0	0
Sb	0.026(2)	0.029(2)	0.016(1)	0	0	0
			Ho_2SbO_2			
Ho	0.009(1)	0.009(1)	0.015(1)	0	0	0
O	0.012(2)	0.012(2)	0.014(3)	0	0	0
Sb	0.024(2)	0.029(2)	0.011(1)	0	0	0
			Er_2SbO_2			
Er	0.010(1)	0.010(1)	0.017(1)	0	0	0
O	0.014(5)	0.014(5)	0.04(1)	0	0	0
Sb	0.021(3)	0.030(4)	0.021(2)	0	0	0

5.2.3 Physical Property Measurement

The electrical resistivity, Seebeck voltage and thermal conductivity of the prepared RE_2SbO_2 samples were measured in the 2–400 K region on a QD PPMS instrument. Gold

wires of 50 μm diameter were attached to the samples using silver ink. The thermal conductivity was measured using the two-probe configuration of the Thermal Transport Option (TTO) of the QD PPMS. The data were collected in the continuous measurement mode at a cooling rate of 0.2 K/min. The power and period of the heating pulses were automatically adjusted to create a thermal gradient across the sample of 3 % of the ambient temperature. The thermal conductivity was obtained by fitting the time-temperature dependences of the hot and cold thermometers by the TTO software assuming that the infrared emissivity of the polycrystalline samples is close to 1. Thermally evaporated Al contacts have been used as contact pads for four-probe electrical resistivity measurements. Spring-loaded rhodium-plated Be-Cu pin contacts have been utilized to ensure excellent mechanical and electrical contact with the sample during electrical resistivity measurements. Hall measurements were also conducted on the Sm_2SbO_2 and Ho_2SbO_2 samples at 200K and 300K with a magnetic field of 8 Tesla. The charge carrier concentrations of the two phases are comparable (Table 5.5).

Table 5.5. The charge carrier densities of the Sm_2SbO_2 and Ho_2SbO_2 samples obtained from the Hall measurements (8 Tesla) are shown along with their electrical conductivities and Seebeck coefficients at the corresponding temperatures. The calculated charge carrier motilities are also listed.

Sample	Charge Carrier Density ρ /cm^{-3}	Elec. Conductivity σ /S·m^{-1}	Seebeck Coefficient S /μV/K	Charge Carrier Mobility μ /cm^2/(V·s)
		300K		
Sm_2SbO_2	4.77×10^{19}	207	113	0.271
Ho_2SbO_2	3.47×10^{19}	261	215	0.441
		200K		
Sm_2SbO_2	1.22×10^{19}	75.9	98.5	0.390
Ho_2SbO_2	1.22×10^{19}	26.8	152	0.136

5.2.4 Electronic Structure Calculation

In order to understand how the observed Sb atomic arrangement affects the physical properties of the RE_2SbO_2 compounds, the tight-binding, linear-muffin-tin-orbital calculations using the atomic sphere approximation (TB-LMTO-ASA)[65] were performed for Nd_2SbO_2. The ideal anti-$ThCr_2Si_2$ type structure (the *I*4/*mmm* space group and the Sb atoms on the 2*a* site) and a super structure (the *Pmmn* space group) were used for the calculations. The Sb atomic displacements in the disordered structure are described in the super structure by removing the 4-fold degeneracy of the atomic Sb site. The super structure is derived from the original structure by doubling the *a* parameter. The cell orientation has been transformed to fit the standard setting of the *Pmmn* space group. The unit cell parameters of the superstructure are shown in Table 5.6, and the atomic parameters are listed in Table 5.7.

Table 5.6. Unit cell parameters of the superstructure (top) and the transformation matrix for the standard orientation of the supercell (bottom).

Space group	Cell parameters		
	a	*b*	*c*
Pmmn	3.9648	13.555	7.9296

0	1	0
0	0	1
1	0	0

Table 5.7. Atomic parameters for the Nd_2SbO_2 superstructure.

Atom	Site	x/*a*	y/*b*	z/*c*
Nd1	4*e*	1/4	0.5866	1/8
Nd2	4*e*	1/4	0.5866	5/8
O1	4*e*	1/4	1/2	3/8
O2	4*e*	1/4	1/2	7/8
Sb1	2*a*	1/4	1/4	0.1682
Sb2	2*a*	1/4	1/4	0.5818

Exchange and correlation were treated by the local density approximation (LDA).[65] All relativistic effects except spin-orbit coupling were taken into account by using a scalar relativistic approximation.[68] In the ASA method, space is filled with overlapping Wigner-Seitz (WS) atomic spheres, the radii of which were obtained by requiring the overlapping potential to be the best possible approximation to the full potential. To satisfy the overlap criteria of the atomic spheres in the TB-LMTO-ASA method, empty spheres were included in the unit cell employing an automatic sphere generation.[69] The *f*-electrons of the rare-earth elements were treated as core electrons.

The Nd_2SbO_2 unit cell was chosen for the calculation as it possessed the largest Sb *x*-coordinate shift. Both electronic band structures failed to describe the observed semiconductor-type electrical conductivity and suggested a metallic-type behavior. Resembling the La_2BiO_2 band structure,[52] the Fermi level sits at the top of the valence band which is dominated by the Sb states, implying a metallic conductivity.

5.3 Results and Discussion

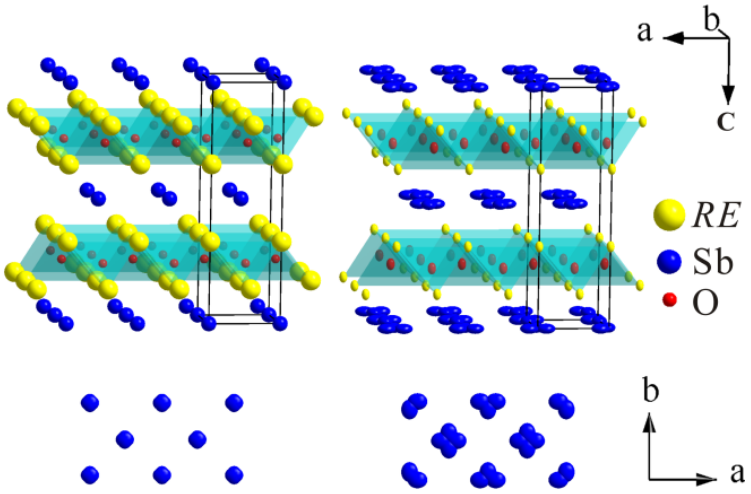

Figure 5.2. The RE_2SbO_2 structural models with the Sb atom on the 2*a* (left) and 8*i* (right) position.

The RE_2SbO_2 compound with Ce was first reported to adopt the *anti*-$ThCr_2Si_2$ type structure with the *I*4/*mmm* space group.[53] As shown in Figure 5.1, left, the structure consists of alternating RE_2O_2 layers and Sb layers, and each antimony atom on the 2*a* atomic site is surrounded by 8 *RE* atoms. However, a recent study by Nuss and Jansen[54] proposed a modified structural model, in which the Sb atoms were shifted away from the ideal 2*a* position along the *a* direction into the 8*i* position with an occupancy of ¼ (Figure 5.1, right). Within the *ab* plane, such atomic arrangements create shorter distances between the Sb atoms on the 4-fold degenerate position. In the case of Ce_2SbO_2 and Pr_2SbO_2 the shortest Sb–Sb distances are 3.23 Å. These Sb–Sb distances were viewed as evidence for Zintl-type Sb^{2-}–Sb^{2-} interactions.[95] Since the rare-earth atoms were found in the 3+ oxidation state from the magnetic susceptibility measurements, and the bulk materials displayed a semiconductor type behavior,[54] the Zintl-type Sb^{2-}–Sb^{2-} dimers

conveniently fit into the charge balanced formula, $RE^{3+}{}_2Sb^{2-}O^{2-}{}_2$. The X-ray single crystal structural results obtained by us for other analogs of the RE_2SbO_2 series (*RE* = La, Nd, Sm, Gd, Ho and Er) agree with the structural model proposed by Nuss and Jansen. As expected, the unit cell parameters decrease with the size of the *RE* elements (Figure 5.2), however the Sb–Sb atomic distances do not follow this trend. As shown in Figure 5.3, the Sb atoms in the large La_2SbO_2 unit cell do not shift along the *x*-direction enough to sustain effective Sb–Sb interactions. Instead, the Sb atoms in the La_2SbO_2 structure appear to be the most localized in the series. As a result, the closest Sb–Sb distance in the La_2SbO_2 structure is 3.471(6) Å. Throughout the rest of the series (Figure 5.3, blue), the Sb–Sb distances remain between 3.22Å and 3.26Å, as the reduction in the unit cell size is offset by smaller Sb *x*-coordinate shifts (Figure 5.3, red).

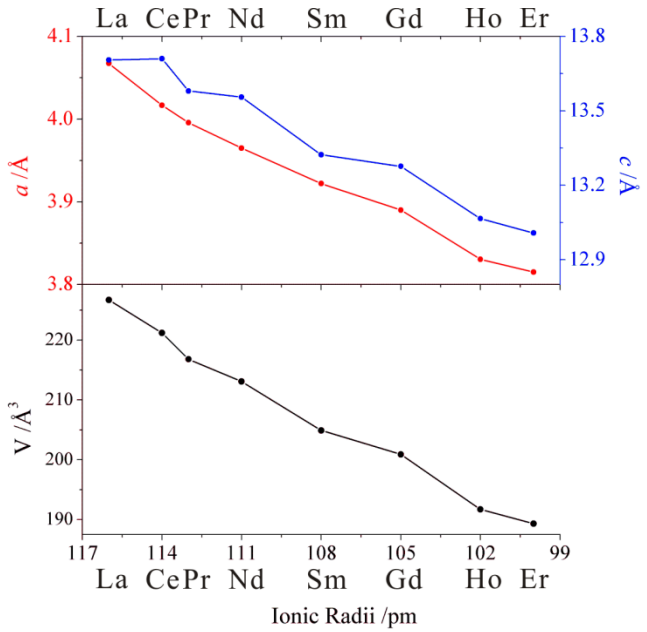

Figure 5.3. Unit cell parameters and volumes of the RE_2SbO_2 compounds extracted from the X-ray single crystal analyses versus the rare-earth ionic radii.[96] The data for $Ce_2SbO_2$and Pr_2SbO_2 are taken from the report by Nuss and Jansen.[54]

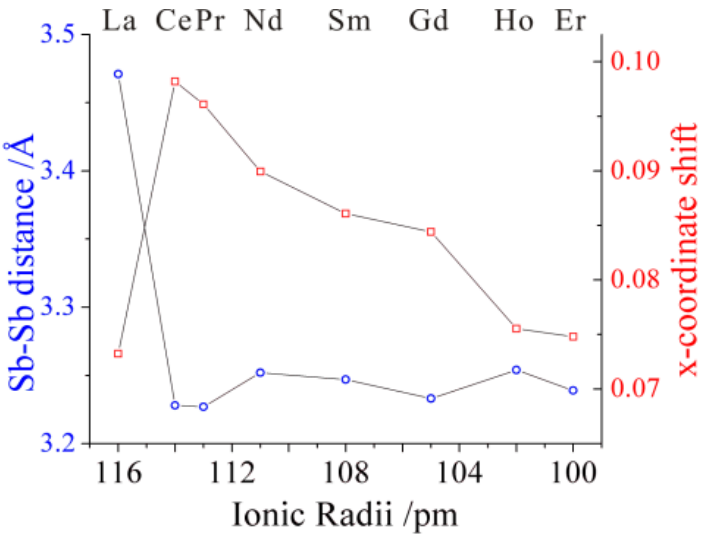

Figure 5.4. Shortest Sb–Sb distance (blue) and Sb *x*-coordinate shift (red) observed in the RE_2SbO_2 crystals with respect to the *RE* ionic radius

As shown in Figure 5.5a, all the RE_2SbO_2 phases display a semiconductor-type behavior. La_2SbO_2 has the highest electrical resistivity, although the least effective Sb–Sb orbital overlap would imply metallic-type conductivities according to the electron poor formula, $RE^{3+}{}_2Sb^{3-}O^{2-}{}_2$. The rest of the phases display semiconducting behaviors with different temperature dependence although their Sb–Sb distances are very similar. However, as in Figure 5.4, the electronic structure calculations based on either the standard structure (*I*4/*mmm*) or the super structure (*Pmmn*) failed to predict the experimentally observed semiconducting properties. Such results are comparable to the band structure of La_2BiO_2 reported by Hosono *et al.*,[52] where the Fermi level penetrates the top of the valence band, thus implying metallic properties.

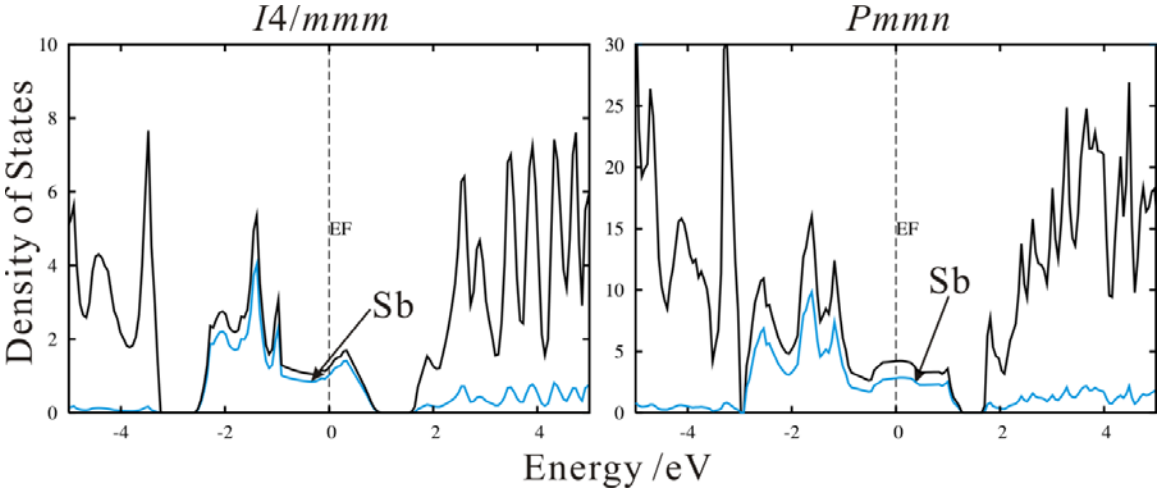

Figure 5.5. Densities of States (DOS) of Nd_2SbO_2 obtained from the LMTO calculations. The blue curves indicate the contribution of the Sb states. (Left) The DOS of the ideal anti-$ThCr_2Si_2$ type (*I*4/*mmm*) structure with the Sb atoms on the 2*a* site. (Right) The DOS of the super structure with the *Pmmn* space group.

The calculation also suggested that the Sb states in RE_2SbO_2 have the largest contribution at the vicinity of the Fermi level. Therefore, the local atomic arrangement within the Sb layer will dictate the electrical properties of these phases. There are two interrelated structural parameters in the Sb layer: the Sb–Sb distances and the Sb site disorder, both of which are governed by the unit cell dimensions. However, for the first member of the family, La_2SbO_2, these parameters are different than for the rest of the group. The electronic structure of La_2SbO_2 conceivably resembles that of La_2BiO_2 more closely than the rest of the RE_2SbO_2 series, as the Sb site disorder is minor and the Sb–Sb distances are well above the single bond values. Therefore, La_2SbO_2 can be considered as a Mott insulator, in which the poor overlap between Sb *p*-orbitals prevents the charge carrier propagation and, as a consequence, leads to the semiconductor-type conductivity.

In the rest of the RE_2SbO_2 compounds, the Sb–Sb distances are shorter and remain almost constant through the series. Although the Zintl-type Sb^{2-}–Sb^{2-} dimers could not be

established from the structural analyses, previous studies[80, 95] suggested that the long range Sb–Sb interactions (ca. 3.3Å) may still influence the local electronic structure. In RE_2SbO_2, such interactions will cause energy separation between the bonding and anti-bonding states of antimony dimers, thus introducing a pseudo-gap at the vicinity of the Fermi level. However, presence of a pseudo-gap alone is insufficient to elucidate the diverse electrical behaviors of the RE_2SbO_2 phases. RE_2SbO_2 (other than La_2SbO_2) possess significant Sb site disorder, which can be correlated to the Sb *x*-coordinate shift. According to Anderson,[83] a significant atomic disorder leads to the localization of states at the top and bottom of bands, where the density of states diminishes. In case of RE_2SbO_2, such localized states resulting from the Sb disorder would appear around the created pseudo-gap. Thus, in the RE_2SbO_2 series (other than La_2SbO_2), the observed semiconductor-type behaviors stem from the Anderson localization of the states within the pseudo-gap and around the Fermi level. A few arguments developed by Mott and Davis[97] will be used in the following discussion to reveal the nature of the observed electrical properties. Figure 5.6 shows three proposed charge carrier activation mechanisms: a) hopping between localized states; b) thermal activation into localized states; c) thermal activation into non-localized states. While each of the three mechanisms may contribute to the measured electrical properties, the chemical pressure in the unit cell will determine which one is the dominant one by affecting the Sb site disorder.

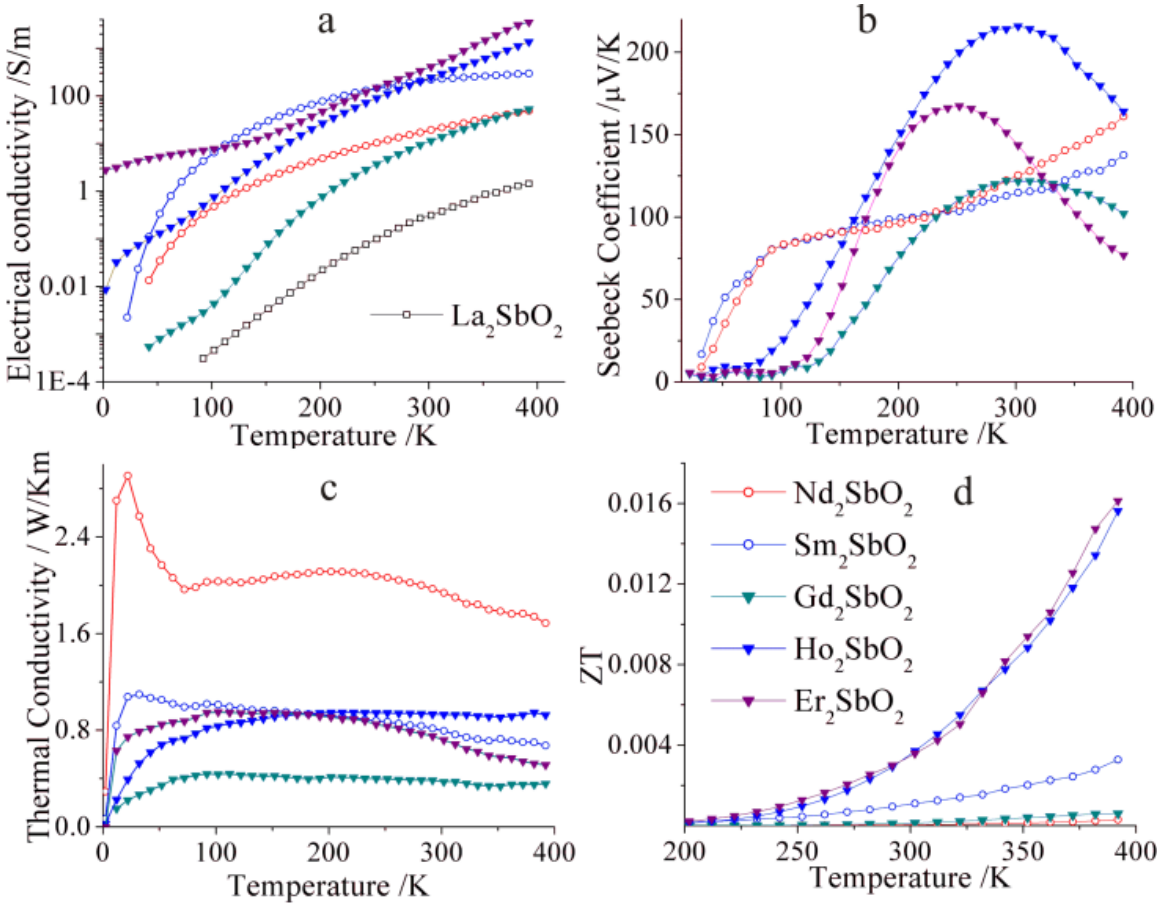

Figure 5.6. Electrical conductivities (a), Seebeck coefficents (b), thermal conductivities (c) and Figure of Merit *ZT* (d) of the RE_2SbO_2 compounds in the rage of 0–400K (200–400K for ZT).

First of all, the energy range of localization is proportional to the extent of disorder, which is reflected by the Sb shifts (Figure 5.3). When unit cells are big as in Nd_2SbO_2 and Sm_2SbO_2, the Sb disorder is large and electronic states within an extended energy range are localized (Figure 5.6a). Also because of the large atomic displacements, a range of Sb–Sb distances is accessible to the charge carriers. The combined outcome is a variable-range hopping (other than between the nearest neighbors), which allows charge carriers to propagate through the low-energy pathways at lower temperatures. Indeed, conductivity of Nd_2SbO_2/Sm_2SbO_2 obeys the variable-range hopping (VRH) formula,

$$\sigma \propto \exp\left(T^{-1/(d+1)}\right) \quad (5\text{-}1)$$

Where d is the dimensionality of the hopping pathways.[98] A method of Hill[99] was employed to establish the dimensionality of the variable-range hopping. In the low-temperature region, the VRH conduction in the two compounds was confirmed by the linearity of the double logarithmic plot of the activation energy over temperature *vs.* inverse of temperature (Figure 5.7). Thus, the charge carriers are tunneling through the random potential created by localization, as shown in Figure 5.6a, i.e. they do not need to be thermally promoted to high-energy extended states. The VRH behavior is also manifested in the thermoelectric powers of Nd_2SbO_2 and Sm_2SbO_2 phases. At low temperatures, their Seebeck coefficients increase significantly, as the charge tunneling requires little thermal energy as long as a large number of hopping pathways are available for the charge carriers. However at high temperatures, thermoelectric power is rather weak as its value depends on the change in the chemical potential, which is small for a tunneling mechanism.

As the *RE* atomic size decreases, the Sb atoms become more spatially constrained towards the ideal 2*a* atomic site by the neighboring *RE* atoms. As a result, the energy range of localization decreases for the heavier rare-earths. In the Ho and Er analogs, thermal excitation of charge carriers into the non-localized states in the conduction band becomes more dominant with increasing temperature (Figure 5.6c). Since the boundary (mobility edge) between the localized and non-localized states is associated with a change in the charge carrier mobility, μ, the electrical conductivities of the smaller RE_2SbO_2 phases are improved at higher temperatures (above 250K). The Seebeck

coefficients of Ho_2SbO_2 and Er_2SbO_2 are also enhanced (above 200K) as a change in the chemical potential originating from the carrier excitation process is greater than the energy range of the localized states.

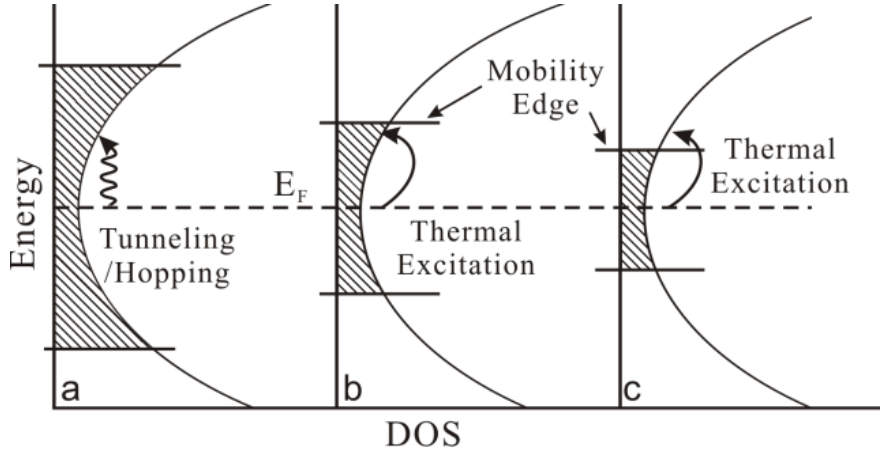

Figure 5.7. DOS at the Fermi level in the middle of a pseudogap. The shaded region represents localized states. The mobility edge is marked at boundary between the localized and the non-localized states. Three charge carrier activation mechanisms are shown: a) hopping between the localized states; b) thermal activation into localized states; c) thermal activation into non-localized states.

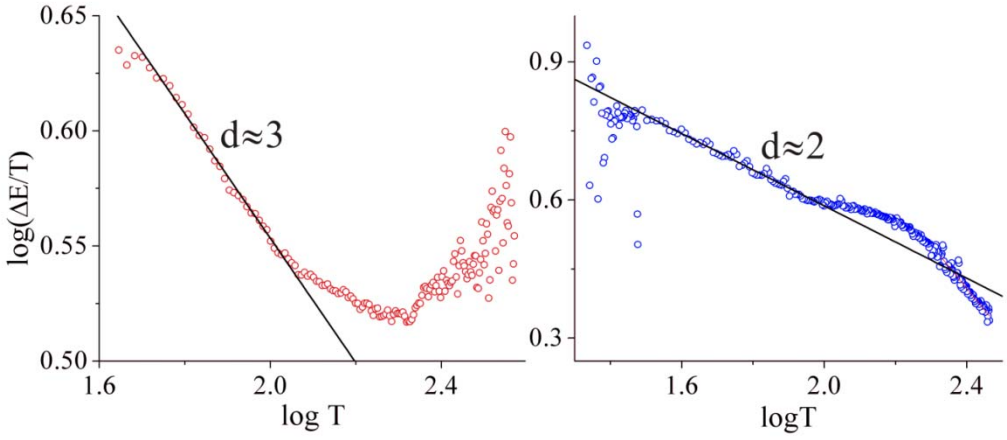

Figure 5.8. Double logarithmic plot of ΔE/T vs. T. The linear regions indicate the variable range hopping (VRH) with *d* being the dimensionality of the hoping mechanism. The activation energy was extracted from the derivative of $\ln \sigma / (1/T)$.[99] The dimensionality, *d*, of the VRH is determined from the slope of the linear fit.

The Gd_2SbO_2 phase, with an intermediate unit cell size, possesses a medium degree of the Sb displacement. As a result, the localized states are more extended than in the Ho/Er analogs while the range of atomic distances available for the hopping process is narrower than in the Sm/Nd analogs. Since there are fewer energy-equivalent electronic states for a charge carrier to tunnel into, the charge carriers are thermally activated. As a result, the Gd_2SbO_2 phase displays transport properties similar to those of the late members of the series. However, as the energy range of the localization is broad, the charge carriers are only excited into the localized states below the mobility edge (Figure 5.6b). The first consequence of such activation mechanism is a low electrical conductivity due to the low mobility. The less obvious outcome is a weaker thermoelectric power, since, according to Mott and Davis, only a part of the thermal activation energy contributes to the change in chemical potential, the rest is consumed by the hopping mechanism as the charge carriers propagate between the localized states.[97]

The Sb site disorder is also reflected in the thermal conductivities of the RE_2SbO_2 phases. Since the samples were cold pressed, a correction, representing experimental densities, was applied to the data following the method of Klemens.[100] The thermal conductivities of the RE_2SbO_2 phases (Figure 5.8**)** were corrected for the porosity of the cold pressed sample by applying equation (5-2):

$$\frac{\kappa_p}{\kappa_d} = 1 - \frac{4}{3}\phi \qquad (5\text{-}2)$$

Where κ_p and κ_d are the thermal conductivities of the porous and dense samples, respectively. The sample porosity, φ, is calculated from the experimental density ρ_{bulk} and the theoretical density ρ_{eff} of the material by equation (5-3).[101]

$$\phi = \frac{\rho_{bulk} - \rho_{eff}}{\rho_{eff}} \quad (5\text{-}3)$$

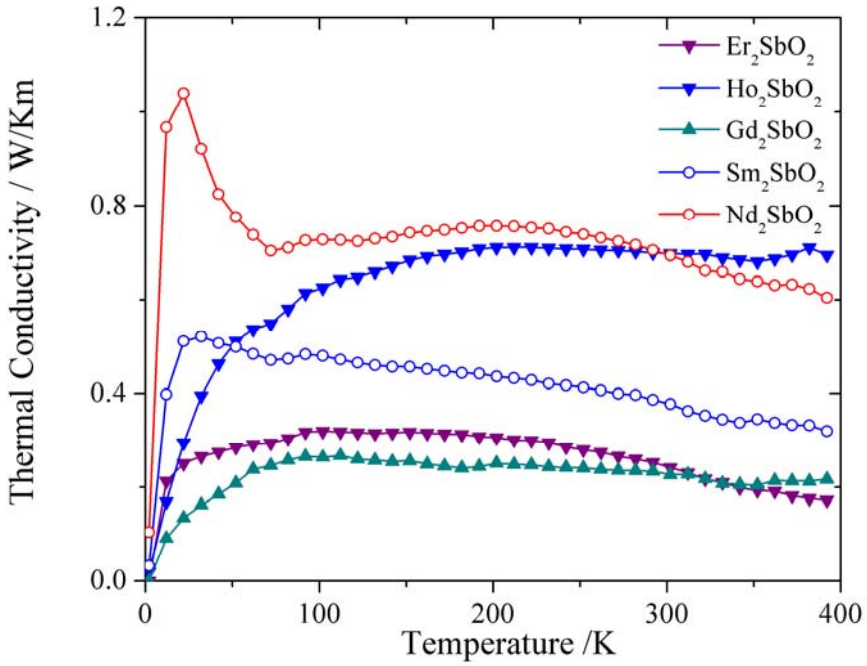

Figure 5.9. The thermal conductivities of the RE_2SbO_2 phases without the density corrections.

The relatively low thermal conductivities of the RE_2SbO_2 compounds (Figure 5.5c) is likely due to the Sb disorder. The dimensionless figure-of-merit, ZT, which combines the three transport parameters, is presented in Figure 5.5d. As shown, the RE_2SbO_2 compounds with small *RE* elements have larger thermoelectric efficiencies as a result of the simultaneous enhancement in the Seebeck coefficient α and electrical conductivity σ.

5.5 Conclusions

In summary, the size of the rare-earth elements was exploited as a chemical pressure to tune the Sb disorder in the RE_2SbO_2 phases. As a result, the RE_2SbO_2 materials with the same structure and charge carrier concentration exhibit a range of transport behaviors.

The size of the unit cell governs the degree of the Sb site disorder and Sb–Sb distances, both of which determine a dominant charge carrier transport mechanism. Thus, rather than changing uniformly within the series, the transport properties of some analogs are unique due to different activation processes. Consequently, the thermoelectric properties of these compounds are improved without compromising the electrical conductivity. The RE_2SbO_2 compounds are, by no means, the most efficient thermoelectric materials. However, this series illustrates possibilities of overcoming the classical challenges in thermoelectric research. Although the actual physics in these systems may be more complex, experimentally, the decoupling of electrical conductivity and thermopower was indeed achieved by perturbing the charge carrier transport mechanism without modifying the carrier concentration.

Chapter 6. Impact of Structural Ordering and Disordering on the Thermoelectric Properties of the Ho_2SbO_2 Phases

Two solid state phases sharing the common composition of Ho_2SbO_2 were prepared from different synthetic routes. The Ho_2SbO_2 compound obtained from high-temperature sintering adopts the *anti*-$ThCr_2Si_2$ type structure with the *I*4/*mmm* space group, while the structure of the low-temperature counterpart belongs to the orthorhombic *Fmmm* space group. Despite the structural similarities, the two phases displayed distinctly different semiconductor-type electrical behaviors. The observed physical properties can be attributed to the local atomic order/disorder associated with the Sb atoms, which is ultimately controlled by the symmetry of the structures. The impact of the local structural features on the thermoelectric properties of the Ho_2SbO_2 compounds is discussed from the perspective of disorder-induced charge carrier localization.

6.1 Introduction

The two compromising electrical properties that determine the thermoelectric efficiency, ($ZT = \alpha^2 \sigma T / \kappa$), the Seebeck coefficient (α) and the electrical conductivity (σ), are both related to the electronic band structure at the vicinity of the Fermi level, while the third parameter, thermal conductivity (κ), is sensitive to disorder in the structure.[1] Chemically increasing the carrier concentration in a degenerate semiconductor generally improves its electrical conductivity since electrical conductivity, σ, is directly proportional to a carrier concentration, n, through $\sigma = ne\mu$.[2] However, the Seebeck

coefficient (α) is typically compromised in the process as it is inversely related to the carrier concentration through the following equation.[2]

$$\alpha = \left(\frac{8\pi^2 {k_B}^2}{3eh^2}\right) mT \left(\frac{\pi}{3n}\right)^{2/3} \quad (1\text{-}9)$$

These relationships represent limitations of chemical doping for optimizing the power factor, $\alpha^2\sigma$. Many research attempts have been undertaken to achieve a higher power factor by increasing one of the two parameters while keeping the other one constant.[3] However, similar results are rarely realized in homogeneous bulk materials through chemical manipulations.

Another approach to optimize the power factor is to perturb the crystal structure of the thermoelectric phase. Structural modifications such as local disorder or substructure formation usually lead to alterations in the materials' electronic band structure, which, in turn could cause changes in the transport properties of the materials. For a thermoelectric material, a subtle structural modification could lead to a significant improvement in its performance. The impact of sub-structural details on the electronic properties can be observed for many antimony-based thermoelectric materials, where the complex Sb−Sb interactions give rise to desirable band structures.[80] In other phases, such as β-Zn_4Sb_3, disordering caused by atomic deficiency and displacement yielded low thermal conductivity.[33, 102, 103] Recently, Liu *et al.* have illustrated that the disordered substructure in the crystalline $Cu_{2-x}Se$ phase can lead to "liquid-like" behavior of the Cu ion, thus produces extraordinary thermoelectric performances.[104]

Previously,[105] we have illustrated the impact of local structural disorder on the thermoelectric behaviors of the RE_2SbO_2 compounds (*RE* = La, Nd, Sm, Gd, Ho and Er).

As shown in Figure 5.1, These compounds adopt a modified *anti*-$ThCr_2Si_2$ type structure with the *I*4/*mmm* space group.[54] The structure consists of a strongly disordered Sb sub-lattice sandwiched between RE_2O_2 layers. Despite of their compositional similarities, the bulk RE_2SbO_2 samples displayed distinctly different semiconducting behaviors, where as the extent of the Sb atomic displacement was the only structural variable. As the degree of the Sb atomic displacement was limited by applying chemical pressure, fine adjustments of the electronic band structure were achieved, which ultimately lead to simultaneous improvement of Seebeck coefficient and electrical conductivity in the bulk material.

The systematic study of the iso-structural RE_2SbO_2 compounds demonstrated the possibility of physical property optimization through perturbations of disordered local structure, however, there lacks a direct comparison between the locally disordered RE_2SbO_2 system and a fully ordered one. In this work, the preparation, crystal structure, physical properties and electronic structure of the fully ordered Ho_2SbO_2 phase will be discussed. Each of these aspects will be compared to the disordered Ho_2SbO_2 analog in order to depict the fundamental impact of the Sb site disorder on the thermoelectric properties of the RE_2SbO_2 phases.

6.2 Experimental

High purity Ho_2SbO_2 samples (>90 wt. %) were prepared by four different routes. Each synthetic method uses binary HoSb as precursor, which was prepared from elemental rare-earth metals (99.9 wt. %, CERAC Inc) and antimony (99.999 wt. %,

CERAC Inc) following the previously reported synthetic route.[106] The binary HoSb, powdered Sb metal and Ho_2O_3 powder (99.99 wt. %, Rhône-Poulenc, pre-fired at 1273K for 12hrs) were mixed in stoichiometric ratio and pressed into 0.5g pellets in an Ar filled glove box. The starting materials were subjected to different heat treatments under different environments. Sample A and B were prepared by sealing the cold pressed pellets in Ta tubes and sintered in a radio-frequency induction-heating system. After sintering at 1573K for 2 hours, sample A was analyzed while sample B was then annealed at 1273K for 20 hours with the original Ta tube. Along with the sintered pellets, small amounts of silver metallic powder were also extracted from the Ta tubes containing samples A and B, which were later identified as Ta_3Sb.[57] Sample C and D were prepared by sealing the pellets of staring material in evacuated silica tubes 10-15cm in length, then heating the ampoule to 1073 K at a rate of 150 K /hour. The cold pressed pellets crumble into gray-black powder after the sintering at 1073 K for 20 hours. Subsequently, without air contact, both samples were ground and re-sealed in evacuated silica tubes and then directly annealed at 1273 K for 20 hours, except sample D which was enclosed in a Ta jacket inside the silica tube. These samples both appeared to be black, sintered pellets.

The samples were subjected to X-ray powder diffraction analysis on a PANalytical X'Pert Pro diffractometer with an X'Celerator detector and $CuK_{\alpha 1}$ radiation. Diffraction data in the 20–70º 2θ range were collected. The full-profile Rietveld refinement (Rietica program[63]) was used to refine the lattice constants and assess the purity of the bulk products. The electrical resistivity, Seebeck voltage and thermal conductivity of the prepared Ho_2SbO_2 samples were measured in the 2–400 K region on a QD PPMS

instrument. In order to understand the effect of atomic arrangement on the physical properties of the Ho_2SbO_2 compounds, tight-binding, linear-muffin-tin-orbital calculations using the atomic sphere approximation[65] (TB-LMTO-ASA) were performed with the Stuttgart program. [66]

6.3 Result and Discussion

6.3.1 Structural Analysis

Samples A and B were identified as Ho_2SbO_2 with the *I*4/*mmm* space group by X-ray powder diffraction and Rietveld refinement. The structural model used in the refinement was reported previously,[105] where the Sb atoms were shifted away from the ideal 2*a* position along *x*-direction into an 8*i* position with an occupancy of ¼. Samples C and D at 1273K yielded X-ray powder diffraction patterns similar to that of the high-temperature samples, suggesting the general similarities between the phases in terms of atomic arrangement. However, when compared to the X-ray powder diffraction patterns of A and B, those of C and D displayed a shift for the major peak at ~30.9° 2θ and a split peak at 33° 2θ. These observations were understood as evidence of symmetry breaking from the parent tetragonal structure. Since the split peak at 33° 2θ corresponds to the (1 1 0) lattice plane in the original structure, the nature of the symmetry breaking was believed to be associated with the ordering of Sb.

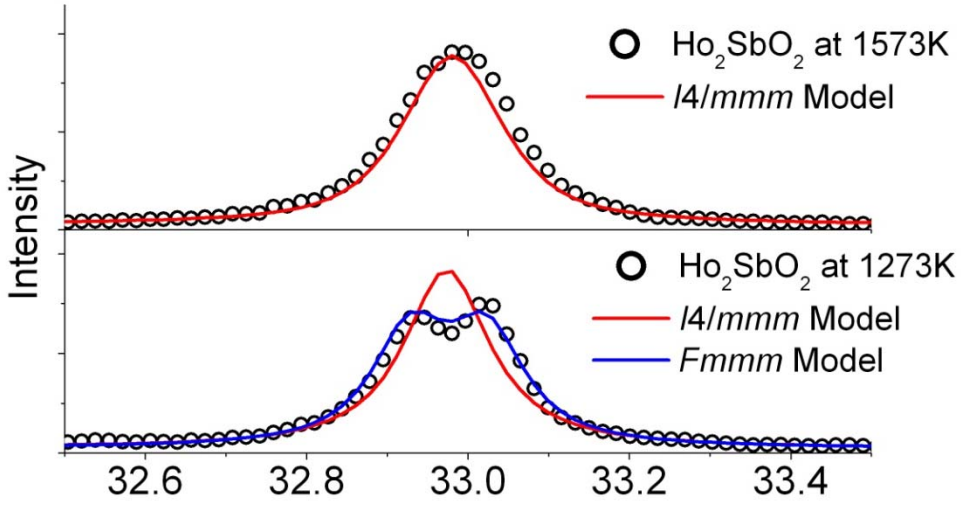

Figure 6.1. The two structural models (*I*4/*mmm* and *Fmmm*) refined against the X-ray powder diffraction data collected from the Ho_2SbO_2 samples

A low symmetry structural model with the orthorhombic *Fmmm* space group (a sub-group of the tetragonal *I*4/*mmm* space group) was constructed and refined against the X-ray powder diffraction data. As in Figure 6.1, the X-ray powder diffraction data collected from samples C and D can be well described by the orthorhombic structural model but not by the parent tetragonal model. The orthorhombic structure also consists of alternating Ho_2O_2 layers and Sb layers, but with Sb atomic position localized on the 4*a* site. In order to accommodate the Sb localization, the Ho_2O_2 sub-lattice relaxes so that the Ho atoms above and below the Sb layer form a diamond-shaped arrangement (Figure 6.2). The transformation from the tetragonal *I*4/*mmm* to the orthorhombic *Fmmm* structure gives rise to two major modifications to the antimony local environment:

1. In the orthorhombic cell, the antimony site localization fixes the distance between the neighboring Sb atoms to 3.831Å, where as the tetragonal structure with the largest Sb displacement yields Sb−Sb distances between 3.256Å and 4.405Å.

2. The Ho_2O_2 sub-lattice relaxation in the *Fmmm* structure creates two Ho−Sb distances at 3.491Å and 3.416Å, while the disordered structure (*I*4/*mmm*) allows Ho−Sb distances of 3.303Å and 3.621Å.

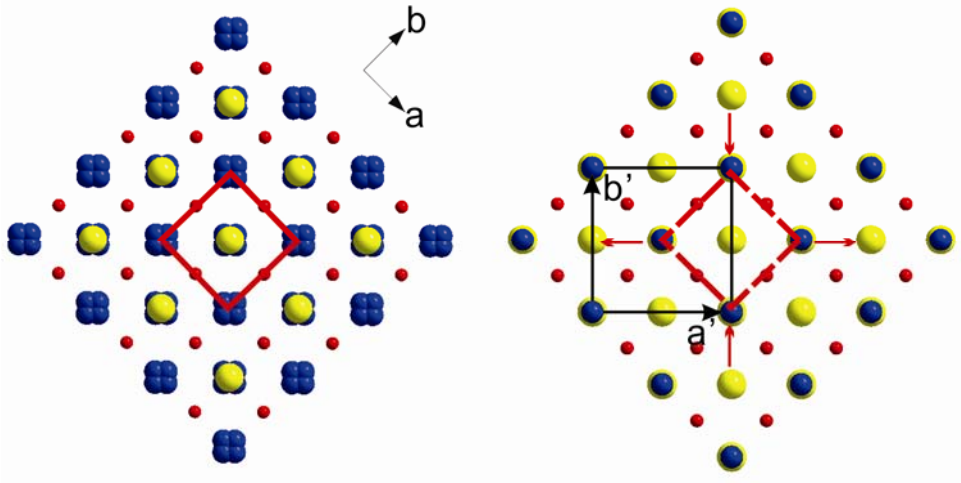

Figure 6.2. Transformation from the disordered *I*4/*mmm* structure (left) to the ordered *Fmmm* structure (right). The lattice is shown with respect to the original *I*4/*mmm* unit cell (marked red). The arrows show the direction of lattice relaxation to form the *Fmmm* super cell (marked black).

6.3.2 Electrical Properties

Since the Sb states dominates the electronic band of the Ho_2SbO_2 phases at the vicinity of the Fermi level, the changes in the Sb chemical environment in turn impact the electrical properties of the bulk material. As shown in Figure 6.3, with the increasing temperature, the electrical conductivity of the ordered orthorhombic Ho_2SbO_2 increases at a much lower rate than that of the disordered tetragonal phase. The Seebeck coefficients of the two phases also show distinctly different features (Figure 6.3, right). These significant changes can be explained within the framework of Anderson and Mott type insulators.[83, 107]

The theory of Anderson localization states that a significant atomic disorder leads to the localization of states at the top and bottom of bands, where the density of states diminishes. Previous studies[80, 95] suggested that the long range Sb–Sb interactions (ca. 3.3 Å), such as those in the disordered tetragonal Ho_2SbO_2, will cause energy separation between the bonding and anti-bonding states of antimony dimers, thus introducing a pseudo-gap at the vicinity of the Fermi level. The diminishing energy states within the pseudo-gap then become localized due to the Sb atomic disordering. The above described condition gives rise to the semiconductor property observed in the tetragonal Ho_2SbO_2, despite the electron poor formula, $Ho^{3+}{}_2Sb^{3-}O^{2-}{}_2$. Since the localized states only exist in a small energy region defined by the pseudo-gap, the charge carriers in the conduction band are more prone to excitation over the so called "mobility edge" above the localized states.[97] The direct result of such thermal excitation is the large increase in electrical conductivity of the tetragonal Ho_2SbO_2 at high temperatures. In terms of Seebeck coefficient, the narrow pseudo-gap becomes a disadvantage as the compensating charge carriers are also excited across the localized region at higher temperatures causing a drop in Seebeck coefficient.

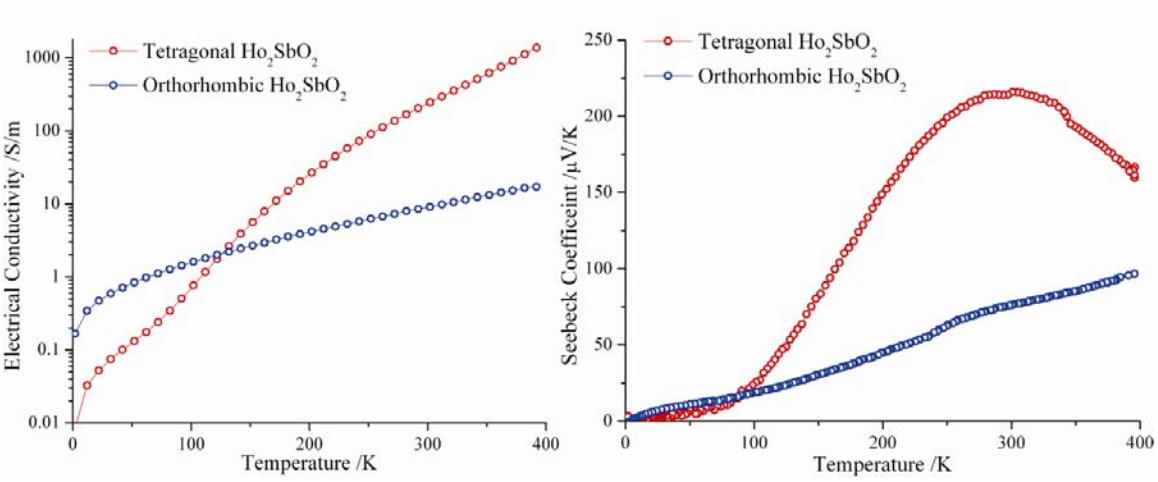

Figure 6.3. The electrical conductivity (left) and Seebeck coefficient (right) of the ordered orthorhombic Ho_2SbO_2 and that of its disordered tetragonal counterpart at temperatures between 0 and 400K.

Without the disorder on the antimony site, Anderson localization fails to elucidate the origin of semiconductor properties observed for the orthorhombic Ho_2SbO_2 phase. This phase, alternatively, falls into the category of Mott insulators, in which the poor overlap between orbitals prevents the charge carrier propagation and, as a consequence, leads to the semiconductor-type conductivity. The recent study by Hosono *et al.*[52] on the RE_2BiO_2 (*RE* = Rare-earth or Yttrium) compound series has illustrated the impact of Bi−Bi orbital overlap on the physical properties of the bulk materials. The RE_2BiO_2 compounds displayed a metal-insulator transition as the larger early rare-earth elements were replaced by the smaller late rare-earth elements. While the metallic behavior of the late *RE* analogs was expected from their electron count, the early *RE* analogs, with larger lattice parameters, exhibited semiconducting properties. As the Bi−Bi distances increase in the larger analogs, the poor overlaps between the neighboring Bi orbitals gave rise to the semiconductor properties.[52] Similarly, the Sb atoms, ordered on the 4*a* sites of the

orthorhombic Ho_2SbO_2 structure, are too separated to maintain the metallic states around the Fermi level.

6.4 Summary

In summary, the Ho_2SbO_2 compound adopting an orthorhombic *Fmmm* symmetry was prepared and characterized by X-ray powder diffraction. The bulk sample of this phase was subjected to physical property measurements. The electrical conductivity and Seebeck coefficient of the orthorhombic Ho_2SbO_2 compound were compared against those of the tetragonal Ho_2SbO_2 compound with *I*4/*mmm* symmetry. The subtle atomic disorder/order transition on the Sb sites due to the symmetry breaking (from *I*4/*mmm* to *Fmmm*) resulted in significant differences in the physical properties of the two phases. The distinctly different semiconducting behaviors of tetragonal and orthorhombic Ho_2SbO_2 were explained as a result Anderson and Mott-type charge carrier localization, respectively.

The experimentally observed physical property alterations are evidently linked to the local structural modifications on the Sb site, whose electronic states dominate the band structure at the vicinity of the Fermi level. Further structural studies are required to evaluate the detail changes in the Sb atomic arrangements. Single crystal X-ray diffraction studies may be a viable route for such investigations, as long as high quality single crystals can be obtained. However, the challenges arise in preparing crystalline samples of the orthorhombic Ho_2SbO_2 phase, since the low symmetry structure is only preserved under the lower sintering temperature (1273K) that is not favorable for crystal

growth. To find an ideal temperature to grow the orthorhombic Ho_2SbO_2 crystals, parallel preparative experiments have to be conducted at various temperatures and sintering times.

Chapter 7. Disorder Controlled Electrical Properties in the $Ho_2Sb_{1-x}Bi_xO_2$ Systems

High purity bulk samples of the $Ho_2Sb_{1-x}Bi_xO_2$ phases (x = 0, 0.2, 0.4, 0.6, 0.8, 1.0) were prepared and subjected to structural and elemental analysis as well as physical property measurements. The Sb:Bi ratio in the $Ho_2Sb_{1-x}Bi_xO_2$ system could be fully traversed without disturbing the overall *anti*-$ThCr_2Si_2$ type structure (*I*4/*mmm*). The single crystal X-ray diffraction studies revealed that the local atomic displacement on the Sb/Bi site is reduced with the increasing Bi content. Such local structural perturbations lead to a gradual semiconductor-to-metal transition in the bulk materials. The significant variations in the electrical properties without change in the charge carrier concentration are explained within the frame of the disorder-induced Anderson localization. These experimental observations demonstrated an alternative strategy for electrical properties manipulations through the control of the local atomic disorder.

7.1 Introduction

Among all the properties of materials, the charge carrier transport properties display the largest variability; for instance, the room-temperature resistivity for different materials spans more than 32 orders of magnitude.[108] The nature of the electrical properties depends on the electronic structure of a materials and, generally, the presence of a forbidden energy range (band gap, E_g) at the vicinity of the Fermi Level differentiates insulators from metals.[27] Semiconductors are insulators with relatively

small band gaps and they exhibit intermediate electrical conductivities, which depend on the number of free charge carriers, n, the carrier charge, e, and mobility, μ, through Equation 1-7.

$$\sigma = ne\mu \text{ [S·m]} \quad (1\text{-}7)$$

In a non-degenerate semiconductor, the number of charge carriers excited across the band gap at a given temperature is related to the band gap energy, E_g, through the Boltzmann relationship (Equation 1-8) [109]

$$n \propto exp\left(-\frac{\Delta E}{kT}\right) \quad (1\text{-}8)$$

For a given semiconductor, a typical approach to tune its electrical properties involves modifying its charge carrier concentration via doping or altering its band gap via structural modification. However, in conventional bulk semiconductors, impurity introduction is limited by the dopant solubility, while the band gap engineering is largely restricted by the material's crystal structure.[108, 110]

Mott[111] and Anderson[83] insulators are semiconductors that should be metallic within the conventional band theory. Electrical properties of such materials can be extensively modified since their electronic structures are not solely determined by their average crystal structures. The insulator-to-metal transition observed in the RE_2BiO_2 series (*RE* = rare-earth elements, *anti*-$ThCr_2Si_2$ structure,[53] Figure 7.1, right) is an excellent example of such modifications without a structural alteration or chemical doping. As larger rare-earth atoms are replaced by smaller ones, the isostructural RE_2BiO_2 phases convert from insulators to metals.[52] The semiconducting RE_2BiO_2 phases, containing early *RE* atoms, can be rationalized as Mott insulators where the poor overlap between the Bi 6*p* fails to

sustain the metallic state predicted by the electronic structure calculations. In the late *RE* analogs with smaller unit cells and shorter Bi–Bi distances the metallic character of the Bi electronic band becomes dominant due to a better Bi–Bi orbital overlap.[52]

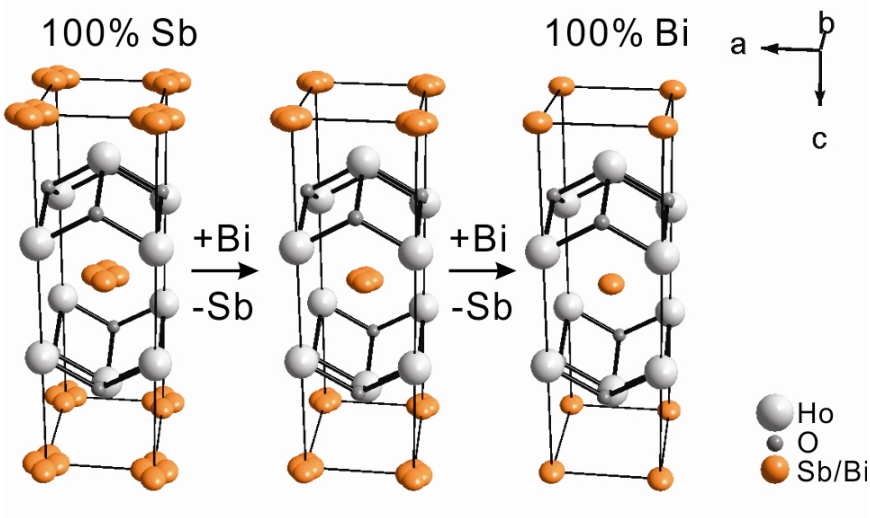

Figure 7.1. The transition from the average Ho_2SbO_2 structure (left) to the Ho_2BiO_2 structure (right) through increasing Bi content.

Another interesting case of electrical property perturbation was observed in the semiconducting RE_2SbO_2 phases (*RE* = rare-earth elements, excluding La). These compounds adopt the same average crystal structure as RE_2BiO_2. Recent structural studies,[54] however, suggested that the Sb atoms are shifted away from the ideal 2*a* position into the 8*i* position with an occupancy of ¼. Within the *ab* plane, such atomic displacement creates random Sb occupancies on the 4-fold degenerate positions (Figure 7.1, left) and, according to the Anderson localization theory,[97] can result in the localization of charge carriers. But as smaller *RE* atoms are introduced into the structure, the degree of randomness in the Sb layer diminishes and different charge carrier transport mechanisms develop from the variable range hoping in Nd_2SbO_2 to the thermal excitation

in Er_2SbO_2. As a result, the electrical resistivity of the RE_2SbO_2 compounds span three orders of magnitude without chemical doping, and their thermopower shows distinctly different temperature dependencies with minimal structural modifications.[105]

The diversity of the electrical properties in the RE_2SbO_2 and RE_2BiO_2 phases stems from their unique atomic arrangement. Their structure can be considered as a natural superlattice[35] of the RE_2O_2 and Sb/Bi layers, with the RE_2O_2 slabs dictating the lattice dimensions in the *ab* plane and the Sb/Bi layers controlling the charge carrier transport. In both the RE_2SbO_2 and RE_2BiO_2 series, the size of the RE_2O_2 slabs was used to govern the interactions and transport properties within the Sb/Bi layer. Another approach would be to fix the dimensionality of the RE_2O_2 slab and to modify the structural and electronic behavior of the Sb/Bi layer via intra-layer Sb/Bi substitution. If the conclusions regarding the transport properties in the RE_2SbO_2 and RE_2BiO_2 phases are correct, then the electrical conductivity of the $RE_2Sb_{1-x}Bi_xO_2$ phases (*RE* is a late rare-earth) should change from semiconducting to metallic as the Bi amount increases. In this work, we present the structural and transport properties of the $Ho_2Sb_{1-x}Bi_xO_2$ phases. The Ho series has been deliberately chosen, as the Ho_2BiO_2 phase is metallic[52] and Bi atoms are well localized on the 2*a* position.[112] On the other hand, the Ho_2SbO_2 phase is semiconducting and features disordered Sb atoms.[105]

7.2 Experimental

7.2.1 Synthesis

The $Ho_2Sb_{1-x}Bi_xO_2$ (x = 0.2, 0.4, 0.5, 0.6, 0.8 and 1) samples, with purities of 95 wt. % or greater, were prepared form Ho metal filings (99.9 wt. %, CERAC Inc), powdered Sb/Bi elements (99.999 wt. %, CERAC Inc) and Ho_2O_3 (99.99 wt. %, Rhône-Poulenc, pre-fired at 1000 ℃ for 12hrs). The starting materials were mixed in the stoichiometric ratio and pressed into 0.5 gram pellets in an Ar filled glove box. Subsequently, the cold-pressed pellets were sealed in evacuated silica tubes and sintered at 800℃ for 48 hours. The pre-reacted samples were then re-ground and re-pressed in the glove box. The samples were sealed again in evacuated silica tubes and heated at 1000 ℃ for 20 hours. The products were dense black pellets stable in air. The $Ho_2Sb_{1-x}Bi_xO_2$ phases with varied Sb:Bi ratios were also produced via high-temperature sintering at 1500 ℃ in order to obtain single crystals suitable for diffraction studies. The details of the high temperature reactions in the induction furnace have been reported for the preparation of the Ho_2SbO_2 sample.[105]

7.2.2 X-ray Powder Diffraction

The bulk samples were subjected to X-ray powder diffraction analysis on a PANalytical X'Pert Pro diffractometer with an X'Celerator detector and $CuK_{\alpha 1}$ radiation. Diffraction data were collected in the 20–70° 2θ range. A full-profile Rietveld refinement (Rietica program[63]) was used to refine the lattice constants and assess the purity of the bulk products. The extracted unit cell dimensions are listed in Table 7.1.

It has been suggested that oxygen deficiency in La_2SbO_2 stabilized the structure and in turn resulted in its semiconductor-type electrical properties.[113] However, stoichiometric amounts of the oxide were used in the preparation of the $Ho_2Sb_{1-x}Bi_xO_2$ samples and yielded the desired phases quantitatively. All powder samples contained small quantities of Ho_2O_3 (<5 wt.%, Figure 7.2), whose formation can be attributed to the unreacted Ho_2O_3, losses of volatile Sb/Bi and the oxidation of remaining Ho at the contact between the sample pellets and the silica tube.

Table 7.1. Loading compositions of the $Ho_2Sb_{1-x}Bi_xO_2$ samples and the corresponding lattice parameters and unit cell volume determined by the powder X-ray diffraction.

Loading Compositions	*a* and *b* /Å	c /Å	Cell volume /Å^3
Ho_2SbO_2	3.83728(6)	13.1644(3)	193.841(6)
$Ho_2Sb_{0.8}Bi_{0.2}O_2$	3.83960(3)	13.1793(2)	194.296(3)
$Ho_2Sb_{0.6}Bi_{0.4}O_2$	3.84126(9)	13.1786(3)	194.454(9)
$Ho_2Sb_{0.4}Bi_{0.6}O_2$	3.84341(4)	13.1791(2)	194.679(5)
$Ho_2Sb_{0.2}Bi_{0.8}O_2$	3.84572(8)	13.1826(3)	194.965(8)
Ho_2BiO_2	3.85070(4)	13.1972(2)	195.686(4)

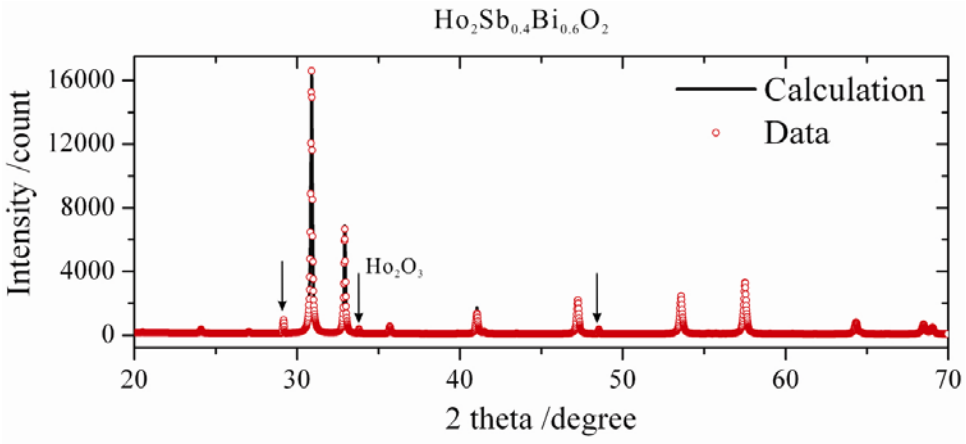

Figure 7.2. The Rietveld refinement of the $Ho_2Sb_{0.4}Bi_{0.6}O_2$ X-ray powder diffraction pattern. The arrows mark the Ho_2O_3 impurity peaks.

7.2.3 EDS Analysis

In order to confirm the Bi/Sb substitutions, the samples were analyzed by energy-dispersive X-ray spectroscopy (EDS). The EDS experiments were conducted on a JEOL 7000F scanning electron microscope. Copper metal was used to standardize the signals. For the bulk samples, as in Table 7.2, the fractions of Bi substitution obtained from the EDS experiments were in agreement with the loading composition. While the ratio between Ho and pnictogens (Sb + Bi) is close to 2:1, the accurate oxygen contents were not extracted due to the instrumental bias to light elements and the potential surface oxidation.

Table 7.2. Fraction of Bi substitution in the bulk samples determined by the EDS experiments (normalized to 2 Ho per formula).

Loading Composition	Atomic %			Fraction of Bi
	Ho	Sb	Bi	
Ho_2SbO_2	2	1	0	0
$Ho_2Sb_{0.8}Bi_{0.2}O_2$	2	0.66(2)	0.16(2)	0.20(3)
$Ho_2Sb_{0.6}Bi_{0.4}O_2$	2	0.54(4)	0.35(2)	0.39(4)
$Ho_2Sb_{0.4}Bi_{0.6}O_2$	2	0.50(2)	0.68(2)	0.58(4)
$Ho_2Sb_{0.2}Bi_{0.8}O_2$	2	0.32(2)	0.54(6)	0.63(7)
Ho_2BiO_2	2	0	1	1

7.2.4 X-ray single crystal studies

X-ray single crystal diffraction studies were performed on the crystals extracted from the high-temperature $Ho_2Sb_{1-x}Bi_xO_2$ samples (x = 0, 0.25, 0.5, 0.75, 100). Room-temperature diffraction data were collected on a STOE IPDSII diffractometer with MoK_α radiation in the whole reciprocal sphere. A numerical absorption correction was applied

based on the crystal shape that was originally derived from the optical face indexing but was later optimized against equivalent reflections using STOE X-Shape software.[60] Structural determination and refinement were performed using the SHELXL program.[62] Details of the structural investigation and refinement are listed in Tables 7.4 and Table 7.5. In the Ho_2SbO_2 structure, the Sb atoms were shifted from the standard 2*a* site (0, 0, 0) into the 8*i* site (*x*, 0, 0) to properly describe the delocalized Sb electron density, which is in agreement with previous studies.[54, 105] In case of Ho_2BiO_2, the Bi atoms were well described on the 2*a* site and the refinement for the disordered model (with the 8*i* site) did not converge. Similarly, the refinement of the $Ho_2Sb_{1-x}Bi_xO_2$ structure proceeded well only when the Sb/Bi atoms were placed into the 2*a* site. Because of the correlation between the vibrational parameters and the occupancy of the Sb/Bi site, one may question the refined Sb/Bi ratios. To verify the obtained compositions, single crystals subjected to the diffraction experiments were subsequently analyzed by energy-dispersive X-ray spectroscopy. The refined compositions showed reasonable agreement with the EDS results (Table 7.3). In order to relate the composition to the degree of the Sb/Bi delocalization, the Ho_2SbO_2 structure was also refined with the same model as the rest of the $Ho_2Sb_{1-x}Bi_xO_2$ series, i.e. with the Sb atoms in the 2*a* site.

Table 7.3. Anisotropic thermal parameters of the pnictogen atoms in the $Ho_2Sb_{1-x}Bi_xO_2$ structures.

Refined Composition	U_{11}	U_{33}	U_{11}/U_{33}	%Bi by EDS Analysis
Ho_2SbO_2	0.080(1)	0.015(1)	5.50	N/A
$Ho_2Sb_{0.69(3)}Bi_{0.31(3)}O_2$	0.045(1)	0.015(1)	2.98	0.32(2)
$Ho_2Sb_{0.63(5)}Bi_{0.37(5)}O_2$	0.049(2)	0.020(2)	2.53	0.30(4)
$Ho_2Sb_{0.41(1)}Bi_{0.59(1)}O_2$	0.038(3)	0.025(4)	1.52	0.60(2)
$Ho_2Sb_{0.36(8)}Bi_{0.64(1)}O_2$	0.038(2)	0.031(3)	1.21	0.62(2)
$Ho_2Sb_{0.25(9)}Bi_{0.75(9)}O_2$	0.045(3)	0.039(4)	1.15	0.82(5)
Ho_2BiO_2	0.023(1)	0.015(1)	1.48	N/A

Table 7.4. Crystallographic data and refinement results for the $Ho_2Sb_{1-x}Bi_xO_2$ single crystals, MoKα radiation.

Refined Composition	Ho_2SbO_2	$Ho_2Sb_{0.69}Bi_{0.31}O_2$	$Ho_2Sb_{0.63}Bi_{0.37}O_2$	$Ho_2Sb_{0.41}Bi_{0.59}O_2$	$Ho_2Sb_{0.36}Bi_{0.64}O_2$	$Ho_2Sb_{0.25}Bi_{0.75}O_2$	Ho_2BiO_2
Formula weight	483.61	510.65	515.89	535.08	539.87	548.60	570.84
Temperature /K				298(2)			
Space group				*I*4/*mmm*			
Unit cell dimensions, Å	*a* = 3.8306(5) *c* =13.066(3)	*a* = 3.8380(5) *c* =13.162(3)	*a* = 3.8390(5) *c* =13.152(3)	*a* = 3.8485(5) *c* = 13.211(3)	*a* = 3.8489(5) *c* =13.230(3)	*a* = 3.8500(5) *c* =13.205(3)	*a* = 3.8544(5) *c* =13.194(3)
Volume /Å3	191.72(5)	193.88(5)	193.84(5)	195.67(5)	195.99(7)	195.73(5)	196.02(5)
Z				2			
d_{calc} /g cm^{-3}	8.377	8.747	8.839	9.082	9.148	9.308	9.671
Abs. coeff., mm-1	47.657	66.304	61.332	69.118	71.091	74.984	84.548
θ range / degrees	3.12 to 29.13	3.10 to 34.32	5.53 to 34.30	5.52 to 34.22	5.52 to 34.21	5.52 to 34.20	5.51 to 34.46
Index ranges	-5<=h<=4 -5<=k<=5 -16<=l<=17	-5 ≤ h ≤ 6, -5 ≤ k ≤ 6, -20 ≤ l ≤ 20	-5<=h<=6, -6<=k<=6, -20<=l<=20	-6<=h<=6, -6<=k<=4, -20<=l<=20	-6<=h<=6, -5<=k<=6, -20<=l<=15	-6<=h<=4, -6<=k<=6, -20<=l<=20	-6≤ h ≤6, -6≤ k ≤6, -20≤ l ≤19
Reflections collected	696	1353	1194	1166	1615	1267	1476
Independent reflections	105 (R_{int}=0.0438)	151 (R_{int}=0.0737)	151 (R_{int}=0.0885)	151 (R_{int}=0.1291)	150 (R_{int}=0.1324)	140 (R_{int} = 0.1526)	151 (R_{int} = 0.1057)
Completeness to max. 2θ	100%	98.7%	99.3%	98.7%	98.0 %	91.5%	96.2%
Data / parameters	150 / 9	150 / 10	150 / 10	151/9	150/10	140/10	151 / 9
Goodness-of-fit on F^2	1.237	1.019	0.777	1.009	0.904	0.785	1.038
Final R indices [I>2σ(I)]	R1 = 0.0219, wR2 = 0.0409	R1 = 0.0295, wR2 = 0.0451	R1 = 0.0351, wR2 = 0.1006	R1 = 0.0477, wR2 = 0.0818	R1 = 0.0331, wR2 = 0.0392	R1 = 0.0359, wR2 = 0.0501	R1 = 0.0309, wR2 = 0.0501
R indices (all data)	R1 = 0.0300, wR2 = 0.0418	R1 = 0.0426, wR2 = 0.0470	R1 = 0.0586, wR2 = 0.1216	R1 = 0.0993, wR2 = 0.0935	R1 = 0.0796, wR2 = 0.0465	R1 = 0.0807, wR2 = 0.0584	R1 = 0.0724, wR2 = 0.0601
Extinction coeff.	0.0064(9)	0.0032(6)	0.0030(2)	N/A	0.0037(6)	0.0032(7)	0.007(1)
Diffr. peak/hole, e/$Å^3$	2.337/-3.320	2.159/-2.200	2.810/-1.987	2.505/ -3.905	3.194/-1.884	3.424 / -2.620	2.184/-3.964

Table 7.5. Atomic coordinates of the for the $Ho_2Sb_{1-x}Bi_xO_2$ single crystals.

Atom	Site	Occupancy	x/a	y/b	z/c	U_{eq}
			Ho_2SbO_2			
Ho	4*e*	1	0	0	0.3360(1)	0.0120(3)
O	4*d*	1	0	0.5	0.25	0.017(2)
Sb	2*a*	1	0	0	0	0.0585(9)
			$Ho_2Sb_{0.69}Bi_{0.31}O_2$			
Ho	4*e*	1	0	0	0.3342(1)	0.0092(3)
O	4*d*	1	0	0.5	0.25	0.011(2)
Sb	2*a*	0.69(3)	0	0	0	0.035(1)
Bi	2*a*	0.31(3)	0	0	0	0.035(1)
			$Ho_2Sb_{0.63}Bi_{0.37}O_2$			
Ho	4*e*	1	0	0	0.3310(1)	0.0074(6)
O	4*d*	1	0	0.5	0.25	0.013(4)
Sb	2*a*	0.63(5)	0	0	0	0.039(2)
Bi	2*a*	0.37(5)	0	0	0	0.039(2)
			$Ho_2Sb_{0.41}Bi_{0.59}O_2$			
Ho	4*e*	1	0	0	0.3327(3)	0.0099(7)
O	4*d*	1	0	0.5	0.25	0.015(5)
Sb	2*a*	0.4(1)	0	0	0	0.033(2)
Bi	2*a*	0.6(1)	0	0	0	0.033(2)
			$Ho_2Sb_{0.36}Bi_{0.64}O_2$			
Ho	4*e*	1	0	0	0.3335(2)	0.0076(4)
O	4*d*	1	0	0.5	0.25	0.014(4)
Sb	2*a*	0.36(8)	0	0	0	0.036(2)
Bi	2*a*	0.64(8)	0	0	0	0.036(2)
			$Ho_2Sb_{0.25}Bi_{0.75}O_2$			
Ho	4*e*	1	0	0	0.3324(2)	0.0099(5)
O	4*d*	1	0	0.5	0.25	0.016(4)
Sb	2*a*	0.25(9)	0	0	0	0.043(2)
Bi	2*a*	0.75(9)	0	0	0	0.043(2)
			Ho_2BiO_2			
Ho	4*e*	1	0	0	0.3318(2)	0.0068(4)
O	4*d*	1	0	0.5	0.25	0.011(4)
Bi	2*a*	1	0	0	0	0.0209(7)

7.2.5 Physical Property Measurements

The sintered sample pellets were cut into bars of 6–7mm in length and 1.5–2.5 mm in width/height for electrical property measurements. Four-probe DC electrical resistivity was measured on a Quantum Design Physical Properties Measurement System (QD, USA) in the temperature interval of 2–400 K. Gold wires of 50 μm diameter were attached to the samples using silver ink. The electrical conductivities and Seebeck coefficients of the $Ho_2Sb_{1-x}Bi_xO_2$ samples in the range of 0–400K are shown in Figure 7.3.

7.3 Results and Discussion

7.3.1 Structural Features

In order to establish the Bi substitution in the $Ho_2Sb_{1-x}Bi_xO_2$ systems, the polycrystalline samples were qualitatively confirmed through the EDS analysis (Table 7.2). However, the powder X-ray diffraction revealed minimal changes in the lattice parameters despite large differences between the Sb and Bi atomic radii (1.45 Å and 1.60Å, respectively[114]). In the case of the pure binaries, the unit cell volume of HoBi (241.7 $Å^3$)[115] is ~5% larger than that of HoSb (230.4 $Å^3$).[38] While the atomic fraction of Sb/Bi is smaller in $Ho_2Sb_{1-x}Bi_xO_2$, the unit cell volume increase from Ho_2SbO_2 to Ho_2BiO_2 is less than 1%. Such small size effect can be related to the observed Sb atomic disorder in the Ho_2SbO_2 structure, in which the Sb atoms occupy a larger-than-usual volume.

As mentioned above, the powder diffraction studies indicate a relatively small lattice expansion and suggest, although indirectly, that the Sb/Bi environment become

tighter with the Bi concentration. The single crystal data confirm the latter argument. Figure 7.4 shows that, with the increasing Bi substitution, the anisotropic thermal parameters of the Sb/Bi 2*a* site are reduced exponentially in the *ab*-plane ($U_{11} = U_{22}$) with respect to the *c* direction (U_{33}). The diminishing U_{11}/U_{33} values suggest atomic localization within the pnictogen layer as the strongly disordered Sb atoms are replaced by the slightly dislocated or even fully ordered Bi atoms.

7.3.2 Electrical Properties and Lattice Disorder

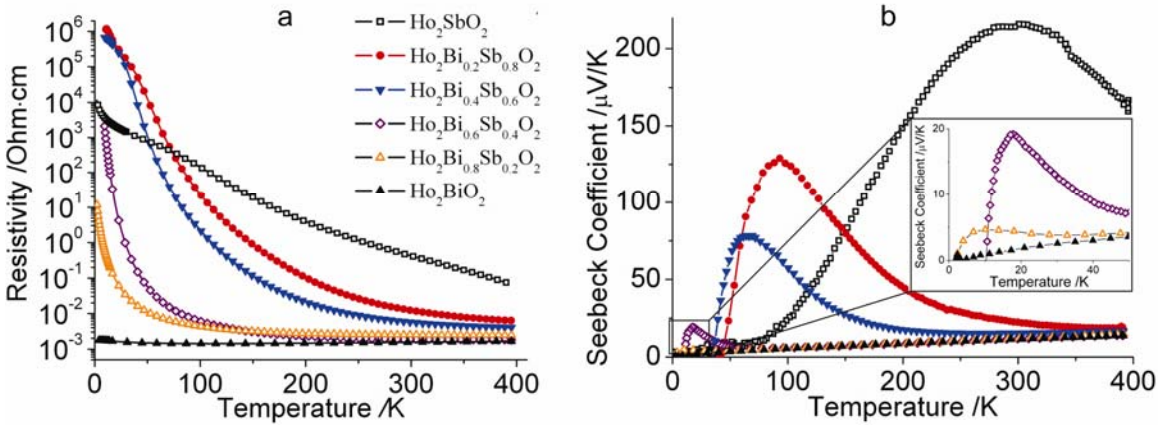

Figure 7.3. Electrical conductivities (a) and Seebeck coefficients (b) of the $Ho_2Sb_{1-x}Bi_xO_2$ compounds in the rage of 0–400K.

Such atomic localization within the Sb/Bi layer correlates nicely with the changes in the charge transport properties of the $Ho_2Sb_{1-x}Bi_xO_2$ samples. As shown in Figure 7.3, the room temperature electrical resistivity of these phases decreases about 400 folds from semiconducting in Ho_2SbO_2 to metallic in Ho_2BiO_2. Interestingly, all the Sb-containing samples possess a semiconductor-type behavior despite their increasing conductivity with respect to the Bi content. The effective band gap (activation energy), E_g, can be estimated

with Equation 7-1 from the maximum Seebeck coefficient, α_{max}, and its corresponding temperature, T_{max}.[24]

$$E_g - 2e\alpha_{\max}T_{\max} \tag{7-1}$$

Although such estimation may be more appropriate for classic semiconductors, it has to be noticed that the extracted effective bang gap (activation energy) displayed a trend similar to that of the Sb/Bi atomic disorder with respect to the increasing Bi concentration (Figure 7.5). Such diminishing, yet detectable activation energies (values listed in Table 7.6) in the $Ho_2Sb_{1-x}Bi_xO_2$ samples (except x =1) have a profound impact on their charge carrier transport properties.

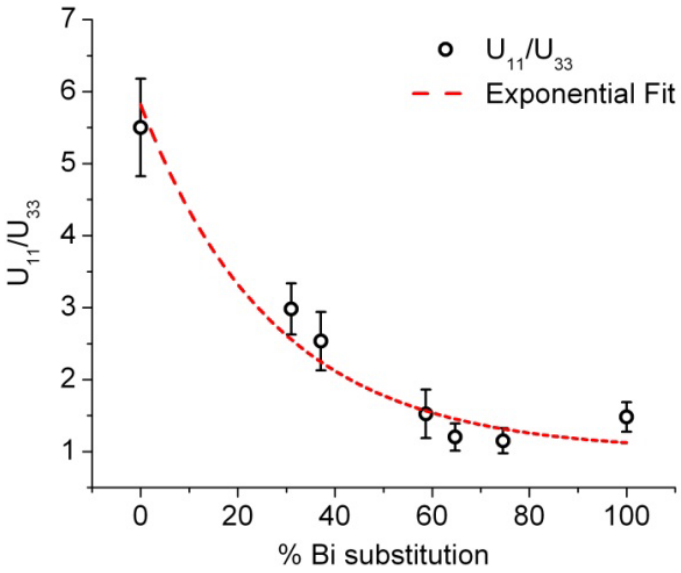

Figure 7.4. The value of U_{11}/U_{33} plotted against the percentage of Bi substitution. The data were fitted with an exponential decay function. Numerical data are listed in Table 3.

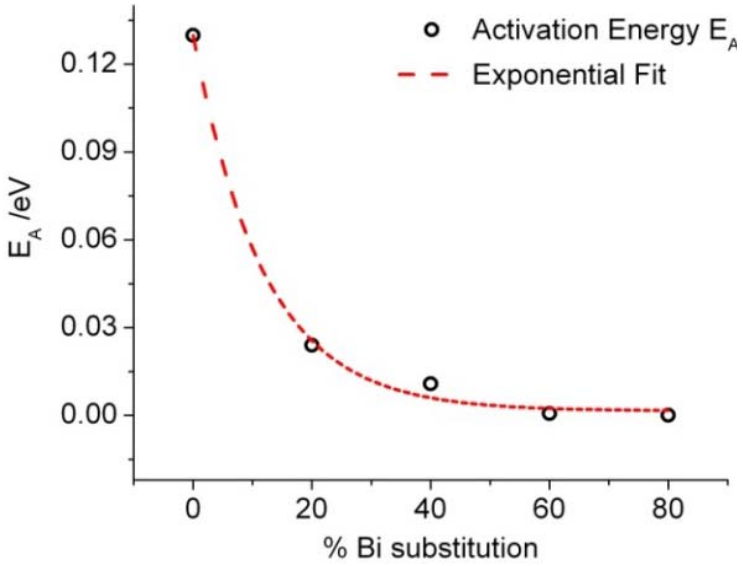

Figure 7.5. Estimated activation energies for the $Ho_2Sb_{1-x}Bi_xO_2$ bulk samples. The data were fitted with an exponential decay function. Numerical data are listed in Table 7.6.

Table 7.6. Room-temperature electrical resistivity and estimated activation energies of the $Ho_2Sb_{1-x}Bi_xO_2$ phases.

x	0	0.2	0.4	0.6	0.8	1
Resistivity at 298K /Ω·cm	5.0×10^{-1}	1.2×10^{-2}	6.1×10^{-3}	1.9×10^{-3}	2.5×10^{-3}	1.6×10^{-3}
Activation energy /eV	0.12	0.024	0.011	0.00068	0.000094	--

7.3.3 Electronic Structures

Since the classic band theory cannot explain the semiconducting properties of the RE_2SbO_2 and RE_2BiO_2 phases, [52, 105] the electrical behaviors observed in the $Ho_2Sb_{1-x}Bi_xO_2$ system cannot be simply attributed to the conventional band gap engineering based on elemental substitutions. Instead, the observed physical behaviors can be related to the degree of the atomic disorder within Sb/Bi layer, which dominates the electronic structure around the Fermi level. Based on the Anderson localization theory,[83] a significant atomic disorder, such as that in the RE_2SbO_2 phases, will lead to the

localization of states within some energy range (see Figure 7.6). According to Mott and Davis,[97] charge carriers can either tunnel within these localized states (variable-range hopping) or undergo thermal activation across the localized energy region, depending on the degree of randomness in the system and, thus, the energy span of localized states. Compared to the early-rare-earth analogs,[11] the starting member of the studied series, Ho_2SbO_2, already displays a reduced lattice disorder. Thus, a dominating charge carrier transport mechanism in Ho_2SbO_2 is thermal activation across the localized states. As indicated by the diffraction data, the Bi substitution further reduces the atomic disorder on pnictogen sites in the $Ho_2Sb_{1-x}Bi_xO_2$ series. Consequently, the energy range of the localized states (shaded region in Figure 7.6) decreases with increasing Bi content and disappears in Ho_2BiO_2. The experimentally observed changes in the electrical conductivity and activation energy can be seen as a physical manifestation of the diminishing atomic disorder and narrower localized states. Since it is easier to promote charge carriers across a smaller region of localized states, the low-temperature electrical conductivities of the $Ho_2Sb_{1-x}Bi_xO_2$ phases increase exponentially with the bismuth to antimony ratio. At high temperatures, the electrical conductivities of these compounds converge toward that of the metallic Ho_2BiO_2, as the total number of valence electrons does not change in the $Ho_2Sb_{1-x}Bi_xO_2$ series.

Likewise, the observed changes in their Seebeck coefficient can be also correlated to the Sb/Bi substitution and atomic localization within the Sb/Bi layer. The Seebeck coefficients of the $Ho_2Sb_{1-x}Bi_xO_2$ phases feature maxima representative of the activation of the secondary (compensating) charge carriers. As the energy region of localized states

narrows due to the local structure ordering (result of the increasing Bi substitution), the compensating charge carriers require less thermal energy to be promoted across the localized energy range. As a result, the maxima in the Seebeck coefficients are shifted to lower temperatures for the samples with a higher Bi content. At temperatures above those of the maximum Seebeck values, the thermopowers of the $Ho_2Sb_{1-x}Bi_xO_2$ phases were also found to converge toward that of the metallic Ho_2BiO_2. Such behavior implies the dominance of the metallic-type electronic structure above the localized states.

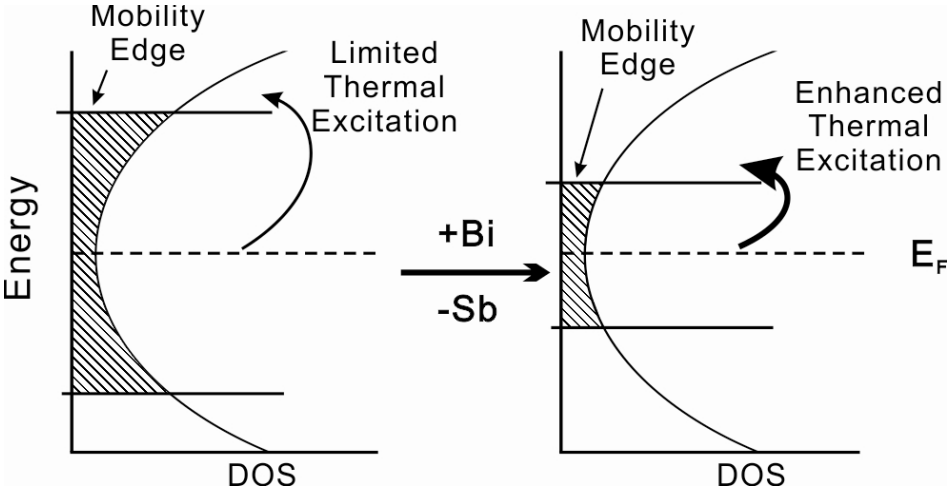

Figure 7.6. Schematic Density of States at the Fermi level for the Sb-containing samples. The shaded region represents the localized states. As the Bi concentration increases, the localized states become narrower and the thermal excitation of charge carriers is enhanced. The mobility edge is a boundary between the localized and extended states.

7.4 Conclusions

The $Ho_2Sb_{1-x}Bi_xO_2$ compositional series was traversed by varying the Sb:Bi ratio. While the modification on the average $Ho_2Sb_{1-x}Bi_xO_2$ structure is minimal, the lattice disorder caused by the pnictogen atomic displacement is reduced upon Bi substitution. As

a result, the energy range of Anderson-type localization within the Sb/Bi states diminishes. Since the Sb/Bi states dominated the electronic structure at the vicinity of the Fermi level, the electrical properties of the $Ho_2Sb_{1-x}Bi_xO_2$ phases were altered systematically within a large range. The focus of this work is not to explicate the detailed physics behind the observed physical properties, which may be due both to the Mott- and Anderson-type localization. Instead, we attempted to illustrate that the electrical properties of a disordered system can be tuned by controlling the degree of atomic localization. In a suitable system, such indirect physical property perturbation may be used in conjunction with other methods such as chemical doping and superlattice construction to produce tailor-made materials for future electronic and optical applications.

Chapter 8. Conclusions and Future Work

This dissertation illustrates the syntheses, structures and physical properties of a number of rare-earth antimonide suboxide phases with the following chemical compositions: RE_3SbO_3, $RE_8Sb_{3-\delta}O_8$, $RE_{9-\delta}Sb_5(O,C)_5$, $RE_9Sb_5O_4C$ and RE_2SbO_2 (*RE* = rare-earth elements). The author explores the interrelations between the chemistry, the structural features and the physical properties of the above mentioned compounds. As the driving force behind our studies, the thermoelectric properties of these phases are also investigated. Although most of these semiconducting compounds are not suitable for thermoelectric applications due to their low electrical conductivities, some of them may be potentially interesting for further material optimization. In addition to the experimental results and the associated theories summarized at the end of each chapter for the independent projects, by viewing the rare-earth antimonide suboxides as interrelated solid state systems, a number of important conclusions can be drawn for this type of materials.

8.1 The Structural Features

The structural versatility is, arguably, the most noticeable feature of the rare-earth antimonide suboxides. While the structural systems described in Chaper 3, 4 and 5 are distinctly different, all of them can be related by their common building blocks. For instance, the 3-D networks in the RE_3SbO_3/$RE_8Sb_{3-\delta}O_8$ system, the oxide layers in RE_2SbO_2, and the oxide/oxy-carbide sublattice in the $RE_{9-\delta}Sb_5(O,C)_5$/$RE_9Sb_5O_4C$ structures share the tetrahedral RE_4O units as common components. The origin of the

corner sharing RE_4O arrangement can be found in the structure of the RE_2O_3 oxides. Since all the electronegative oxygen atoms in these structures are surrounded by RE^{3+} cations, the Sb atoms could remain anionic as they are in the *RE*Sb binaries. To some extent, the rare-earth antimonide suboxide phases preserve the local structural features of their binary precursors, despite of their different overall structures.

8.2 Chemical Complexity and Flexibility

The structural interrelations between the rare-earth antimonide suboxides are reflected in the chemistry of the suboxides. Without carefully designed preparative experiments, the efforts of producing any one of these suboxides often would result in the formation of others as impurities. For example, the compositional and structural similarities between RE_3SbO_3 and $RE_8Sb_{3-\delta}O_8$ are reflected in their thermal stabilities and transformation pathways. Since the $RE_8Sb_{3-\delta}O_8$ suboxides are more thermodynamically stable, tuning the temperature and duration of the heat treatment allows selective preparation of either RE_3SbO_3 as the kinetic product or $RE_8Sb_{3-\delta}O_8$ as the thermodynamic product.

However, the most chemically complex systems within the rare-earth antimonide suboxide family would be the $RE_{9-\delta}Sb_5(O,C)_5$/$RE_9Sb_5O_4C$ superlattices described in Chapter 4. These phases are determined to be impurity stabilized through partial carbon substitution. And a number of interrelated structures were discovered by controlling the amount of carbon in the starting materials.

The least complex phases, RE_2SbO_2, display the chemical flexibility of the rare-earth antimonide suboxides. Owning to the robust chemistry, the RE_2SbO_2 phases are prepared for many rare-earth elements, so that the systematic changes in the electrical properties could be studied. In addition, chemical substitutions within the Sb layers are also proven feasible in Chapter 7.

8.3 The Physical Properties

Although the structures and chemistry of the rare-earth antimonide suboxides are interesting from a scientific perspective, the search for high performance thermoelectric phases is still the driving force behind our investigations. Within the scope of this dissertation, the $RE_{9-\delta}Sb_5(O,C)_5$/$RE_9Sb_5O_4C$ superlattices requires further preparative studies due to their chemical complexity, while the RE_3SbO_3/$RE_8Sb_3O_8$ and the RE_2SbO_2 compounds have been subjected to preliminary thermoelectric property studies. Although none of these phases appear to be desirable thermoelectric material at this stage, the $RE_8Sb_3O_8$ and RE_2SbO_2 phases are proven interesting for further investigations. It has to be noticed that the physical properties of these two types of compounds stemm from their local structural disorders and defects. As elucidated in Chapter 5, 6 and 7, perturbing the local structures of the Sb sites through chemical pressure (traversing the RE_2SbO_2 series), symmetry modification (tetragonal and orthorhombic Ho_2SbO_2) or direct chemical substitutions ($RE_2(Sb/Bi)O_2$ series), all results in a wide range of physical properties.

8.4 Expand the Natural Superlattice Structure

The conclusions about the rare-earth antimonide suboxides also give guidelines for the future investigations. First of all, a number of new phases can be predicted from the structural perspective. Since the $RE_{9-\delta}Sb_5(O,C)_5$/$RE_9Sb_5O_4C$ structures are the results of structure engineering, further exploration along this direction has led to the prediction and discovery of the $RE_{14}Sb_{10}O_4C$ phases. If one considers the general formula of the superlattice as $(RE_5Sb_5)_n(RE_4O_4C)$, where the integer n is the number of RE_5Sb_5 slabs between the neighboring RE_4O_4C layers, the $RE_9Sb_5O_4C$ phases satisfy n =1. Intuitively, the $RE_{14}Sb_{10}O_4C$ phases (or the equivalent oxide) can be constructed by stacking one RE_4O_4C layer with two slabs of RESb on each side (n = 2), while $RE_{19}Sb_{15}O_4C$ may form with lower oxide content (n = 3). Preliminary experimental results have indicated the existence of the $Dy_{14}Sb_{10}O_4C$ and $Ho_{14}Sb_{10}O_4C$ phases, whose X-ray powder diffraction patterns can be modeled by the predicted structure under the $P4/n$ space group. Similar to the studies shown in Chapter 4, further experiments are required to clarify the compositional ambiguities in these phases. In addition, single crystal X-ray diffraction studies would be necessary to confirm the structure. And ultimately, the physical property measurements have to be conducted on a series of $RE_{14}Sb_{10}O_4C$ phases and the corresponding $RE_9Sb_5O_4C$ phases in order to describe the impact of the stacking sequence on the physical properties of these natural superlattices.

8.5 Chemically Controlled Structural Alterations

The chemical flexibilities of the rare-earth antimonide suboxides imply that many more members of the compound family might be accessible by changing their compositions. The transformation from RE_3SbO_3 to $RE_8Sb_{3-\delta}O_8$ can be considered a chemical driven structural alteration. In an attempt to improve the electrical conductivity of the Ho_3SbO_3 phase by substituting Ho^{3+} with Ce^{4+}, a new structure is discovered. The $(CeHo)_3SbO_3$ phase adopts a novel crystal structure with the $P4_2/mnm$ space group. Similar to the original RE_3SbO_3 phases, the new tetragonal structure is composed of a framework of edge-sharing RE_4O tetrahedra with Sb atoms filling the empty channels. Since the Ce atoms are found to be in +3 oxidation state by subsequent magnetic studies, the driving force for the structural alteration is the sheer size difference between the two rare-earth elements. Intuitively, the larger La atom can also be mixed with the small Dy, Ho atoms to expand the iso-electronic compound series. Currently, a manuscript is being prepared to illustrate more details of the $(RE^{I}RE^{II})_3SbO_3$ phases, including atomic site preference of the *RE* atoms, the electronic structure calculations and the physical property measurements. Beyond the work in progress, the author is interested in probing the limit of rare-earth atomic size that would trigger the observed structural change. Experimentally, parallel syntheses using different large/small rare-earth pairs at different mixing ratios would be crucial in understanding the chemistry in these systems.

8.6 Improve the Thermoelectric Performances

Finally, the classic materials engineering approaches can also be used for future studies. The RE_2SbO_2 and $RE_8Sb_3O_8$ phases are narrow-band gap semiconductors with non-charge-balanced formulae. Their low electrical conductivity makes them inadequate for thermoelectric applications. However, doping these phases on both the *RE* site and the Sb site may dramatically improve their electrical conductivity, since the band gap of these phases are relatively small. Doping on the cationic site can be performed by adding 5% of Sr^{2+} or Zr^{4+} to form *p* and *n*-type extrinsic semiconductors, respectively. The elemental substitutions on the anionic Sb site with Sn (*p*-type) or Te (*n*-type) can be particularly interesting as the DOS at the vicinity of the Fermi level is dominated by the Sb *p*-orbitals.

As an extension of the study of the $RE_2(Sb/Bi)O_2$ system, the $Ho_2(Bi/Te)O_2$ phases can be prepared to modify the electrical properties. The Ho_2BiO_2 compound displays metallic properties[52] while the Ho_2TeO_2 compound is a charge-balanced semiconductor with a similar structure.[116, 117] Traversing the Te/Bi substitution can be considered as a classic example of modifying the charge carrier concentration to improve the thermoelectric properties. However, alterations of charge carrier propagation mechanisms may also take place as the Bi and Te atoms are randomly placed on the Bi atomic site.

Appendix

A1. Powder X-ray Diffraction Patterns

This section contains the powder X-ray diffraction patterns and Rietveld refinements of all the samples described in this thesis. The full-profile Rietveld refinement (Rietica program[63]) was used to refine the lattice constants and amount of impurities.

A1.1 $RE_3Sb_3O_3$ and $RE_8Sb_{3-\delta}O_8$

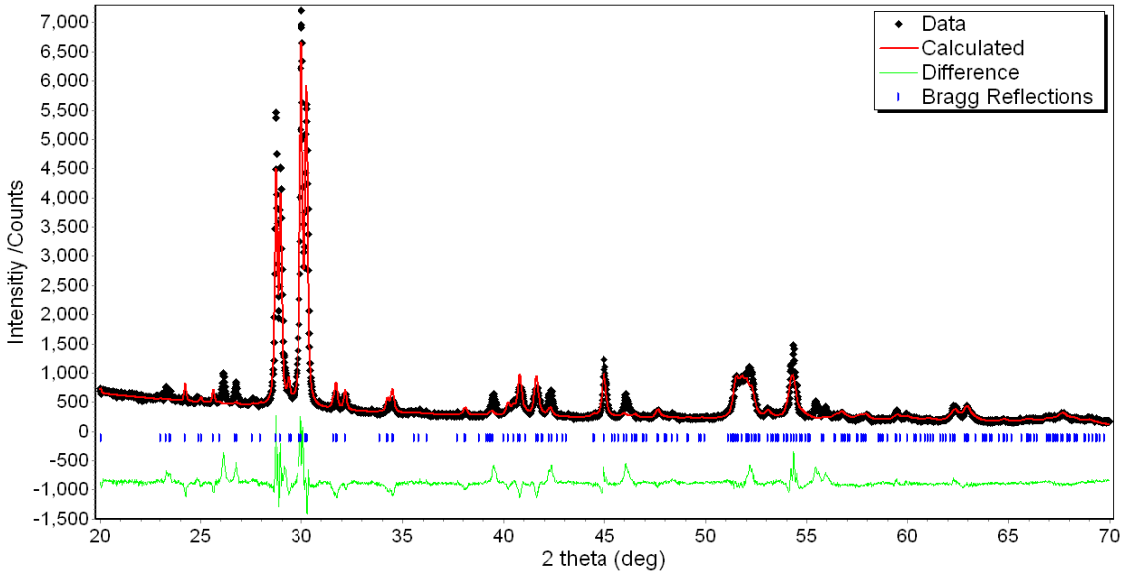

Figure A1-1. Powder X-ray diffraction patterns and Rietveld refinements of $La_8Sb_3O_8$.

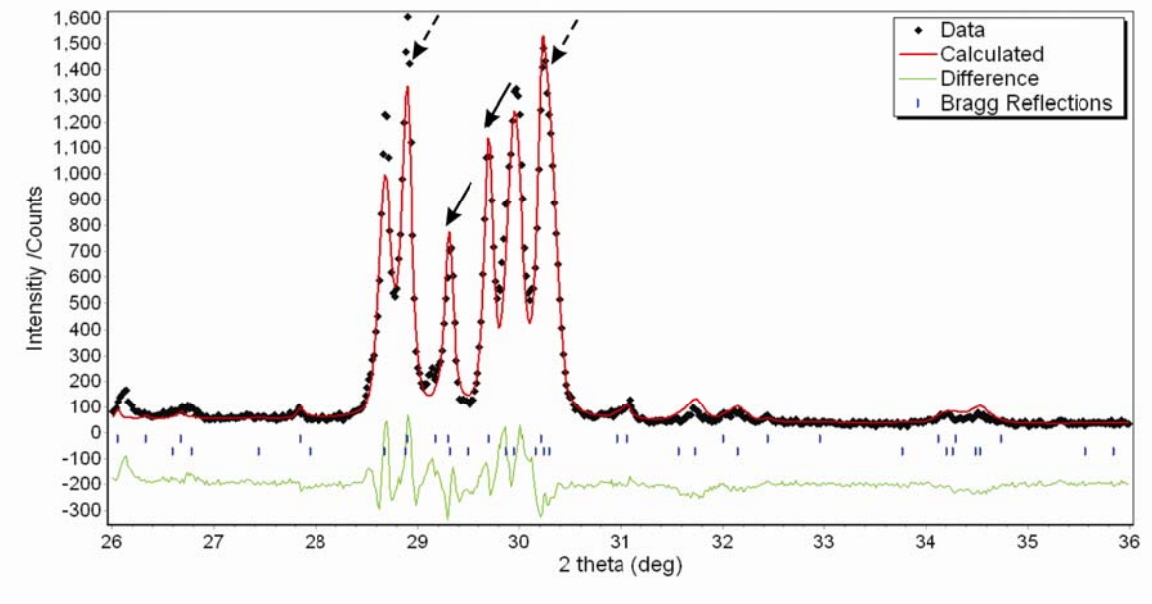

Figure A1-2. Powder X-ray diffraction patterns and Rietveld refinements of a mixture of La_3SbO_3 and $La_8Sb_3O_8$. The solid arrows marked the La_3SbO_3 peaks and the dashed arrows marked the overlapped peaks.

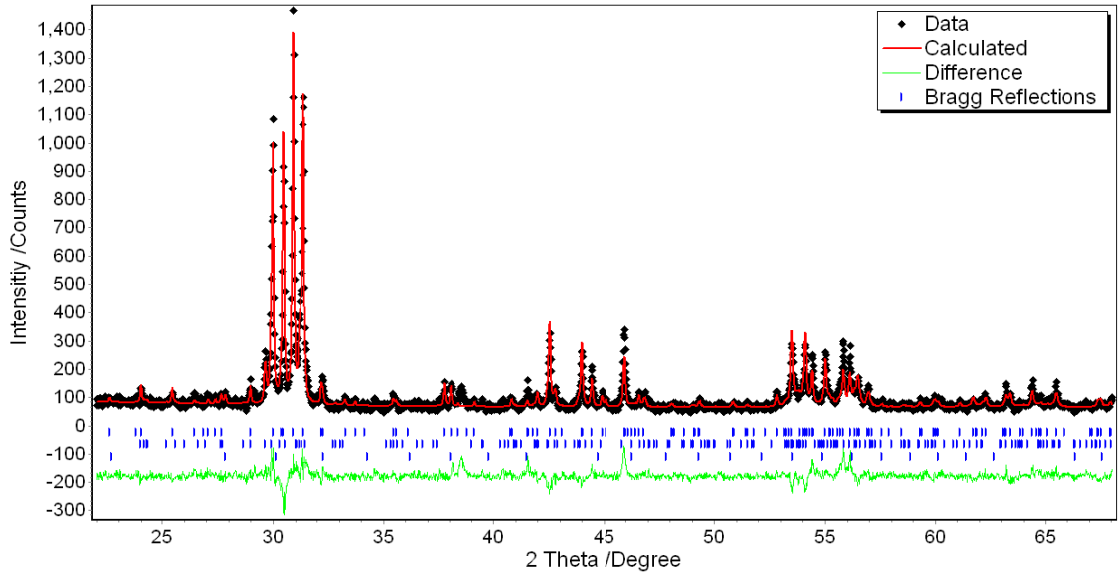

Figure A1-3. Powder X-ray diffraction patterns and Rietveld refinements of Sm_3SbO_3. The Bragg reflections of the three phases, including Sm_3SbO_3, $Sm_8Sb_3O_8$ and Sm_2O_3, were identified by the top, middle and bottom row of blue markers, respectively.

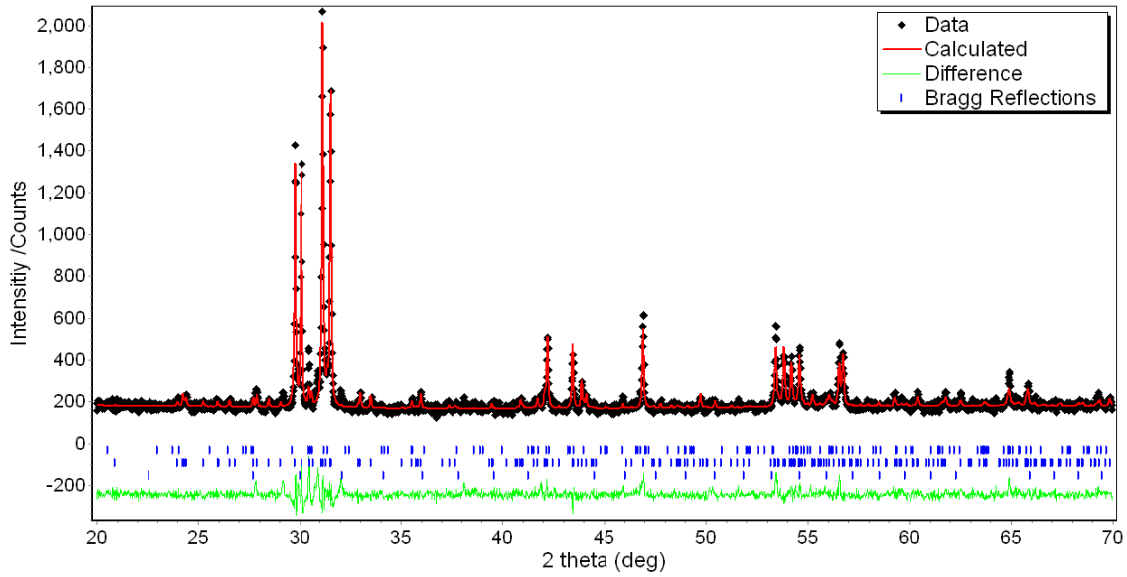

Figure A1-4. Powder X-ray diffraction patterns and Rietveld refinements of $Sm_8Sb_3O_8$. The Bragg reflections of the three phases, including Sm_3SbO_3, $Sm_8Sb_3O_8$ (major) and Sm_2O_3, were identified by the top, middle and bottom row of blue markers, respectively.

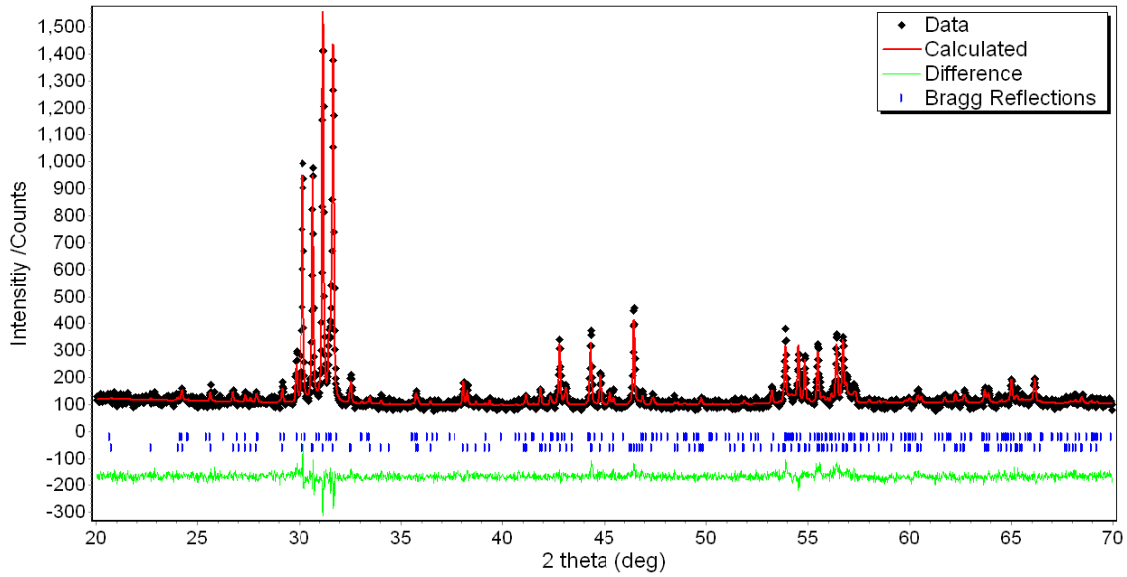

Figure A1-5. Powder X-ray diffraction patterns and Rietveld refinements of Gd_3SbO_3. The Bragg reflections of the three phases, including Gd_3SbO_3, $Gd_8Sb_3O_8$, were identified by the top, middle and bottom row of blue markers, respectively.

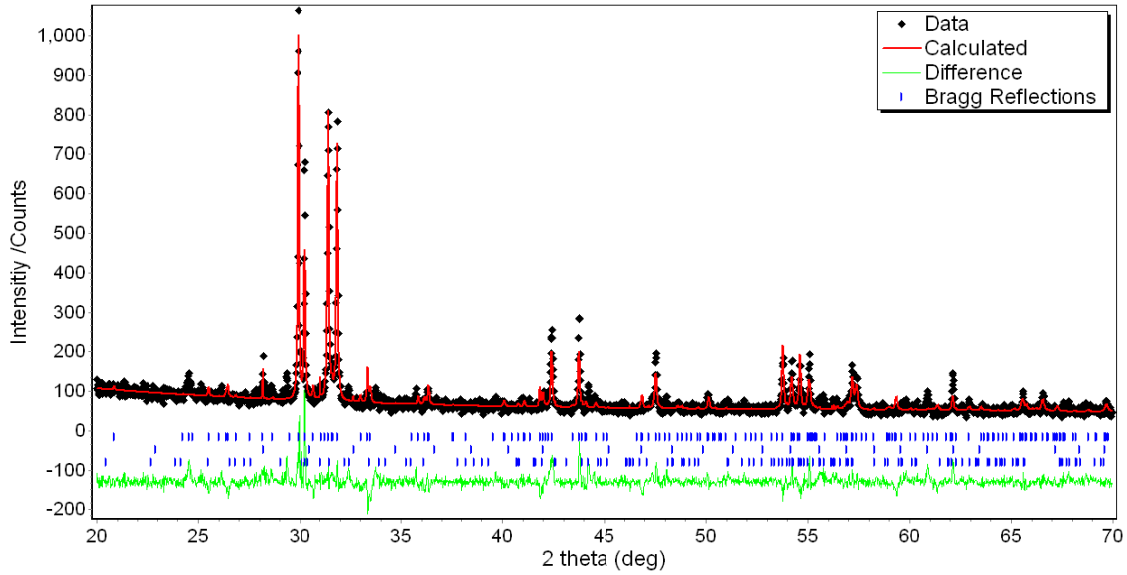

Figure A1-6. Powder X-ray diffraction patterns and Rietveld refinements of $Gd_8Sb_3O_8$. The Bragg reflections of the three phases, including $Gd_8Sb_3O_8$, GdSb, Gd_3SbO_3, were identified by the top, middle and bottom row of blue markers, respectively.

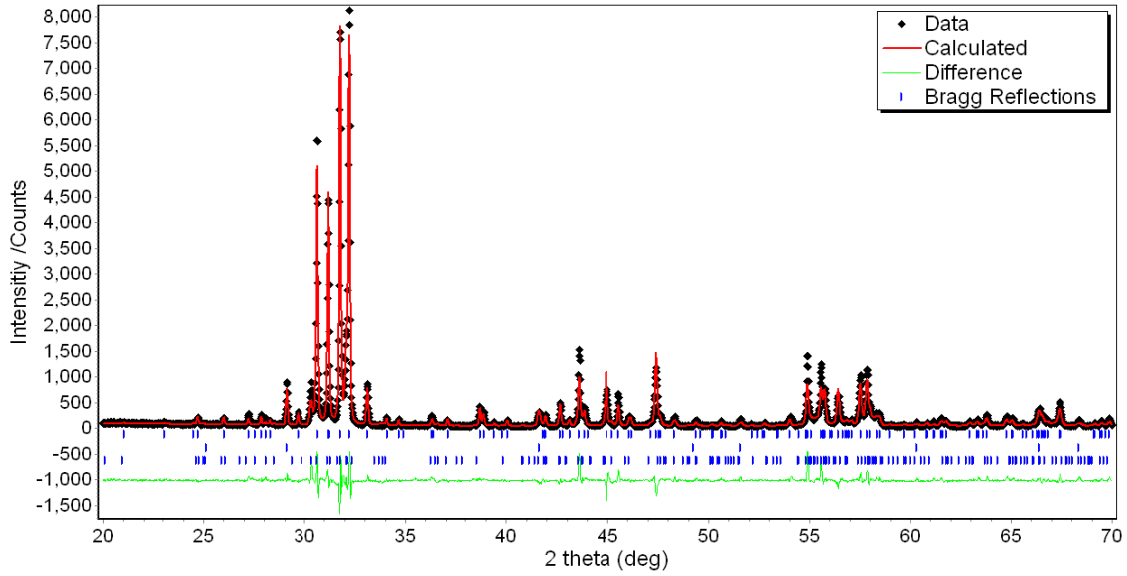

Figure A1-7. Powder X-ray diffraction patterns and Rietveld refinements of Ho_3SbO_3. The Bragg reflections of the three phases, including Ho_3SbO_3, HoSb, $Ho_8Sb_3O_8$, were identified by the top, middle and bottom row of blue markers, respectively.

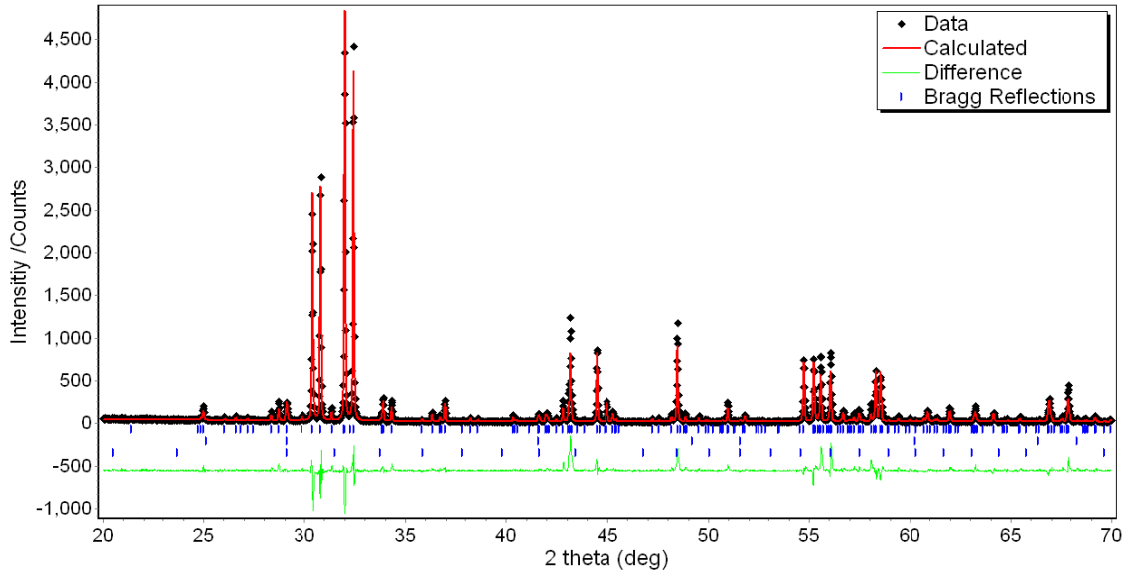

Figure A1-8. Powder X-ray diffraction patterns and Rietveld refinements of $Ho_8Sb_3O_8$. The Bragg reflections of the three phases, including Ho_3SbO_3, HoSb, Ho_2O_3, were identified by the top, middle and bottom row of blue markers, respectively.

A1.2 $RE_{9-\delta}Sb_5(O,C)_5$ and $RE_9Sb_5O_4C$

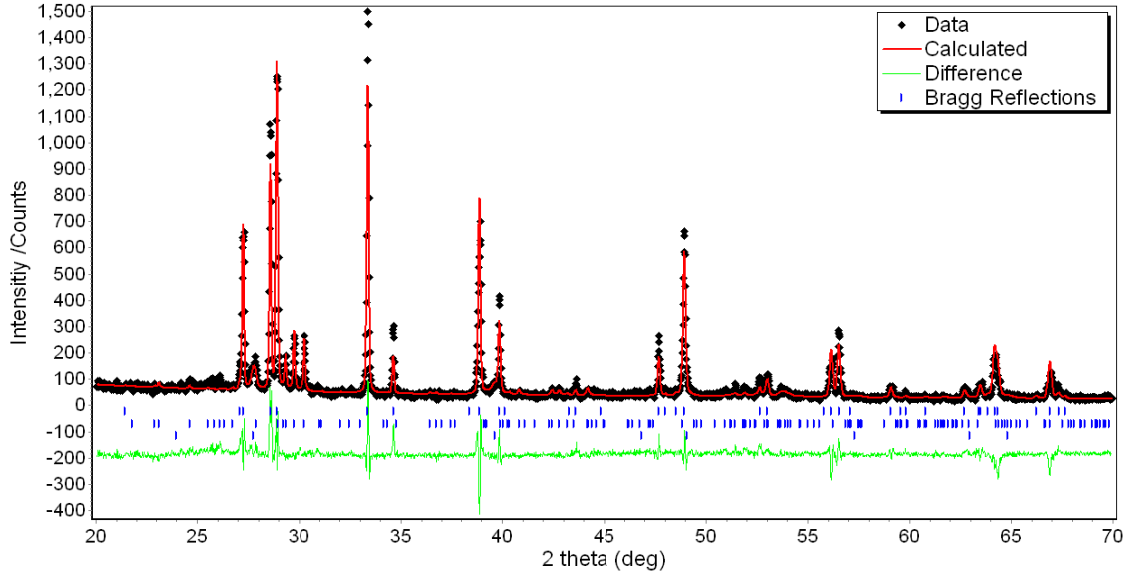

Figure A1-9. Powder X-ray diffraction patterns and Rietveld refinements of $La_{9-\delta}Sb_5(O,C)_5$. The Bragg reflections of the three phases, including $La_{9-\delta}Sb_5(O,C)_5$, La_3SbO_3, LaSb, were identified by the top, middle and bottom row of blue markers, respectively.

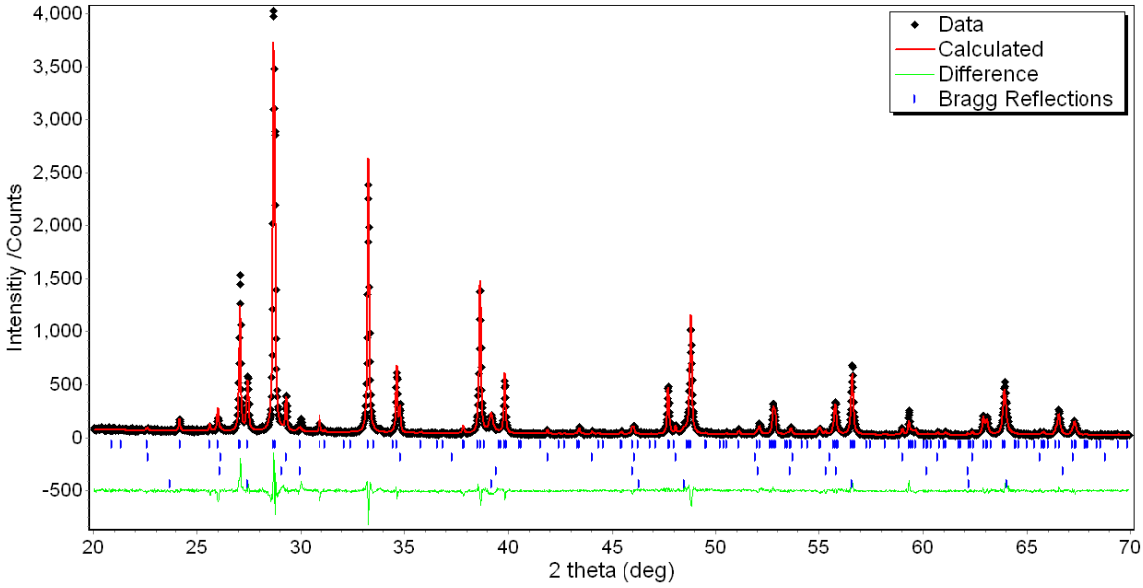

Figure A1-10. Powder X-ray diffraction patterns and Rietveld refinements of $La_9Sb_5O_4C$. The 4 rows of Bragg reflections markers indicated, $La_9Sb_5O_4C$, La_4Sb_3, La_2O_3 and LaSb, respectively.

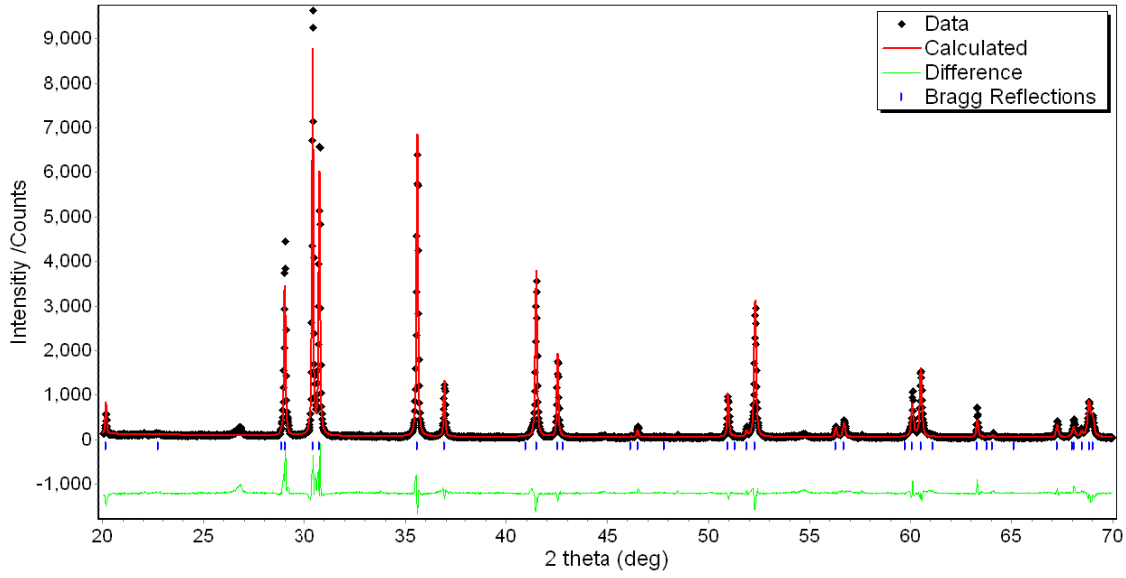

Figure A1-11. Powder X-ray diffraction patterns and Rietveld refinements of $Ho_{9-\delta}Sb_5(O,C)_5$.

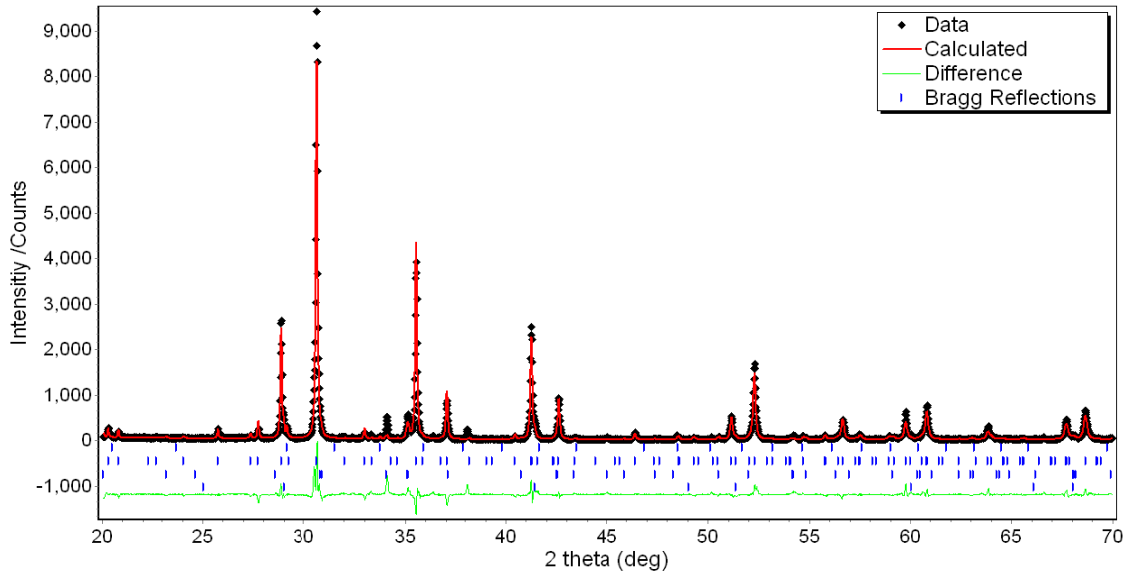

Figure A1-12. Powder X-ray diffraction patterns and Rietveld refinements of $Ho_9Sb_5O_4C$. The 4 rows of Bragg reflections markers indicated Ho_2O_3, $Ho_9Sb_5O_4C$, Ho_5Sb_3, and HoSb, respectively.

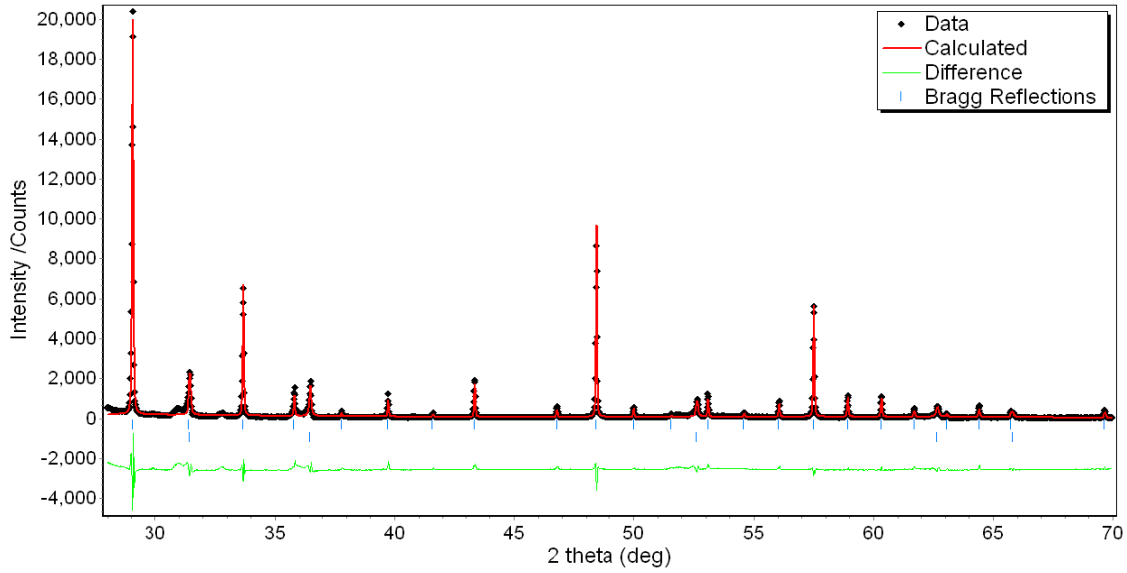

Figure A1-13. Powder X-ray diffraction patterns and Rietveld refinements of the Ho_4O_4C precursor. The top and bottom rows of Bragg reflections markers indicated a mixture of Ho_2O_3 (~75%) and a new phase with the HoN structure (~25%), respectively.

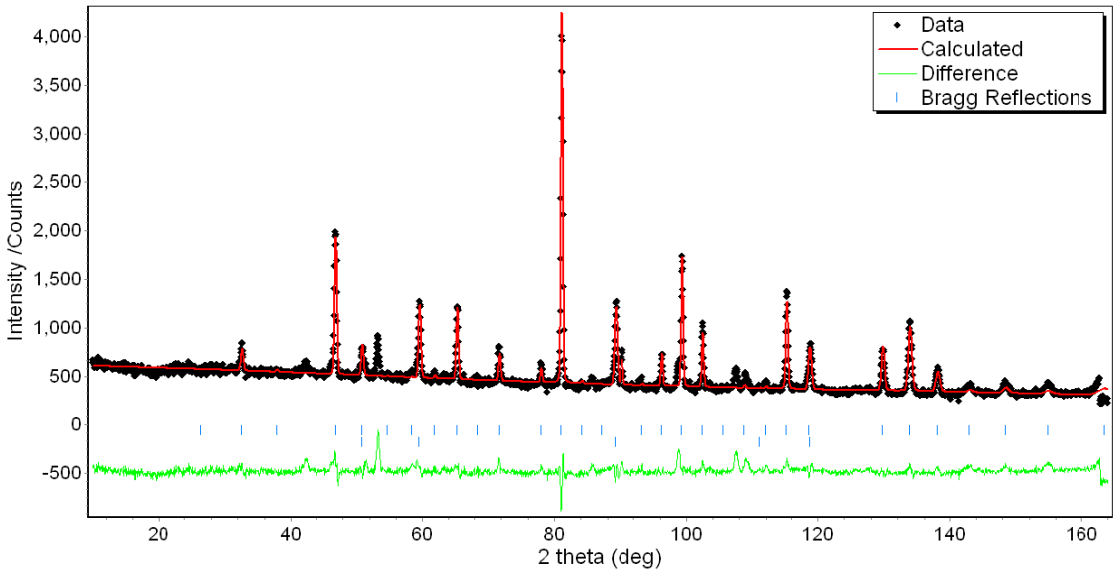

Figure A1-14. Powder Neutron diffraction patterns and Rietveld refinements of the Ho_4O_4C precursor. The top and bottom rows of Bragg reflections markers indicated a mixture of Ho_2O_3 (~75%) and a new phase with the HoN structure (~25%), respectively.

A1.3 RE_2SbO_2

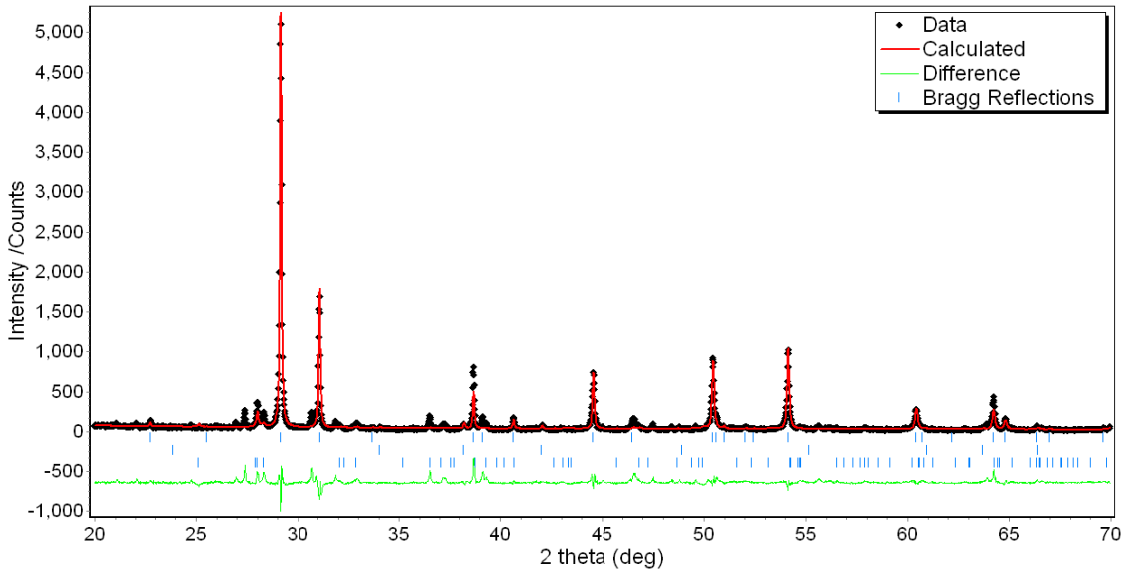

Figure A1-15. Powder X-ray diffraction patterns and Rietveld refinements of La_2SbO_2. The 3 rows of Bragg reflections markers indicated La_2SbO_2, Ta_3Sb and Sb_2O_3, respectively.

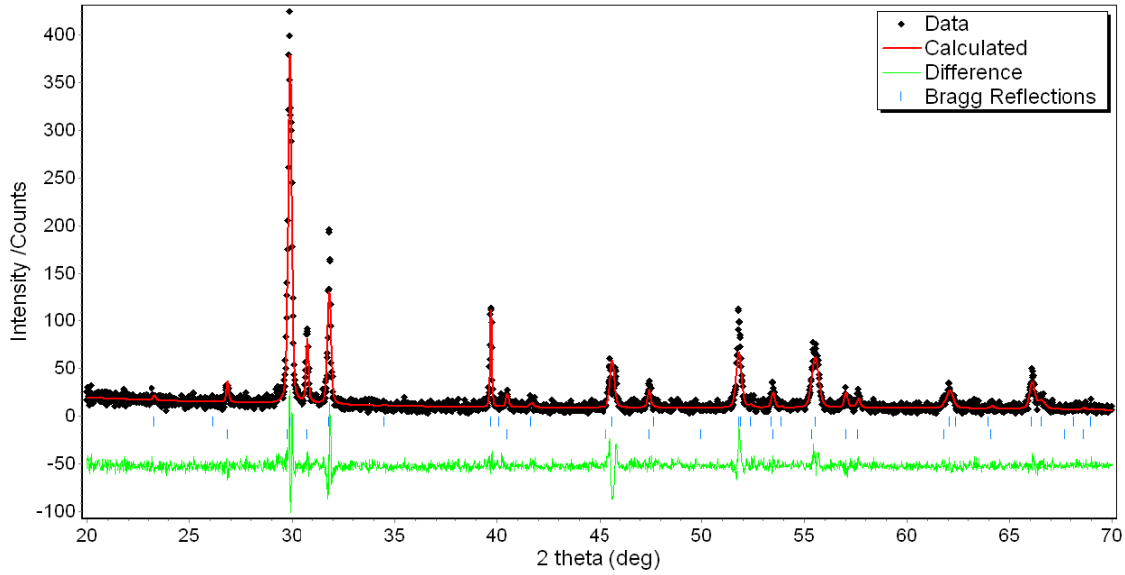

Figure A1-16. Powder X-ray diffraction patterns and Rietveld refinements of Nd_2SbO_2. The 2 rows of Bragg reflections markers indicated Nd_2SbO_2 and Nd_2O_3, respectively.

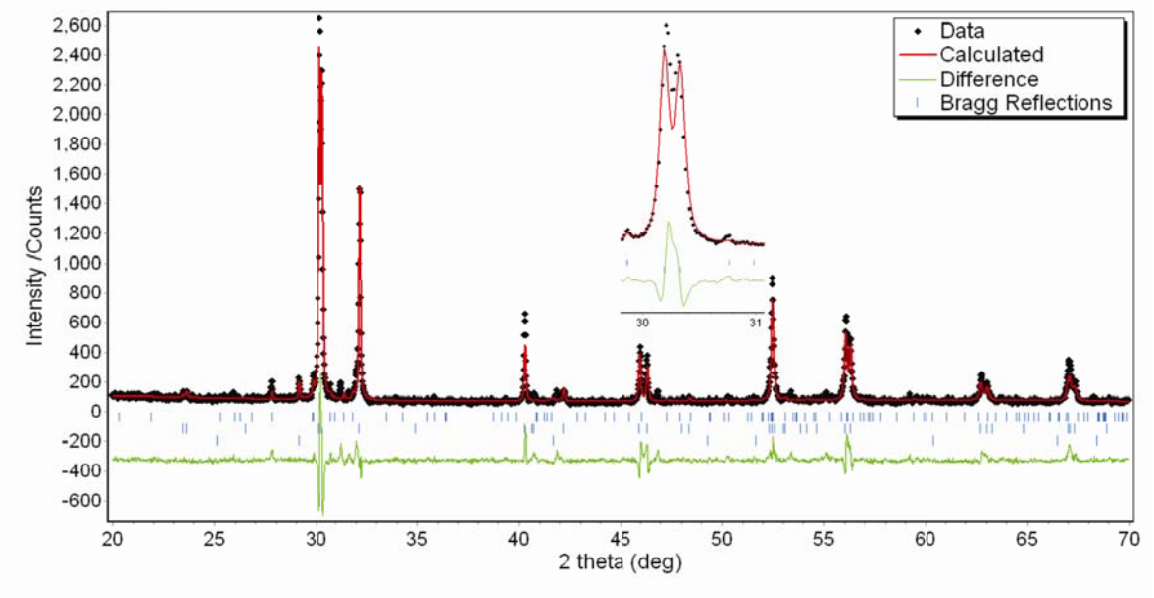

Figure A1-17. Powder X-ray diffraction patterns and Rietveld refinements of Sm_2SbO_2. The 3 rows of Bragg reflections markers indicated Sm_2O_3, Sm_2SbO_2 and SmSb respectively. The Sm_2SbO_2 structural model with *Immm* space group was used to describe the observed peak splitting.

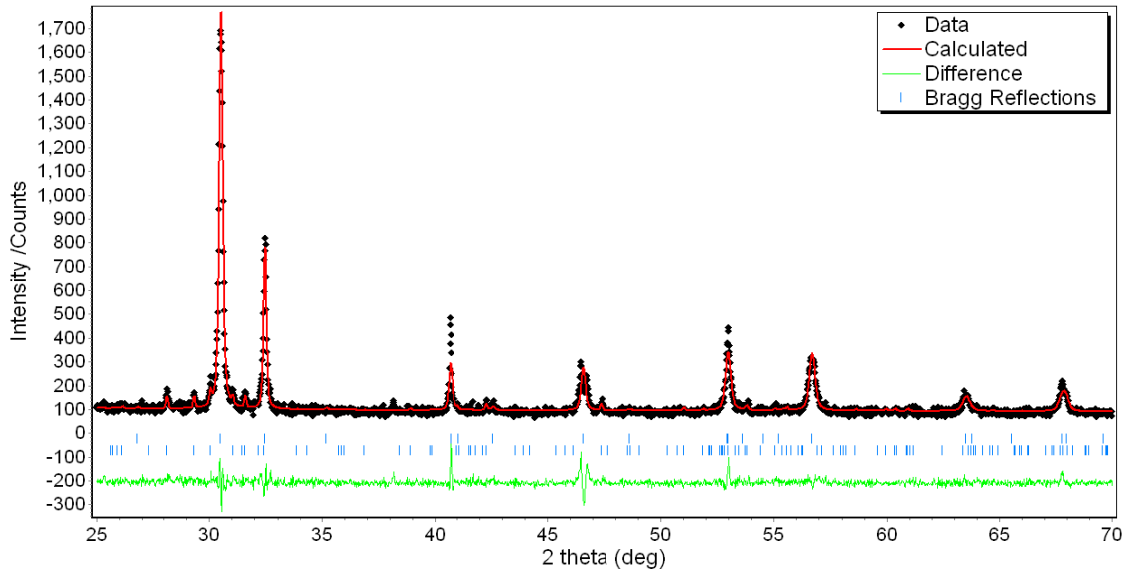

Figure A1-18. Powder X-ray diffraction patterns and Rietveld refinements of Gd_2SbO_2. The 2 rows of Bragg reflections markers indicated Gd_2SbO_2 and Gd_3O_4, respectively.

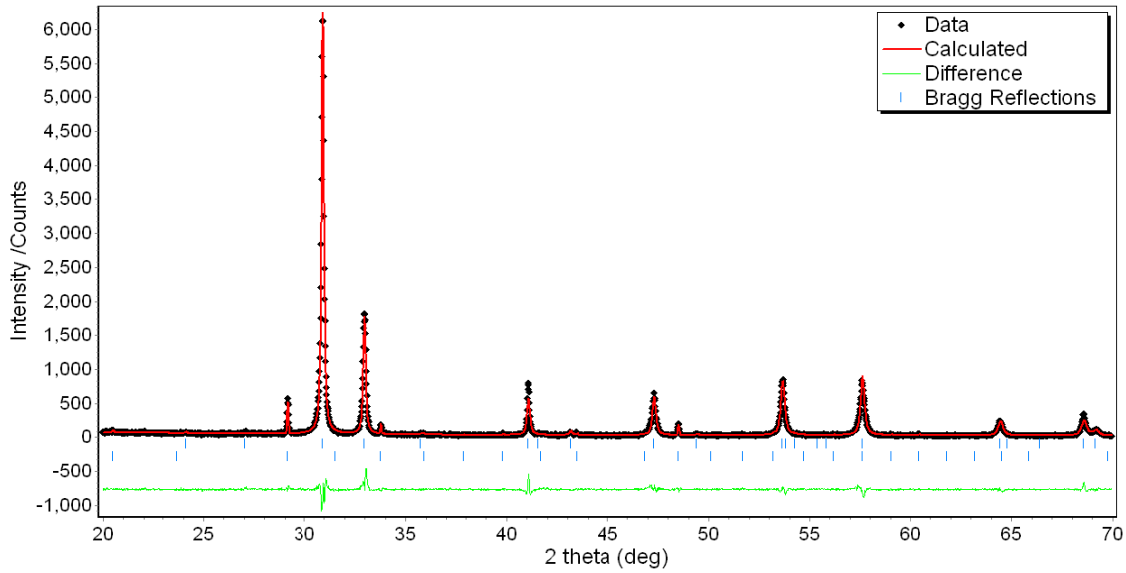

Figure A1-19. Powder X-ray diffraction patterns and Rietveld refinements of Ho_2SbO_2. The 2 rows of Bragg reflections markers indicated Ho_2SbO_2 and Ho_2O_3, respectively.

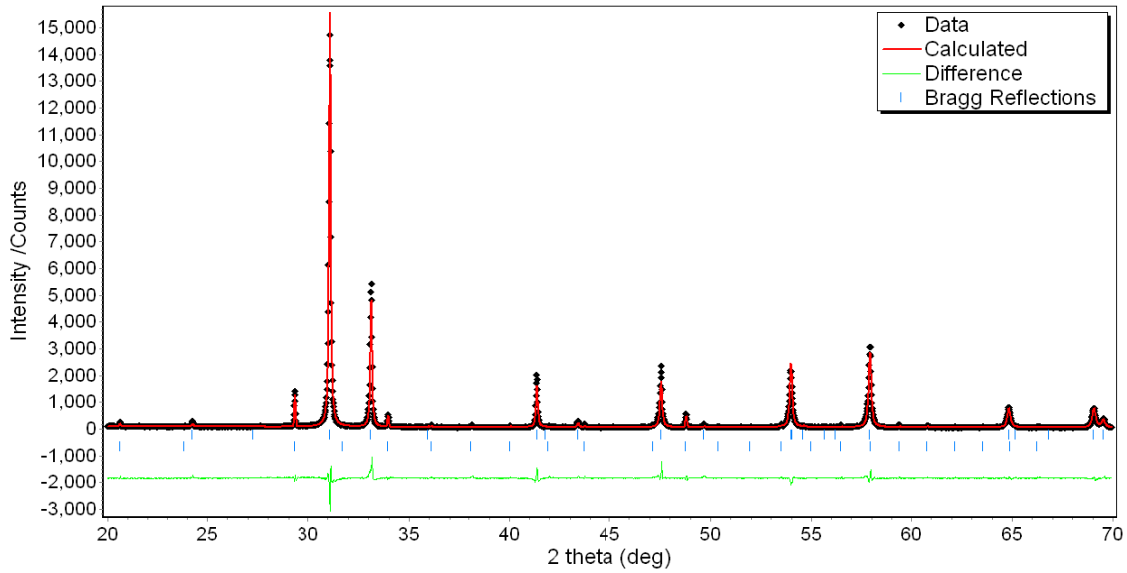

Figure A1-20. Powder X-ray diffraction patterns and Rietveld refinements of Er_2SbO_2. The 2 rows of Bragg reflections markers indicated Er_2SbO_2 and Er_2O_3, respectively.

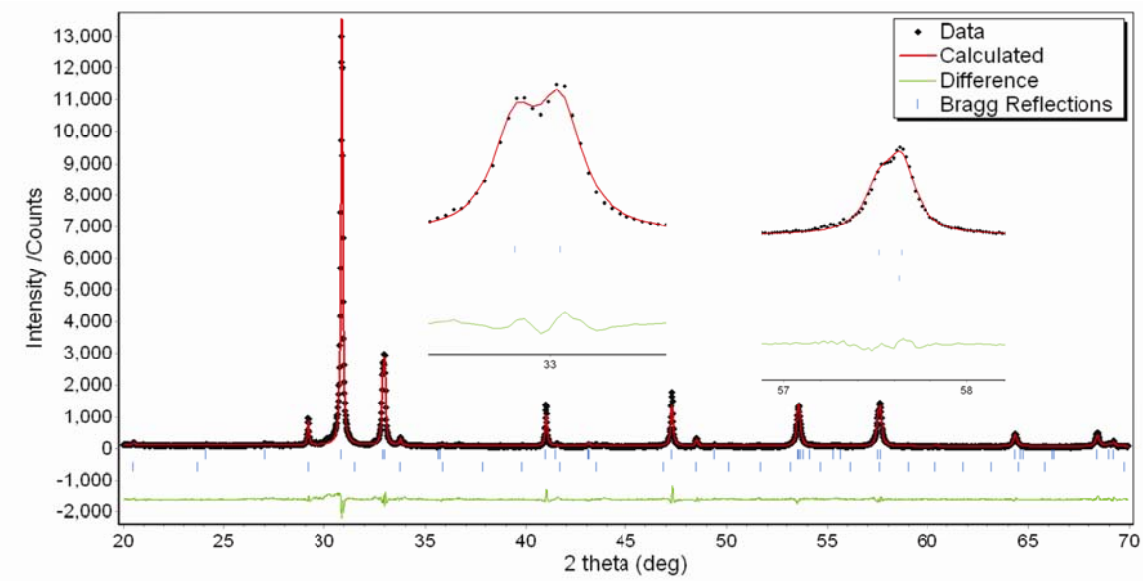

Figure A1-21. Powder X-ray diffraction patterns and Rietveld refinements of the low-symmetry Ho_2SbO_2. The 2 rows of Bragg reflections markers indicated Ho_2SbO_2 and Ho_2O_3, respectively. The Ho_2SbO_2 structural model with *Fmmm* space group was used for the refinement.

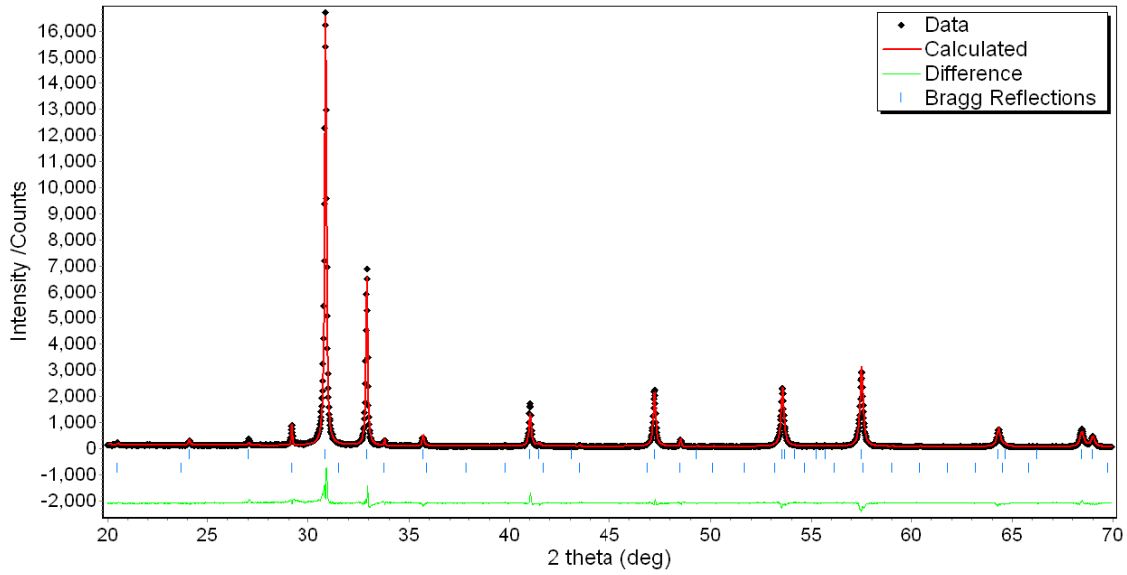

Figure A1-22. Powder X-ray diffraction patterns and Rietveld refinements of $Ho_2Sb_{0.4}Bi_{0.6}O_2$. The 2 rows of Bragg reflections markers indicated $Ho_2Sb_{0.4}Bi_{0.6}O_2$ and Ho_2O_3, respectively.

A2. Other Physical Property Data

This section included any physical property measurement data obtained but not discussed in the main text of this thesis.

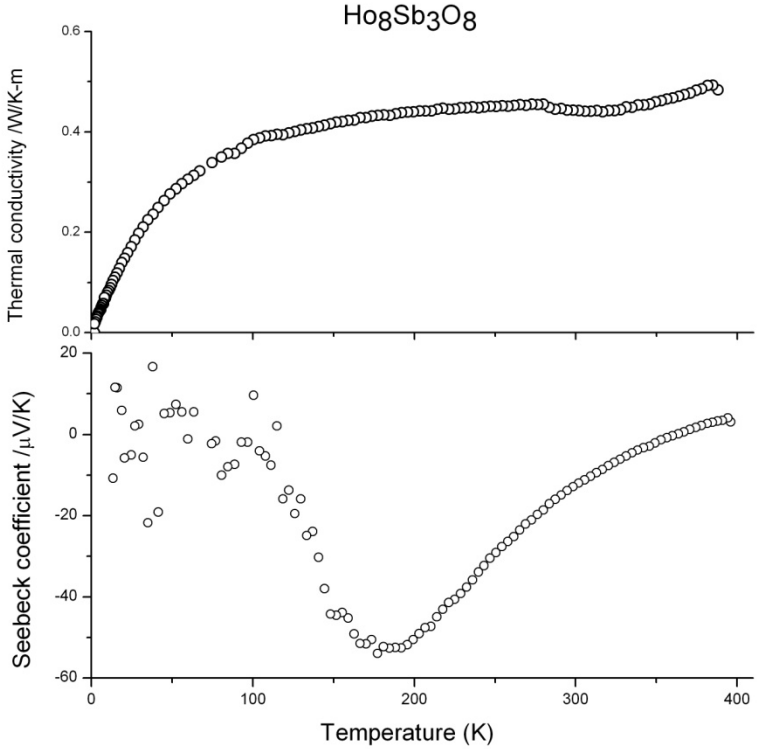

Figure A2-1. Thermal conductivity (top) and Seebeck coefficient (bottom) of the $Ho_8Sb_3O_8$ phase in the rage of 0–400K.

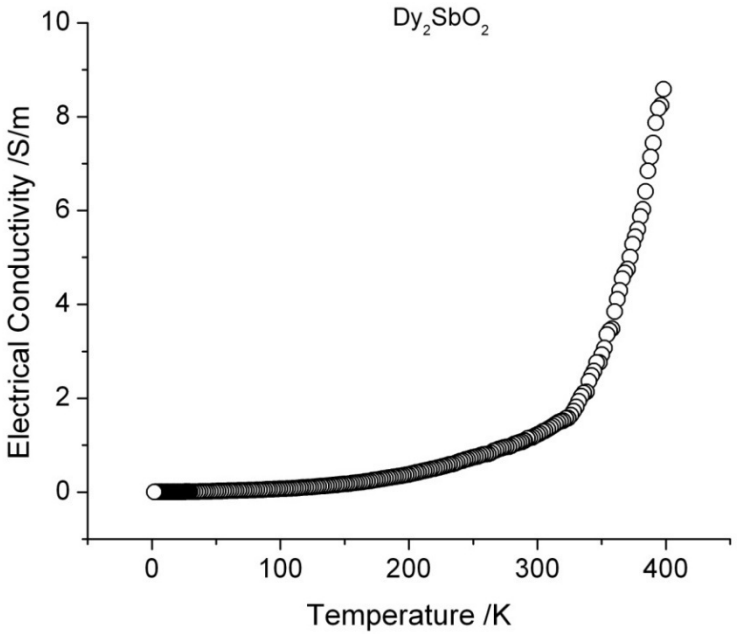

Figure A2-2. Electrical conductivity of the $Dy_8Sb_3O_8$ in the rage of 0–400K. The purity of the sample was less than atomic 90%.

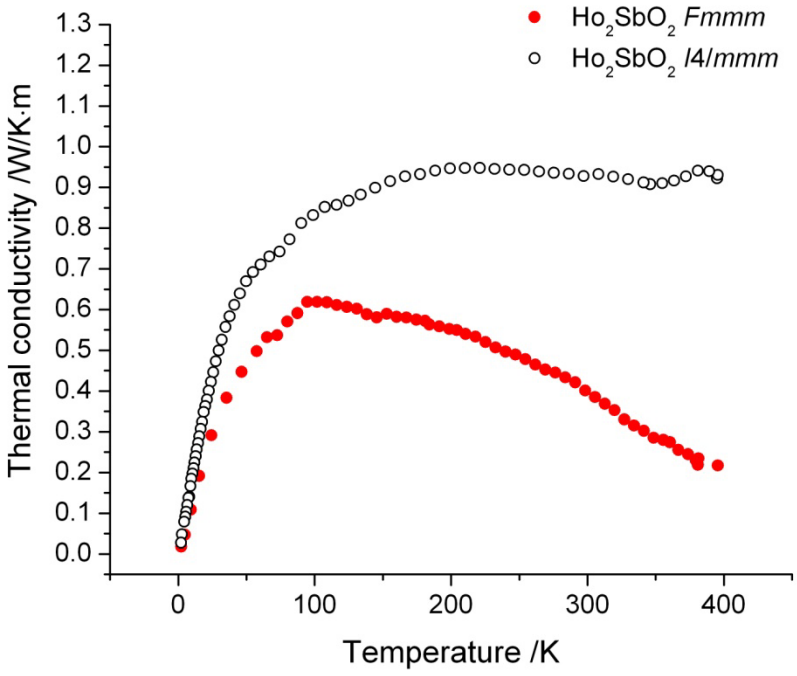

Figure A2-3. Thermal conductivities of the orthorhombic Ho_2SbO_2 phase (*Fmmm*) compare to that of its tetragonal counterpart (*I*4/*mmm*).

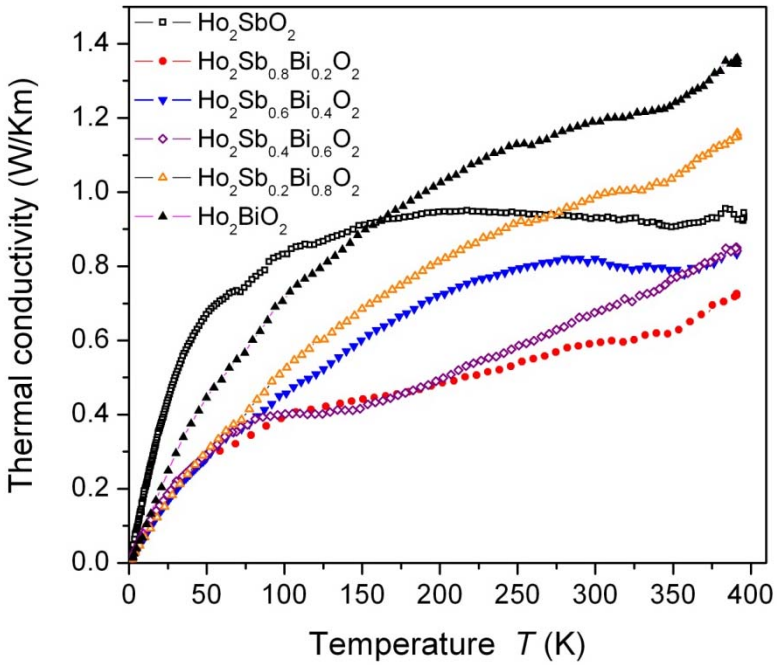

Figure A2-4. Thermal conductivities of the $Ho_2Sb_{1-x}Bi_xO_2$ compounds in the rage of 0–400K.

References

1. Tritt, T. M., *Science (Washington, D. C.)* **1996,** *272* (5266), 1276-1277.
2. F. J. Disalvo, *Science* **1999,** (285), 703.
3. Tritt, T. M.; Subramanian, M. A., *MRS Bulletin* **2006,** *31* (3), 188-194.
4. Sootsman, J. R.; Chung, D. Y.; Kanatzidis, M. G., *Angew. Chem.-Int. Edit.* **2009,** *48* (46), 8616-8639.
5. Seebeck, T. J., *Annalen der Physik* **1826,** *82* (2), 133-160.
6. Ioffe, A. F., *Semiconductor Thermoelements, and Thermoelectric Cooling*. Infosearch: London, U.K., 1957; p 184 pp.
7. Rowe, D. M., General Principles and Basic Considerations. In *Thermoelectrics Handbook --Macro to Nano*, Rowe, D. M., Ed. CRC press: Boca Raton, FL,, 2006; pp 1-8.
8. Pollock, D. D., General Principles and Theoretical Considerations. In *CRC Handb. Thermoelectr.*, Rowe, D. M., Ed. 1995.
9. Winder, E. J.; Ellis, A. B.; Lisensky, G. C., *J. Chem. Educ.* **1996,** *73* (10), 940.
10. Rowe, D. M., Introduction. In *CRC Handbook of Thermoelectrics*, Rowe, D. M., Ed. 1995; pp 1-5.
11. Sittig, M., *Thermoelectric materials*. Noyes Data Corp.: Park Ridge, N.J., 1970.
12. Luste, L. I. A. a. O. J., Modern Thermodynamic Theory of Thermoelectricity. In *Thermoelectrics Handbook --Macro to Nano*, Rowe, D. M., Ed. CRC press: Boca Raton, FL,, 2006.
13. Blatt, F. J.; et al., *Thermoelectric Power of Metals*. 1976; p 264 pp.
14. Altenkirch, E., *Phys. Z.* **1909,** *10*, 560-8.
15. Altenkirch, E.; Gehlhoff, G. Thermoelectric cooling and heating body. DE280696, 1911.
16. Goldsmid, H. J.; Douglas, R. W., *British Journal of Applied Physics* **1954,** *5* (11), 386.
17. Bennett, G. L.; Lombardo, J. J.; Hemler, R. J.; Silverman, G.; Whitmore, C. W.; Amos, W. R.; Johnson, E. W.; Zocher, R. W.; Hagan, J. C.; Englehart, R. W., *AIP Conf. Proc.* **2008,** *969* (Space Technology and Applications International Forum--STAIF 2008), 663-671.
18. Montag C. Davis, B. P. B., Peter T. Clarke, Brett R. Manners, and RobertM.Weymouth, Thermoelectric Refrigeration for Mass-Market Applications. In *Thermoelectrics Handbook --Macro to Nano*, Rowe, D. M., Ed. CRC press: Boca Raton, FL,, 2006.
19. Stabler, F. R., *Mater. Res. Soc. Symp. Proc.* **2006,** *886* (Materials and Technologies for Direct Thermal-to-Electric Energy Conversion), 13-21.
20. Yang, J.; Caillat, T., *MRS bulletin* **2006,** *31* (03), 224-229.
21. Vining, C. B., *Nat. Mater.* **2009,** *8* (2), 83-85.
22. Slack, G. A., New materials and performance limits for thermoelectric cooling. In *CRC Handb. Thermoelectr.*, Rowe, D. M., Ed. 1995.

23. MacDonald, D. K. C., *Thermoelectricity: An Introduction to the Principles.* John Wiley & Sons, Inc.: New York, 1962.
24. Goldsmid, H.; Sharp, J., *J. Electron. Mater.* **1999,** *28* (7), 869-872.
25. Snyder, G. J.; Toberer, E. S., *Nat. Mater.* **2008,** *7* (2), 105-114.
26. Jonson, M.; Mahan, G. D., *Phys. Rev. B* **1980,** *21* (10), 4223-4229.
27. White, M. A., *Properties of Materials*. Oxford University Press: New York, 1999.
28. Keyes, R. W., *Phys. Rev.* **1959,** *115* (3), 564-567.
29. Mahan, G. D.; Sofo, J. O., *Proc. Natl. Acad. Sci. U. S. A.* **1996,** *93* (15), 7436-7439.
30. Nolas, G. S.; Poon, J.; Kanatzidis, M., *MRS Bulletin* **2006,** *31* (3), 199-205.
31. Kleinke, H., *Chem. Mater.* **2009,** *22* (3), 604–611.
32. Beekman, M.; Nolas, G. S., *J. Mater. Chem.* **2008,** *18* (8), 842-851.
33. Snyder, G. J.; Christensen, M.; Nishibori, E.; Caillat, T.; Iversen, B. B., *Nat. Mater.* **2004,** *3* (7), 458-463.
34. Toberer, E. S.; Sasaki, K. A.; Chisholm, C. R. I.; Haile, S. M.; Goddard, W. A.; Snyder, G. J., *physica status solidi (RRL) – Rapid Research Letters* **2007,** *1* (6), 253-255.
35. Koumoto, K.; Terasaki, I.; Funahashi, R., *MRS Bulletin* **2006,** *31* (3), 206-210.
36. Gascoin, F.; Ottensmann, S.; Stark, D.; Haile, S. M.; Snyder, G. J., *Adv. Funct. Mater.* **2005,** *15* (11), 1860-1864.
37. Peter Atkins, T. O., Jonathan Rourke, Mark Weller, Fraser Armstrong, *Inorganic Chemistry*. 4th ed.; W.H. Freeman & Company New York, U.S., 2006.
38. Abdusalyamova, M. N.; Shokirov, H. S.; Rakhmatov, O. I., *J. Less-Common Met* **1990,** *166* (2), 221-7.
39. Li, D. X.; Haga, Y.; Shida, H.; Suzuki, T.; Kwon, Y. S., *Phys. Rev. B* **1996,** *54* (15), 10483-10491.
40. Larson, P.; Lambrecht, W. R. L., *Phys. Rev. B* **2006,** *74* (8).
41. Nolas, G. S.; Cohn, J. L.; Chakoumakos, B. C.; Slack, G. A., *Therm. Conduct.* **2000,** *25* (Thermal Expansion 13), 122-129.
42. Gaume, R.; Viana, B.; Vivien, D.; Roger, J.-P.; Fournier, D., *Appl. Phys. Lett.* **2003,** *83* (7), 1355-1357.
43. Fennell, T.; Bramwell, S. T.; Green, M. A., *Can. J. Phys.* **2001,** *79* (11/12), 1415-1419.
44. Hinatsu, Y.; Ebisawa, H.; Doi, Y., *J. Solid State Chem.* **2009,** *182* (7), 1694-1699.
45. Marcano, C. M.; Rasines, I., *Inorg. Chim. Acta* **1985,** *109* (2), L15-L16.
46. Lissner, F.; Meyer, M.; Kremer, R. K.; Schleid, T., *Z. Anorg. Allg. Chem.* **2006,** *632* (12-13), 1995-2002.
47. Lissner, F.; Schleid, T., *Z. Anorg. Allg. Chem.* **1993,** *619* (10), 1771-6.
48. Schleid, T., *Eur. J. Solid State Inorg. Chem.* **1996,** *33* (2/3), 227-40.
49. Nuss, J.; von Schnering, H. G.; Grin, Y., *Z. Anorg. Allg. Chem.* **2004,** *630* (13-14), 2287-2291.
50. Nuss, J.; Jansen, M., *Z Kristallogr New Cryst Struct* **2002,** *217* (1), 19-20.
51. Nuss, J.; Jansen, M., *Acta Crystallogr B* **2007,** *B63* (6), 843-849.
52. Mizoguchi, H.; Hosono, H., *J. Am. Chem. Soc.* **2011,** *133* (8), 2394-2397.

53. Benz, B., *Acta Crystallogr B* **1971,** *27* (Pt. 4), 853-4.
54. Nuss, J.; Jansen, M., *J. Alloys Compd.* **2009,** *480* (1), 57-59.
55. Corbett, J. D., *Inorg. Chem.* **2009,** *49* (1), 13-28.
56. Adachi, G.; Imanaka, N.; Kang, Z. C., *Binary Rare Earth Oxides*. Springer: 2004.
57. Furuseth, S.; Selte, K.; Kjekshus, A., *Acta Chem. Scand.* **1965,** *19* (1), 95-106.
58. Pecharsky, V.; Zavaliji, P., *Fundamentals of Powder Diffraction and Structural Characterization of Materials*. Springer-Verlag: 2003; p 744 pp.
59. Palmer, M. F. C. L. a., *Structure Determination by X-ray Crystallography*. 3rd ed.; Pleum Press: New York, 1993.
60. STOE; Cie; STOE & Cie GmbH: Darmstadt, G., 2004.
61. *Bruker Analytical X-Ray Systems*, Madison, WI, USA, 2002.
62. Sheldrick, G. M.; Schneider, T. R., *Methods Enzymol.* **1997,** *277*, 319-43.
63. Hunter, B. A. H., C. J.;, *Australian Nuclear Science and Technology Organization: Menai, Australia* **2000**.
64. Egerton, R. F., *Physical Principles of Electron Microscopy: an Introduction to TEM, SEM, And AEM.* Springer Science+Business Media: New York, 2005.
65. Andersen, O. K.; Pawlowska, Z.; Jepsen, O., *Phys. Rev. B* **1986,** *34* (8, Pt. 1), 5253-69.
66. O. Jepsen, A. B., O. K. Andersen *The TB-LMTO-ASA Program*, version 4.7; Max-Planck-Institut für Festkörperforschung: Stuttgart, Germany 1999.
67. Andersen, O. K.; Jepsen, O., *Phys. Rev. Lett.* **1984,** *53* (27), 2571-4.
68. O. K. Andersen O. Jepsen, D. G., In *Highlights of condensed matter theory*, F. Bassani, F. F., M. Tosi (eds), Ed. North−Holland, Lambrecht, W. R. L: New York, 1985.
69. Jepsen, O.; Andersen, O. K., *Z. Phys. B: Condens. Matter* **1995,** *97* (1), 35-47.
70. H. Scherrer, S. S., Thermoelecrtric Properties of Bismuth Antimony Telluride Solid Solution. In *Thermoelectrics Handbook --Macro to Nano*, Rowe, D. M., Ed. CRC press: Boca Raton, FL,, 2006; pp 27-1.
71. Satterthwaite, C. B.; Ure, R. W., Jr., *Phys. Rev.* **1957,** *108*, 1164-70.
72. Brown, S. R.; Kauzlarich, S. M.; Gascoin, F.; Snyder, G. J., *Chem. Mater.* **2006,** *18* (7), 1873-1877.
73. Mozharivskyj, Y.; Pecharsky, A. O.; Bud'ko, S.; Miller, G. J., *Chem. Mater.* **2004,** *16* (8), 1580-1589.
74. Nylen, J.; Andersson, M.; Lidin, S.; Haeussermann, U., *J. Am. Chem. Soc.* **2004,** *126* (50), 16306-16307.
75. Nuss, J.; Jansen, M., *Z Kristallogr New Cryst Struct* **2009,** *224* (1), 11-12.
76. Kolodiazhnyi, T.; Petric, A., *J. Am. Ceram. Soc.* **2003,** *86* (9), 1554-1559.
77. Sarbak, Z., *Binary Rare Earth Oxides edited by G. Adachi, N. Imanaka, and Z. C. Kang*. 2005; Vol. 84, p 963.
78. Hoenle, W.; Von Schnering, H. G., *Z. Kristallogr.* **1981,** *155* (3-4), 307-14.
79. Kleinke, H., *Inorg. Chem.* **1999,** *38* (12), 2931-2935.
80. Xu, J.; Kleinke, H., *J. Comput. Chem.* **2008,** *29* (13), 2134-2143.
81. Hamilton, W. C., *Acta. Cryst.* **1965,** *18* (3), 502-10.

82. Caillat, T.; Fleurial, J. P.; Borshchevsky, A., *J. Phys. Chem. Solids* **1997,** *58* (7), 1119-1125.
83. Anderson, P. W., *Phys. Rev.* **1958,** *109*, 1492-1505.
84. Kramer, B., Springer Proceedings in Physics. In *Springer Proc. Phys.*, T.Ando and H.Fukuyama, S.-V., Berlin, Ed. Springer-Verlag: Berlin - New York 1988; Vol. 28, p p84.
85. Cox, P. A., *The Electronic Structure and Chemistry of Solids*. 1987; p 350 pp.
86. P.Ganguly, C. N. R. a., In *Localization and Metal - Insulator Transition*, D.Adler, H. F. a., Ed. Plenum Press: New York - London 1985; p p53.
87. Jones, D. W.; McColm, I. J.; Yerkess, J., *J. Solid State Chem.* **1991,** *92* (2), 301-11.
88. Jones, D. W.; McColm, I. J.; Steadman, R.; Yerkess, J., *J. Solid State Chem.* **1984,** *53* (3), 376-81.
89. Brown, I. D.; Altermatt, D., *Acta Crystallogr A* **1984,** *40*, C444-C445.
90. Atoji, M., *J. Chem. Phys.* **1981,** *74*.
91. Brese, N. E.; O'Keeffe, M., *Acta Crystallogr B* **1991,** *47* (2), 192-197.
92. Fort, D.; Pecharsky, V. K.; Gschneidner, K. A., *J. Alloys Compd.* **1995,** *226* (1-2), 190-196.
93. Dan'kov, S. Y.; Tishin, A. M.; Pecharsky, V. K.; Gschneidner, K. A., *Phys. Rev. B* **1998,** *57* (6), 3478-3490.
94. Leon-Escamilla, E. A.; Corbett, J. D., *Chem. Mater.* **2006,** *18* (20), 4782-4792.
95. Papoian, G. A.; Hoffmann, R., *Angew. Chem.-Int. Edit.* **2000,** *39* (14), 2409-2448.
96. Shannon, R., *Acta Crystallogr. Sect. A* **1976,** *32* (5), 751-767.
97. Mott, N.; Davis, E. A., *International Series of Monographs on Physics. Electronic Processes in Non-Crystalline Materials*. Oxford Univ. Press: 1978.
98. Mott, N. F., *Philos. Mag.* **1972,** *26* (4), 1015 - 1026.
99. Hill, R. M., *Physica Status Solidi a-Applied Research* **1976,** *35* (1), K29-K34.
100. Klemens, P. G., *Int. J. Thermophys.* **1996,** *17* (4), 979-981.
101. Kennedy, C. A.; White, M. A.; Wilkinson, A. P.; Varga, T., *Appl. Phys. Lett.* **2007,** *90* (15).
102. Cargnoni, F.; Nishibori, E.; Rabiller, P.; Bertini, L.; Snyder, G. J.; Christensen, M.; Gatti, C.; Iversen, B. B., *Chem.--Eur. J.* **2004,** *10* (16), 3861-3870.
103. Mozharivskyj, Y.; Pecharsky, A. O.; Bud'ko, S.; Miller, G. J., *Chem. Mater.* **2004,** *16* (8), 1580-1589.
104. Liu, H.; Shi, X.; Xu, F.; Zhang, L.; Zhang, W.; Chen, L.; Li, Q.; Uher, C.; Day, T.; Snyder, G. J., *Nat. Mater.* **2012,** *11* (5), 422-425.
105. Wang, P. L.; Kolodiazhnyi, T.; Yao, J.; Mozharivskyj, Y., *J. Am. Chem. Soc.* **2012,** *134* (3), 1426-9.
106. Wang, P.; Forbes, S.; Kolodiazhnyi, T.; Kosuda, K.; Mozharivskyj, Y., *J. Am. Chem. Soc.* **2010,** *132* (25), 8795-8803.
107. Mott, N. F.; Davis, E. A., *Electronic Processes in Noncrystalline Materials (The Internation Series of Monographs on Physics)*. Oxford Univ. Press: 1971; p 451 pp.
108. Kittel, C., *Introduction to solid state physics*. 8th ed.; Wiley: Hoboken, NJ, 2005.

109. Streetman, B. G. B., Sanjay K., *Solid State Electronic Devices*. 6 ed.; Pearson Education, Inc.: Upper Saddle River, New Jersey, USA, 2006.
110. Capasso, F., *Science* **1987,** *235* (4785), 172-176.
111. Mott, N. F., *Can. J. Phys.* **1956,** *34* (12A), 1356-1368.
112. Nuss, J.; Jansen, M., *Z. Anorg. Allg. Chem.* **2012,** *638* (3-4), 611-613.
113. Muir, S.; Vielma, J.; Schneider, G.; Sleight, A. W.; Subramanian, M. A., *J. Solid State Chem.* **2011,** *185* (0), 156-159.
114. Slater, J. C., *The Journal of Chemical Physics* **1964,** *41* (10), 3199-3204.
115. Yoshihara, K.; Taylor, J. B.; Calvert, L. D.; Despault, J. G., *J. Less-Common Met* **1975,** *41* (2), 329-337.
116. Llanos, J.; Conejeros, S.; Cortes, R.; Sanchez, V.; Barahona, P.; Pena, O., *Mater. Res. Bull.* **2008,** *43* (2), 312-319.
117. Weber, F. A.; Schleid, T., *Z. Anorg. Allg. Chem.* **1999,** *625* (11), 1833-1838.